

School of Physical Sciences

Department of Applied Physics

**SYNTHESIS AND CHARACTER OF
A FUNCTIONALLY-GRADED
ALUMINIUM TITANATE/ZIRCONIA-ALUMINA
COMPOSITE**

Suminar PRATAPA

**This thesis is presented as part of the requirements for the
award of the Degree of**

Master of Science

Curtin University of Technology

April 1997

DECLARATION

I hereby declare that this submission is my own work, and that the best of my knowledge contains no material previously published or written by another person, or material which to a substantial extent has not been accepted for the award of any other degree of a university or other institute of higher learning, except where due acknowledgement is made in the text.

Suminar Pratapa

ACKNOWLEDGEMENTS

I would like to thank the various people who have contributed to the completion of this thesis. Firstly, my principal supervisor, Dr. Jim Low, who has given me a ceaseless supervision during my work (even via e-mail), encouraged me to be confident and helped with aspects of data measurement during his study leave in Japan and the USA. Secondly, my associate supervisor, Prof Brian O'Connor, who has supervised me with very deep understanding, patience and encouragement.

I would sincerely express my gratitude to the Australian Agency for International Development (AusAID) which has been my sponsor during my study.

I also wish to acknowledge the following colleagues in the School of Physical Sciences who have given me considerable assistance:

1. Elaine Miller, for assistance in scanning electron microscopy and also for proof reading my thesis,
2. Prof Deyu Li, for assistance in x-ray diffractometry and x-ray fluorescence spectrometry and for useful discussions on Rietveld analysis,
3. Arie van Riessen, for advice on Rietveld methods and electron microscopy,
4. Rob Skala, for discussions on many matters and cooperation in conducting neutron diffraction measurements at ANSTO on my samples.
5. James Browne and Terry MarGrain for their technical assistance.

I also would like to give thanks to people at the Materials Research Group who have given me a sweet friendship during my hard work in this Department.

I would like to thank Grant Ferguson of SCM Chemicals (WA) for supplying the titanium chloride solution and discussion on the chemistry matters regarding the material synthesis. My gratitude is also for the Australian Institute of Nuclear Science and Engineering for research funding awarded to Dr Low (Grant No. 96/142(NS)) for the neutron diffraction experiments. Appreciation should also be given to people at Niihara Laboratory of Osaka University, Japan and National Institute of Standards and Technology, USA, who provided facilities for conducting some of the experiments.

My special thanks are for my wife, Evyta, and my daughter, Zafira, for their everlasting love, understanding, and support.

This thesis is dedicated to my family and parents who have given me endless support and love for the success of my study.

ABSTRACT

A functionally-graded $\text{Al}_2\text{TiO}_5/\text{ZrO}_2\text{-Al}_2\text{O}_3$ (AT/zirconia-alumina) composite has been successfully synthesized by an infiltration process involving an $\alpha\text{-Al}_2\text{O}_3\text{-ZrO}_2$ (90:10 by weight) green body and a solution containing titanium chloride. The mass gain after infiltration has been used to estimate the amount of new phase introduced into the system. The phase composition character of the functionally-graded material (FGM) has been determined by x-ray diffraction. The Rietveld “whole pattern” refinement method was applied to diffraction patterns of the sample which were collected from the surface and at several depths which were made by polishing away the material. Absolute weight fraction determination using the Rietveld external standard method showed that the concentration of AT reduces linearly from the surface to the core. In contrast, the α -alumina content increases with depth in a complementary manner. Low level amorphous phase was also observed. Other functionally-graded microstructural profiles examined were x-ray characteristic line intensity of Ti, Ti dot-mapping, and α -alumina grain size.

The FGM also exhibits graded character in both thermal and mechanical properties, i.e. thermal expansion, microhardness, and Young’s modulus. The thermal expansion coefficient (TEC) of the FGM increased with polishing-depth and approached that of the zirconia-alumina reference sample at a depth of 0.5 mm. Relatively lower thermal expansion and softer surface layer in comparison to those of the core (TEC value of $5.9 \times 10^{-6} \text{ }^\circ\text{C}^{-1}$ and microhardness of 6 GPa compared to $7.4 \times 10^{-6} \text{ }^\circ\text{C}^{-1}$ and 12 GPa, respectively) render possibilities to implement the material to which thermal shock resistance surface but hard core, such as a metal melting crucible, are required.

Load-dependent microhardness was obviously observed on the surface of the material but only slight dependence was observed in the core. This observation indicated that the material exhibit “quasi-ductile” surface but brittle core. In comparison to the reference specimen, the FGM displayed damage-tolerance and remarkable machinability.

TABLE OF CONTENTS

Declaration	i
Acknowledgments	ii
Abstract	iv
Table of Contents	v
List of Figures	ix
List of Tables	xiv
List of Abbreviations	xvi
1. INTRODUCTION	1
1.1 RESEARCH BACKGROUND	1
1.1.1 Functionally-graded Materials (FGMs)	1
1.1.2 Aluminium Titanate	3
1.2 RESEARCH OBJECTIVES	3
1.3 RESEARCH PLAN	5
1.4 STRUCTURE OF THESIS	5
2. LITERATURE REVIEW	6
2.1 INTRODUCTION	6
2.2 FUNCTIONALLY-GRADED MATERIALS (FGMs)	6
2.2.1 Introduction	6
2.2.2 Methods for Producing FGMs	8
2.2.3 Infiltration Methods to Produce FGMs	8
2.2.4 Modelling of Compositional Distribution Profile in FGMs	16
2.2.5 Prediction of Properties in FGMs	23
2.3 ALUMINUM TITANATE	23
2.3.1 Crystal Structure	23
2.3.2 Formation and Properties	25

2.4 ALUMINA-ZIRCONIA SYSTEM	28
2.4.1 Crystal Structures	29
2.4.2 Properties of Alumina-Zirconia Composite	29
2.5 QUANTITATIVE PHASE ANALYSIS USING X-RAY DIFFRACTION	33
2.5.1 Introduction	33
2.5.2 Rietveld Refinement	33
2.5.3 Quantitative Phase Analysis using Rietveld Method	37
3. EXPERIMENTAL METHODS	39
3.1 EXPERIMENTAL DESIGN	39
3.1.1 Processing	39
3.1.2 Characterisation	40
3.1.3 Properties and Microstructure	40
3.2 MATERIAL PROCESSING	41
3.2.1 Powder Processing	41
3.2.2 Ceramic Processing	42
3.3 CHARACTERISATION	43
3.3.1 Differential Thermal Analysis (DTA)	43
3.3.2 Phase Analysis	43
<u>X-Ray Powder Diffraction Pattern Collection</u>	43
<u>Rietveld Refinement</u>	44
<u>Quantitative Phase Analysis using Rietveld Method</u>	46
<u>Mass Attenuation Coefficient Measurement</u>	47
<u>Electron-probe Microanalysis</u>	49
<u>Neutron Powder Diffraction</u>	50
3.4 THERMAL PROPERTIES	50
3.4.1 Thermal Expansion Behaviour	50
3.4.2 Decomposition Study of Aluminium Titanate	50

3.5 MECHANICAL PROPERTIES	51
3.5.1 Microhardness and Fracture Toughness	51
3.5.2 Young's Modulus	52
3.5.3 Contact Hertzian Response	53
3.6 MICROSTRUCTURE	53
 4. SYNTHESIS AND MICROSTRUCTURAL CHARACTERISATION OF A FUNCTIONALLY-GRADED ALUMINIUM TITANATE/ ZIRCONIA-ALUMINA COMPOSITE	 55
4.1 INTRODUCTION	55
4.2 RESULTS	56
4.2.1 Physical Character	56
4.2.2 Graded Compositional Character	63
<u>X-ray Diffraction</u>	63
<u>Attenuation Corrections</u>	67
<u>Phase Composition</u>	71
<u>Energy-dispersive X-ray Microanalysis</u>	73
4.2.3 Microstructure	73
4.3 DISCUSSION	81
4.4. CONCLUSIONS	87
 5. THERMAL AND MECHANICAL PROPERTIES OF A FUNCTIONALLY-GRADED ALUMINIUM TITANATE/ ZIRCONIA-ALUMINA COMPOSITE	 89
5.1 INTRODUCTION	89
5.2 RESULTS	89
5.2.1 Thermal Expansion	89
5.2.2 Thermal Decomposition of AT	93

5.2.3 Microhardness	95
5.2.4 Fracture Toughness	100
5.2.5 Young's Modulus	105
5.2.6 Hertzian Contact Damage	105
5.2.7 Machinability	107
5.3 DISCUSSION	111
5.4 CONCLUSIONS	115
6. CONCLUSIONS AND FURTHER WORK	117
6.1 CONCLUSIONS	117
6.2 FURTHER WORK	118
REFERENCES	120
APPENDIX 1: CRYSTALLOGRAPHIC DATA	130
APPENDIX 2: RIETVELD REFINEMENT OUTPUT	135
APPENDIX 3: CALIBRATION CURVES TO DETERMINE MASS ATTENUATION COEFFICIENT BY COMPTON SCATTERING	142
LIST OF PUBLICATIONS FROM THESIS STUDY	144

LIST OF FIGURES

Figure	Title	Page
<hr/>		
1.1	Graded composition profiles of functionally-graded mullite/alumina produced by infiltration (After Marple and Green 1992). The legend indicates the infiltration time.	4
2.1	Graded characteristic of functionally-graded materials. Gradual change on component concentration causes gradual change in property.	7
2.2	Liquid infiltration steps to produce functionally-graded materials (FGMs).	10
2.3	Indentation fracture toughness of FGMs (measured at surface) (a) mullite/alumina (After Marple and Green 1991). Indentation loads of 2, 5, 8, and 10 kg were applied. (b) mullite/ZTA (After Low <i>et al.</i> 1993). Indentation load of 10 kg was used. The figure shows the curves for mullite/ZTA (—) and mullite/alumina (---) FGMs.	14
2.4	Vickers microhardness of functionally-graded aluminium titanate/alumina along cross-sectional depth (After Low <i>et al.</i> 1995a)	16
2.5	Residual stresses profile of functionally-graded mullite-alumina measured using neutron diffraction technique (After Root <i>et al.</i> 1991). Circles show the stress component perpendicular to the cylinder axis, whereas crosses show the stress component parallel to the cylinder axis.	17
2.6	Variation of effective property P (as an example here, P is effective thermal conductivity λ with $\lambda_A/\lambda_B = 10$) with volume fraction f_A of phase A, see equations 2.2 - 2.4. (—) arithmetic mean; (---) harmonic mean; (—) Markworth model.	19
2.7	Plots of volume fraction (f) versus depth (x) of FGM modelled by Wakashima <i>et al.</i> (1990) with Equation 2.5 for selected N values. Here, values $x_1 = 1$ and $x_2 = 2$ were assumed.	21
2.8	Plots of volume fraction (f) versus relative depth (x/l) of FGM modelled by Markworth and Saunders (1995b) for maximum and minimum values of a_2 in Equation 2.6. Symbol x is sample depth and l is the sample thickness. (—) for minimum a_2 and (---) for maximum a_2 .	21

2.9	Plots of volume fraction (c) versus depth (z) of FGM modelled by Hirano (1995) using Equation 2.7.	22
2.10	Plots of volume fraction (c) versus relative depth (x/d) of FGM modelled by Hirai (1996) using Equation 2.8. d is the sample thickness.	22
2.11	Crystal structure of aluminium titanate (Al_2TiO_5) showing the oxygen octahedra distributed about the metal sites. Symbols M_1 and M_2 designate the two metal ion sites, i.e. the Al^{3+} ion and Ti^{4+} ions. Note that the octahedra are edge-shared as indicated by double lines. Dashed lines are used for octahedra about metal sites located at $z = \frac{1}{2}$, filled atoms lie at $z = \frac{1}{2}$ (After Morosin and Lynch 1972).	24
2.12	Crystal structure of alumina. Figure shows the packing of Al and O ions in the basal plane (After Dörre and Hübner 1984).	30
2.13	Crystal structure of zirconia polymorphs, (a) monoclinic, (b) tetragonal, (c) cubic and (d) orthorhombic (see Table 2.2 for references).	31
3.1	X-ray beam related to the geometry of a sample (After Klug and Alexander 1974, p 371).	45
3.2	Vickers microhardness indentation. Measurement of the impression's diagonals, d , and crack-lengths, c , allow the determination of hardness and fracture toughness.	52
3.3	Contact Hertzian test of a material. A load P is delivered by a tungsten carbide sphere (radius r) over contact radius of a . Two polished halves of the specimen are bonded together, and the load P is applied on the interface (After Cai <i>et al</i> 1994).	54
4.1	SEM back-scattered micrograph of alumina-zirconia preform before infiltration. Note that the porosity (fine black dots) is well-distributed in the material.	57
4.2	Differential thermal analysis result for the TiCl_4 -infiltrated alumina-zirconia mixture. (a) between room temperature and 1500°C , (b) between 1000 and 1500°C .	58
4.3	Photograph of as-fired infiltrated (A, B, and C) and uninfiltrated (D) specimens. Sample A was not turned over during both infiltration and drying. Sample B was turned over during infiltration but not during drying. Sample C was turned over	

during both infiltration and drying. Sample C is black-in-colour due to carbon coating.	62
4.4 X-ray diffraction patterns of AT/zirconia-alumina FGM at various depths. CuK α radiation was used. Legend: ■ = aluminium titanate, ● = alumina, + = monoclinic zirconia and * = tetragonal zirconia.	64
4.5 X-ray diffraction patterns of zirconia-alumina control sample and high-purity alumina external standard. CuK α radiation was used. Legend: ● = alumina, + = monoclinic zirconia, and * = tetragonal zirconia. C = peaks due to contamination of the diffractometer tube.	65
4.6 Rietveld refinement plot of the specimen at a depth of (a) 0.1 mm and (b) 1.2 mm. The observed data are represented by a (+) sign, and the calculated data by a solid line. Vertical lines represent the positions of diffraction lines of alumina, AT, monoclinic zirconia, and tetragonal zirconia, respectively. The line below the plot is the difference profile.	69
4.7 Volume fraction of phases in the AT/zirconia-alumina FGM. (a) Gradual change in volume fraction with depth of AT and α -alumina. (b) Moderate change in volume fraction with depth of zirconia phases. Error bars indicate 2 \times estimated standard deviations.	72
4.8 X-ray characteristic emissions of TiK α , AlK α , and ZrL α with depth of FGM sample measured using energy-dispersive x-ray microanalysis. Error bars indicate 2 \times estimated standard deviations.	74
4.9 (a) Ti dot map at region of approximately 0 - 500 μ m within the AT/zirconia-alumina FGM. (b) Back-scattered SEM micrograph of the associated region. Note the same size of the indicator bars.	75
4.10 Back-scattered SEM micrographs of the as-fired infiltrated specimen at a depth of (a) 0.02 mm (near the surface) and (b) 0.3 mm. Dark grains are alumina, grey ones are aluminium titanate, and light ones are zirconia. Sample was polished and then thermally-etched at 1550° C for 10 mins. Note the increase in grain size of Al ₂ O ₃ with depth.	76
4.10 (Cont'd) Back-scattered SEM micrographs of the as-fired infiltrated specimen at depths of (c) 0.6 mm and (d) 1.0 mm. Note the increase in grain size of Al ₂ O ₃ with depth.	77

4.11	Microcracking phenomena in AT and zirconia grains of AT/zirconia-alumina FGM.	80
5.1	Thermal expansion behaviour of AT/zirconia-alumina FGM and alumina-zirconia control sample between 20° and 1300° C. (a) the FGM, as-fired and after polishing up to 0.3 and 0.5 mm depths, (b) the as-fired FGM and zirconia-alumina control samples.	91
5.2	Neutron diffraction patterns of the AT/zirconia-alumina FGM collected at room and high temperatures ($\lambda = 1.664 \text{ \AA}$). Patterns are highlighted at 2θ -range of: (a) 27-37° and (b) 49-59°. Symbol: AT = aluminium titanate, A = α -alumina, Z-m = monoclinic zirconia, and Z-t = tetragonal zirconia.	92
5.3	X-ray diffraction patterns (CuK α radiation) from the surface of the FGM for decomposition study after annealing at 1050°C for 0, 2, 4, and 6 hours. Note in particular the peak increase in rutile (110). Legend: A = α -alumina, AT = aluminium titanate, Z-m = monoclinic zirconia	94
5.4	Decomposition rate of AT in the AT/zirconia-alumina FGM. Represented ratios are for integrated intensities of [AT(023)/alumina(024)] and [rutile (110)/alumina(024)] lines. Alumina and rutile are denoted as A and T, respectively. Decomposition rate of AT in AT/alumina system [denoted as C, Hwang <i>et al.</i> (1994)] is also presented for comparison.	96
5.5	Variation of Vicker's microhardness with depth of AT/zirconia-alumina FGM for several indentation loads. Upper and lower bound curves were developed from Voigt-type and Reuss-type "rules-of-mixtures", respectively [Equations (2.2) and (2.3)]. Error bars indicate 2 \times estimated standard deviations.	98
5.6	Microhardness as a function of indentation load in the near-surface region and at the core of the AT/zirconia-alumina FGM. Plot for the control specimen is also presented. Error bars indicate 2 \times estimated standard deviations.	99
5.7	Back-scattered SEM micrographs of microhardness indentation of near the surface (0.3 mm) of AT/zirconia-alumina FGM at (a) 25 N and (b) 75 N loads. Associated Vickers hardness (on average) are (a) 8.2 GPa and (b) 5.9 GPa.	101
5.8	Back-scattered SEM micrographs of microhardness indentation of (near) the core (1.2 mm) of AT/zirconia-alumina FGM at (a) 25 N and (b) 75 N loads. Associated Vickers hardness (on average) are (a) 10.3 GPa and (b) 9.1 GPa.	102

5.9	A back-scattered SEM micrograph of a microhardness indentation of zirconia-alumina control sample at 15 N load. Associated Vickers hardness (on average) is 15.4 GPa. Note the presence of cracks at all of the indentation tips.	103
5.10	Back-scattered SEM micrographs of microhardness indentation of AT/zirconia-alumina FGM showing (a) no-crack indentation tip and (b) grain pullout; P = pulled-out grains and G = a grain prior to pullout.	104
5.11	Back-scattered SEM micrographs of microhardness indentations of AT/zirconia-alumina FGM showing (a) crack deflection and (b) grain-bridging (labelled as "G"). Cracks propagate from the left-hand side to right-hand side. Arrows indicate the indentation cracks.	106
5.12	Nomarski optical micrographs of surface (a) and subsurface (b) of the near-surface region of AT/zirconia-alumina FGM at load of P = 2000 N. Note the grain pullout at the contact region indicating the damage-tolerance of the material.	108
5.13	Nomarski optical micrographs of surface (a) and subsurface (b) of the zirconia-alumina ceramic at load of P = 2000 N. Note the cone cracks at the contact region indicating the brittleness of the material.	109
5.14	Indentation stress-strain curves for AT/zirconia-alumina FGM and zirconia-alumina control sample. Solid curves are empirical fits.	110
5.15	Response of materials to a Vicker's hardness indentation. (a) "sink in marks"; typical for ceramics, (b) "rising of material"; typical for metals.	114
A3.1	Calibration curve for mass attenuation coefficient (MAC) determination constructed using alumina-zirconia compacted powders (zirconia content from 0% to 20% by weight). MoK α radiation was used.	142
A3.2	Calibration curve to convert the MAC values from those at the MoK α radiation to those at the CuK α radiation.	143

LIST OF TABLES

Table	Title	Page
1.1	Fabrication methods and examples of FGMs (After Hirai 1996).	9
2.1	Linear thermal expansion coefficient of aluminium titanate.	25
2.2	Crystallographic parameters of zirconia polymorphs.	29
3.1	The refinable parameters for phase analysis.	45
3.2	Compton scatter measurement conditions.	48
4.1	Mass change, density, porosity, and shrinkage of the infiltrated and uninfiltrated (control) specimens.	59
4.2	Scale factors from Rietveld refinement of phases in the functionally-graded aluminium titanate/zirconia-alumina composite at various depths, the alumina- zirconia ceramic control sample, and the α -alumina external standard.	67
4.3	Calculated unit volume cells of phases in the functionally-graded aluminium titanate/zirconia-alumina composite at various depths, the alumina-zirconia ceramic control sample, and the α -alumina external standard from refined lattice parameters (Appendix 2).	68
4.4	Compton scatter intensities and calculated MAC values for CuK α radiation of the functionally-graded aluminium titanate/zirconia-alumina composite at various depths and the alumina-zirconia ceramic control sample.	70
4.5	Absolute weight fraction of phases in the functionally-graded aluminium titanate/zirconia-alumina composite at various depths and the alumina-zirconia ceramic control sample.	70
4.6	Grain size measurement results for the AT/zirconia-alumina FGM.	79
5.1	Thermal expansion coefficient value of the AT/zirconia-alumina FGM and alumina-zirconia control sample between 20° and 1300° C.	93

5.2	Young's modulus of the AT/zirconia-alumina FGM (as-fired and as-polished) and the control sample.	105
A2.1	Rietveld refinement output of x-ray diffraction patterns of AT/zirconia-alumina FGM.	136
A2.1	Rietveld refinement output of x-ray diffraction patterns of AT/zirconia-alumina FGM (continued).	137
A2.1	Rietveld refinement output of x-ray diffraction patterns of AT/zirconia-alumina FGM (continued).	138
A2.2	Rietveld refinement output of x-ray diffraction patterns of zirconia-alumina control sample and α -alumina standard.	139
A2.3	Figures-of-merit from Rietveld refinement of aluminium titanate/zirconia-alumina composite at various depths (in %).	140

LIST OF ABBREVIATIONS

α -Al ₂ O ₃	Alpha alumina
Al ₂ TiO ₅	Aluminium Titanate
AT	Aluminium Titanate
BSCCO	Bi-Sr-Ca-Cu-O superconductor
CuK α	Copper K α line
CVD	Chemical Vapour Deposition
CVI	Chemical Vapour Infiltration
DTA	Differential Thermal Analysis
EB-PVD	Electron-Beam Physical Vapour Deposition
EDS	Energy-dispersive Spectrometer
EPD	Electrophoretic Deposition
Fe ₂ O ₃	Iron trioxide
FWHM	Full-width of Half Maximum
FGM	Functionally-graded Material
GoF	Goodness-of-Fit
HIP	Hot Isostatic Pressing
HP	Hot Pressing
m-ZrO ₂	Monoclinic zirconia
MAC	Mass Attenuation Coefficient
MgO	Magnesia, magnesium oxide
Mg-PSZ	Magnesia Partially-stabilised Zirconia
MoK α	Molybdenum K α line
MRPD	Medium-resolution Powder Diffraction
o-ZrO ₂	Orthorhombic zirconia
R _B	Bragg R-factor
R _p	Profile R-factor
R _{wp}	Weighted Profile R-factor
RIR	Reference Intensity Ratio
PHA	Pulse Height Analyser
SEM	Scanning Electron Microscopy
SENB	Single-edge Notched Beam
SiO ₂	Silica, silicon dioxide
SHS	Self-Propagating High-Temperature Synthesis

t-ZrO ₂	Tetragonal zirconia
TiCl ₄	Titanium chloride
TiO ₂	Titanium dioxide
TEM	Transmission Electron Microscopy
TEOS	Tetraethyl Orthosilicate
TEOT	Tetraethyl Orthotitanate
TMA	Thermal Measurement Apparatus
XRD	X-ray Diffraction
YBCO	Y-Ba-Cu-O superconductor
YSZ	Yttria Stabilised Zirconia
Y-TZP	Yttria Tetragonal Zirconia Polycrystal
ZrO ₂	Zirconia, zirconium dioxide
ZrP	Zirconium Phosphate
ZTA	Zirconia-toughened Alumina

CHAPTER 1

INTRODUCTION

1.1 RESEARCH BACKGROUND

Ceramic materials have become increasingly important for structural applications in modern industry as they exhibit exceptional properties such as hardness, corrosion and erosion resistance, and excellent ability to retain strength at elevated temperature (Richerson 1992). The attractive properties of ceramic materials include:

- a. the typical value of hardness is approximately twice that of metals (Callister 1991, p139),
- b. the service temperature is considerably higher compared with that of polymers and metals (Richerson 1992, p162),
- c. the wide range of values of thermal conductivity makes them applicable for both heat storage and heat dissipation (Richerson 1992, pp809-812).

Combining two or more types of ceramics may produce a composite material with unique properties. Demand for such materials has increased over several decades in situations where monolithic material could not meet particular service requirements. Some ways of combining one ceramic with another are particulate-dispersion, fiber-reinforcing, and laminating.

1.1.1 Functionally-graded Materials (FGMs)

Functionally-graded materials (FGMs) are composite materials which exhibit a progressive change in composition, structure, and properties as a function of spatial direction within the material (e.g., Markworth *et al.* 1995a; Hirai 1996). The aim of producing FGMs is, therefore, to obtain a material with two different characteristics in its two opposite faces.

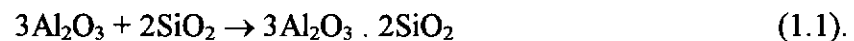
FGMs can be produced in several ways. Hirai (1996) classified the fabrication of FGMs into three approaches, i.e. by gas phase, liquid phase, and solid phase. Most FGMs fabricated involve a metallic component. Some ceramic-ceramic FGMs have been fabricated using chemical-vapour deposition (CVD), electro-deposition, sol-gel, or slip casting methods. Metal-ceramic FGMs can be

produced by CVD, electro-deposition, molten metal infiltration, centrifugal casting, powder infiltration, slip casting, filtration, sedimentation, sintering, and diffusion and reaction techniques.

Graded profiles in FGMs can be constructed by several ways. Micrography (optical or scanning electron microscopy) and microprobe analysis are common methods to reveal such profile (Sarkar *et al.* 1993; Sasaki and Hirai 1991; Marple and Green 1990). Microstructure, such as grain size, can show the material profile changes (Sarkar *et al.* 1993; Sasaki and Hirai 1991). The compositional graded profile of FGMs can be constructed by measuring the characteristic x-ray emission in electron microprobe. Quantitative x-ray diffraction (Klug and Alexander 1974) is another prospective method for characterising the compositional graded profile. This last technique was used in this research.

Infiltration can be used to produce ceramics and their composites (e.g., Glass and Green 1987; Marple and Green 1989-1992; Low *et al.* 1993 and 1996a; Tu and Lange 1995; Pratapa and Low 1996). This technique includes the soaking of porous powder compacts with suitable infiltrants. Subsequent heat treatment is required to produce a dense multiphase body. A more detailed description of this method is given in Chapter 2. Examples of use of the infiltration method for introducing new ceramic phases into ceramic bodies are alumina into Y-TZP (Glass and Green 1987), mullite into alumina (Marple and Green 1989), mullite into ZTA (Low *et al.* 1993), and aluminium titanate (AT) into alumina or ZTA (Low *et al.* 1996a; Pratapa and Low 1996).

The infiltration technique was used by Marple and Green (1989) to incorporate mullite ($3\text{Al}_2\text{O}_3 \cdot 2\text{SiO}_2$) into alumina resulting in functionally-graded mullite/alumina composites. Mullite in these materials was formed via the reaction



The alumina preforms, with approximately 39% porosity, were fully immersed in a hydrolyzed ethyl silicate containing 25 wt% SiO_2 for 1 min, 4 h, and 2 x 4 h. The infiltrated bodies were dried at 100°C and then sintered at 1600°C for 12 h. Only mullite and alumina were detected by x-ray diffraction analysis in the as-fired

specimens. Marple and Green (1989) made use of electron probe microanalysis to determine the concentration of the constituents in the material. The graded profile of the mullite content is evident from the results shown in Figure 1.1.

1.1.2 Aluminium Titanate

Aluminium titanate (AT), Al_2TiO_5 , ceramic has a low thermal expansion coefficient and excellent thermal shock resistance (e.g., Ohya *et al.* 1983; Morishima *et al.* 1986) which makes it a promising component for repeated high temperature applications. Ohya *et al.* (1983) reported that the thermal expansion coefficient of AT was $4 \times 10^{-6} \text{ }^\circ\text{C}^{-1}$. AT is usually prepared by reaction sintering between Al_2O_3 and TiO_2 powders. Formation of AT occurs above 1280°C (Kato *et al.* 1980) in an oxidizing atmosphere according to



However, AT also displays low mechanical strength and poor high temperature stability. Pure AT exhibits very low flexural strength, i.e. 20 MPa (Hwang *et al.* 1994). AT decomposes into its original former alumina and TiO_2 -rutile between $900 - 1200^\circ\text{C}$ (Kato *et al.* 1980). If ZrO_2 is added, AT can be partly stabilised (Wohlfromm *et al.* 1991), while addition of MgO will effectively stabilise the AT structure at 900°C . Fe_2O_3 provides better stabilisation at higher temperature (Battilana *et al.* 1995). Addition of MgO , ZrO_2 , and SiO_2 (by allowing formation of mullite) has been shown to improve the strength of AT (Wohlfromm *et al.* 1991). Despite of its low strength, aluminium titanate-based ceramics exhibit excellent flaw-tolerance (Runyan and Bennison 1991; Padture *et al.* 1993).

1.2 RESEARCH OBJECTIVES

The main objective of this research was to produce a functionally-graded composite which has a low thermal expansion and flaw-tolerant aluminium titanate outer-case and strong and tough zirconia- alumina core by infiltrating zirconia-

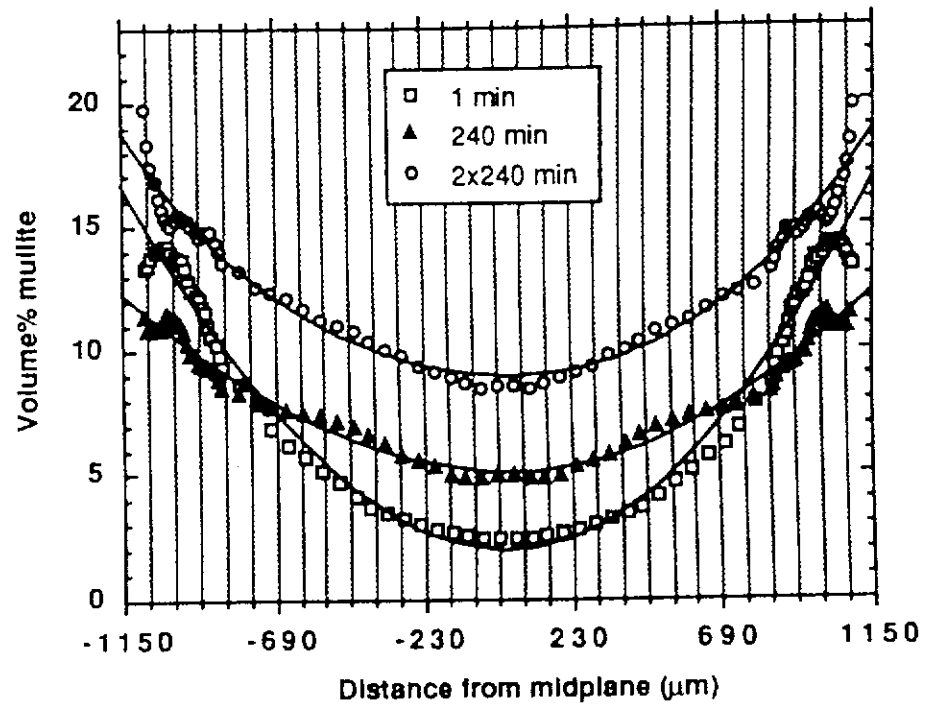


Figure 1.1 Graded composition profiles of functionally-graded mullite/alumina produced by infiltration (After Marple and Green 1992). The legend indicates the infiltration time.

alumina preforms with a TiO_2 precursor solution through a sintering reaction in forming the aluminium titanate. The presence of ZrO_2 in the system is expected to improve the mechanical properties as well as prevent the decomposition of aluminium titanate.

1.3 RESEARCH PLAN

There are several experimental aspects in realising the research objectives which are:

- a) Characterisation of the functionally-graded profile of the FGM.
- b) Measurement of the thermal behaviour of the FGM.
- c) Measurement of the mechanical properties of the FGM.

There are four main areas involved in this research:

1. The synthesis and processing of the composites utilising high-purity alumina and monoclinic zirconia powders and a solution containing TiCl_4 .
2. Characterisation of the graded composition profile on the composite using x-ray diffraction, attenuation coefficient measurement, and electron-probe microanalysis.
3. Evaluation of thermal and mechanical properties including thermal expansion coefficient, effect of thermal treatment on compositions, hardness, indentation fracture toughness, and contact damage response.
4. Examination of microstructures, including grains characterisation and microstructure of indentation hardness and cracks.

1.4 STRUCTURE OF THESIS

This first chapter discusses the background to the research topic and the aims of the research. The literature review of related research topics is elaborated in Chapter 2. In Chapter 3, the detailed experimental procedure is described. Results and discussion of the synthesis and microstructural characterisation of the FGM are detailed in Chapter 4. In Chapter 5, the results from thermal and mechanical properties measurements of the FGM are discussed. Finally, the conclusions and proposed further work are outlined in Chapter 6.

CHAPTER 2

LITERATURE REVIEW

2.1 INTRODUCTION

In this chapter, the theoretical backgrounds related to the research topic are explored. These topics considered functionally-graded materials (FGMs), aluminium titanate, zirconia-alumina ceramic system and quantitative phase analysis using x-ray diffraction and Rietveld analysis. Aluminium titanate is the introduced phase in the FGM and is expected to improve the flaw-tolerance of the matrix. Zirconia-alumina ceramic is the matrix of the FGM and used as a reference specimen in this research. Therefore, reviews on both aluminium titanate and the matrix are presented. A theoretical survey on quantitative phase analysis using XRD and Rietveld analysis is also presented here since this novel method was used to characterise the phase composition of the FGMs.

2.2 FUNCTIONALLY-GRADED MATERIALS (FGMs)

2.2.1 Introduction

As explained in the introduction chapter, FGMs are composite materials which exhibit a progressive change in composition, structure, and properties as a function of spatial direction within the material (Markworth *et al.* 1995a; Hirai 1996). Figure 2.1 shows in schematic form the typical microstructural and property character of a functionally-graded material.

The concept of FGMs was first proposed in 1984 by Japanese material scientists led by Niino (Koizumi 1992). The original purpose of the development of these materials was to produce superheat-resistant materials for propulsion systems and airframes of spaceplanes. The research focussed on ceramic-metal FGM systems. For example, superheat-resistant ceramics were prepared on the high-temperature side of the composite and tough metals with high thermal conductivity were placed on the low-temperature side, to achieve a graded composition of ceramic to metal (Koizumi 1992). The development of FGMs has now been extended to electronic, optical, biomedical, and other applications (Hirai 1996).

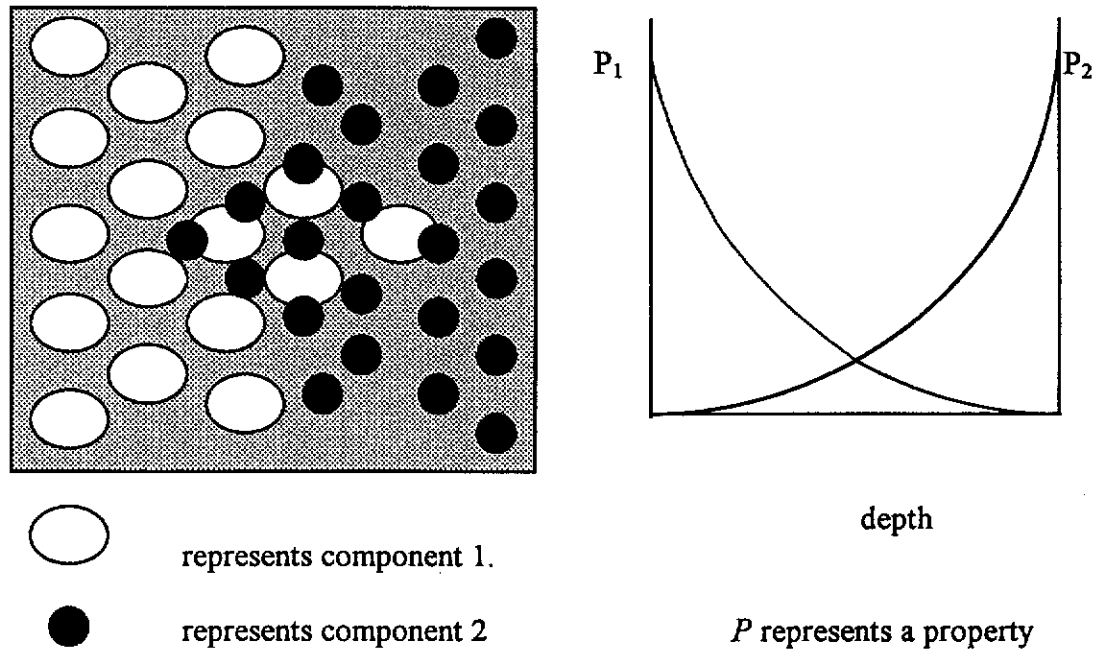


Figure 2.1 Graded characteristic of functionally-graded materials. Gradual change in component concentration causes gradual change in property.

FGMs can be designed in various ways to produce several types of continuous component change (Hirai 1996). Firstly, there are FGMs which exhibit *continuous changes in concentration*. Most FGMs produced are of this type. The second type exhibits *continuous changes in morphology*, for example from spherical particles in one side to fiber-like ones in the other side. The third exhibits a *continuous change in state*. An example of this type of change is a material with a very dense surface on one side and a porous surface on the other side. Another type of change is a *continuous change in crystallinity*. With this type of change a crystalline/amorphous FGM can be produced.

The following sub-sections discuss the various topics related to functionally-graded materials. The discussion begins with the techniques for producing FGMs. The use of infiltration to produce FGMs and the modelling of compositional profiles are reviewed in the next sections.

2.2.2 Methods for Producing FGMs

FGMs can be produced in several ways. Hirai (1996) has classified the fabrication of FGMs into three approaches, i.e. by gas phase, liquid phase, and solid phase. Table 2.1 lists various fabrication methods and examples of FGMs according to this classification. The list shows that most FGMs fabricated involve a metallic component. Some ceramic-ceramic FGMs have been fabricated using CVD, electro-deposition, sol-gel or slip casting methods. Metal-ceramic FGMs can be produced by CVD, electro-deposition, molten metal infiltration, centrifugal casting, powder infiltration, slip casting, filtration, sedimentation, sintering, and diffusion and reaction techniques. Ceramic-polymer FGMs have also been produced by infiltration such as in epoxy-modified Y-Ba-Cu-O (YBCO) and Bi-Sr-Ca-Cu-O (BSCCO) superconductors (Low *et al.* 1994 and 1995) and epoxy-zirconium phosphate (ZrP) protonic conducting materials (Low *et al.* 1996b).

2.2.3 Infiltration Method for Producing FGMs

Ceramic precursors in the liquid infiltration method can be employed to produce FGMs. Figure 2.2 shows the steps required to produce FGMs by infiltration. This infiltration method can be used to produce ceramics and their composites (e.g., Glass and Green 1989; Marple and Green 1990; Low *et al.* 1993 and 1996a; Tu and Lange 1995; Pratapa and Low 1996). The technique involves the immersion of porous powder compacts in suitable infiltrants. Subsequent heat treatment produces a dense multiphase body. Heat treatment may generate other processes such as solid-state reaction and decomposition. Additional phases can be introduced into the body when the infiltrant reacts with the host matrix. Since infiltration may introduce a graded amount of infiltrant according to depth, this technique can be used to produce ceramic-ceramic FGMs. This method offers many possibilities of producing varied kinds of FGMs for broad applications and allows surface modifications either on the whole surface by full-infiltration or only on one surface by partial infiltration. The full infiltration method was employed in this research.

Table 2.1 Fabrication methods and examples of FGMs (After Hirai 1996).

Method	Examples
1. Gas phase method	
CVD	SiC/C, TiC/C, SiC/TiC, SiO ₂ /SiO ₂ (GeO ₂), Cr ₃ C/Cr
CVI	SiC/C, TiB ₂ /SiC
EB-PVD	PSZ
Ion plating	TiN/Ti, TiC/Ti
Chemical gas reaction	SiC/C
2. Liquid Phase Method	
Electro deposition	Cu/CuZn, Cu/CuNi, ZrO ₂ /Al ₂ O ₃
Electroplating	Cu/CuZn, Cu/CuNi
Sol-gel	SiO ₂ /TiO ₂ , SiO ₂ /GeO ₂
Plasma spraying	PSZ/NiCrAlY, PSZ/NiCrAl
Molten Metal Infiltration	SiC/C, W/Cu, Al ₂ O ₃ /Al
Centrifugal Casting	SiC/Al
3. Solid Phase Method	
Centrifugal	ZrO ₂ /NiCr
Spraying	PSZ/SS
Powder Infiltration	Al ₂ O ₃ /Ni
Slip casting	Al ₂ O ₃ /Al ₂ TiO ₅ , Al ₂ O ₃ /mullite, ZrO ₂ /Ni, Al ₂ O ₃ /ZrO ₂
Sedimentation	Al ₂ O ₃ /NiAl, Al ₂ O ₃ /W
Filtration	Al ₂ O ₃ /Ni
Painting	SiC (fiber)/SiC
Sintering, HP, HIP	Al ₂ O ₃ /Ni, MgO/Ni, AlN/Ni, AlN/Al
Plasma activated	PSZ/TiAl, PSZ/Ti, YSZ/SS
SHS	TiC/NiAl, TiB ₂ /Cu, TiB ₂ /Ni, AlN/Al
Diffusion and reaction	ZrO ₂ / Al ₂ O ₃ , ZrSi ₂ /Zr

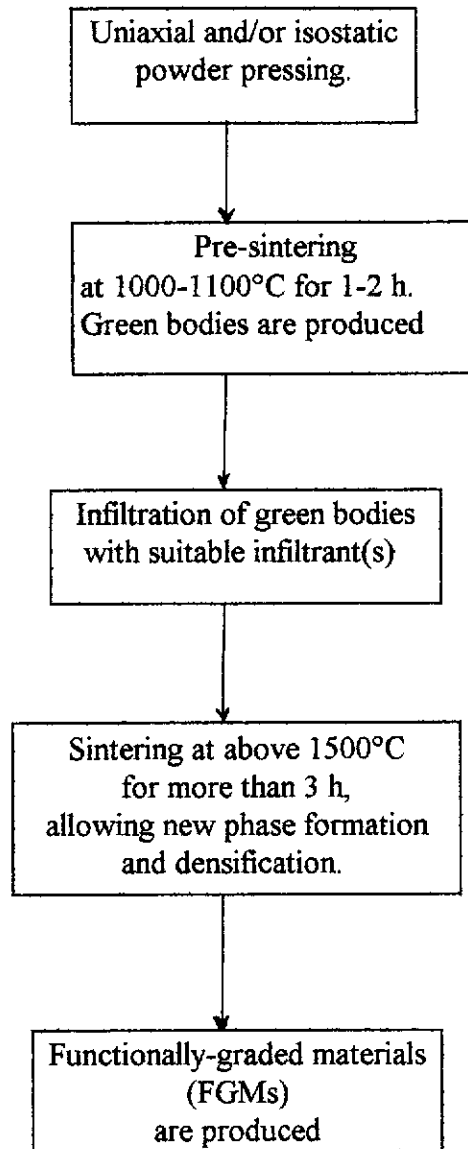


Figure 2.2 Liquid infiltration steps to produce functionally-graded materials (FGMs)

The infiltration method has been successfully employed to introduce new ceramic phases into ceramic bodies e.g. alumina into Y-TZP (Glass and Green 1987), mullite into alumina (Marple and Green 1989 - 1993), mullite into ZTA (Low *et al.* 1993), and aluminium titanate (Al_2TiO_5) into alumina or ZTA (Low *et al.* 1996a; Pratapa and Low 1996). However, most of the research did not discuss graded profile characterisation.

Marple and Green (1989) used the infiltration method to incorporate mullite ($3\text{Al}_2\text{O}_3 \cdot 2\text{SiO}_2$) into alumina. Alumina preforms, with approximately 39% porosity, were fully immersed in a prehydrolyzed ethyl silicate (TEOS) containing 25 wt% SiO_2 for 1 min, 4 h, and 2 x 4 h. The infiltrated bodies were dried at 100°C and then sintered at 1600°C for 12 h. The formation of mullite in these materials followed the reaction described in Equation (1.1).

Marple and Green (1992) made use of the electron probe microanalysis to determine the concentration of the constituents in the material. The results are shown in Figure 1.1.

Further investigation (Marple and Green 1990) showed that the process of incorporating mullite into alumina using infiltration techniques involved several aspects. Firstly, the infiltration depth, d , of the infiltrant within the porous alumina depends on the square root of infiltration time, t , as observed by Glass and Green (1987)

$$d \propto t^{1/2} \quad (2.1).$$

The SiO_2 elemental concentration (and hence mullite) decreased from the surface toward the interior (Figure 1.1). It was suggested that the cause of the gradient was a redistribution of the liquid during the drying stage. Secondly, the amount of incorporated phase was influenced by the degree of porosity within the preforms, the density of the infiltrant, and reactions during sintering. Increasing the mullite content was important not only to enhance the properties but also to reduce the amount of shrinkage during final heat-treatment. Thirdly, multiple infiltrations

can be used to increase the mullite content (Figure 1.1). An increase of mullite content with infiltration time was observed.

Glass and Green (1987) applied the infiltration method to introduce an $\text{Al}_2\text{O}_3/\text{ZrO}_2$ composite surface onto a yttria-tetragonal zirconia polycrystal (Y-TZP) matrix. The Y-TZP green body had 55% theoretical porosity after isostatic pressing at 138 MPa. A solution of $\text{Al}(\text{NO}_3)_3 \cdot 9\text{H}_2\text{O}$ was used since it readily infiltrated to the green compact and decomposed at a much lower temperature than that of sintering (1500°C for 2 h). The densities of the fired specimens were measured and used to estimate the volume fractions of introduced Al_2O_3 . The graded profile was not determined. The plot of relative thickness versus the square root of infiltration time was found to be linear. This shows that infiltration follows capillary process.

Low *et al.* (1993 and 1996a) and Pratapa and Low (1996) made use of the infiltration method to incorporate mullite into ZTA matrix, aluminium titanate into alumina and aluminium titanate and mullite into ZTA matrix. They used tetraethyl orthosilicate (TEOS, a SiO_2 -rich organic solution) and tetraethyl orthotitanate (TEOT, a TiO_2 -rich organic solution), respectively. Sintering at 1550°C for 3 h was applied to the specimens to allow the formation of mullite and aluminium titanate and the densification of the specimens. The formation of aluminium titanate occurred following Equation (1.2). The graded profile of the products was characterised by elemental dot-mapping using electron-probe analysis. Both Si and Ti dot-mapping showed the graded characteristic of the materials. The graded phase abundance profile was not constructed.

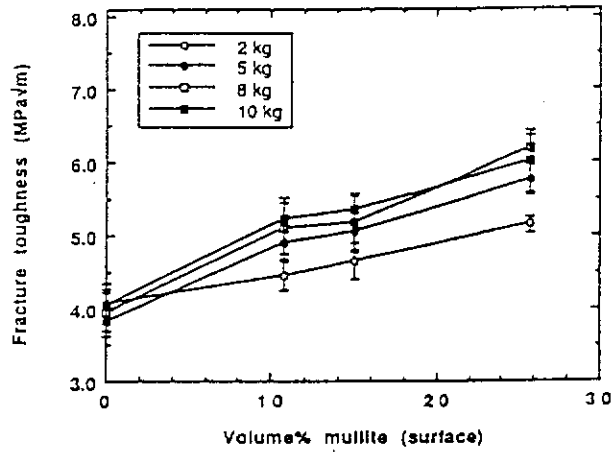
Performance of FGMs produced by infiltration

The mechanical properties of functionally-graded mullite/alumina composites produced using the infiltration process (TEOS as infiltrant) were investigated by Marple and Green (1991). They measured the elastic modulus and biaxial flexural strength of bulk specimens. Vickers indentation fracture toughness measurement was carried out at the “surface” of the materials after polishing the samples up to $90\text{ }\mu\text{m}$. There was no attempt to reveal the properties as a function of depth to show the graded behaviour of the material. They showed that the elastic moduli of

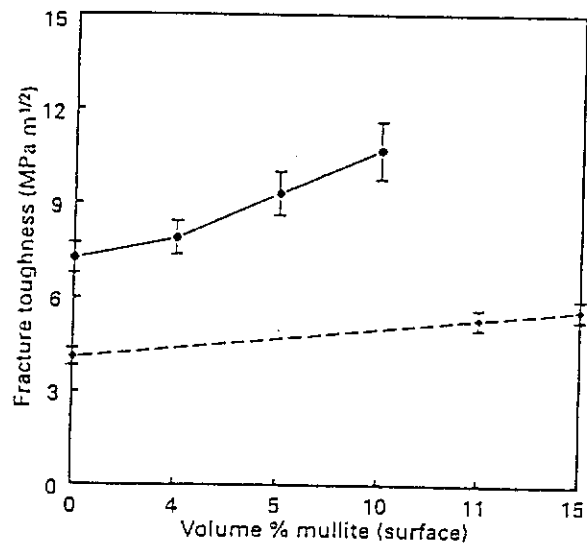
mullite-alumina decreased with increasing mullite content. This result was as expected since mullite has a lower elastic moduli than alumina. Their investigation of the strength of the materials indicated that the introduction of mullite by infiltration led to substantial increases in the strength over pure alumina. Sintered samples which had been infiltrated once for 4 h had an average strength 35% higher than alumina samples. Four-hour infiltration performed twice produced samples with strength 65% higher than pure alumina samples. Marple and Green (1991) also showed that the indentation fracture toughness of the composites tended to increase with an increasing amount of mullite at the surface. The trend in the fracture toughness change with mullite content is depicted in Figure 2.3a. Under all loads used, the fracture toughness increases with increased content of mullite at the surface.

Possibilities proposed to explain the improvement of the strength and the indentation fracture toughness included (i) changes in dominant flaw population during processing, (ii) effect of mullite on crack propagation, e.g. by crack deflection or stress-induced microcracking, and (iii) presence of residual compressive stresses in the surface region due to the concentration gradient of mullite and thermal expansion coefficient mismatch between the surface and the bulk. In a further study (Marple and Green 1992), it was claimed that compressive surface stresses were the major contributor to the improvements of strength and fracture toughness. They calculated the residual stresses in the mullite/alumina systems from residual strains measured using a strain gage, and related the stresses to the change in strength and surface fracture toughness. They found that increases in residual compressive stresses corresponded to the improvement in those mechanical properties.

Low *et al.* (1993 and 1996a) studied the mechanical properties of other types of FGMs, i.e. mullite/ZTA and aluminium titanate/alumina systems. The graded profile was solely made using elemental x-ray dot map. Investigation on the surface indentation fracture toughness showed that mullite-ZTA (TEOS as infiltrant) was tougher than pure ZTA ceramic (Figure 2.3b). They also reported that the surface microhardness of this FGM was further improved when sinter-HIP was applied. The microhardness measurement was performed in aluminium titanate/alumina



(a)



(b)

Figure 2.3 Indentation fracture toughness of FGMs (measured at surface)
 (a) mullite/alumina (After Marple and Green 1991). Indentation loads of 2, 5, 8, and 10 kg were applied.
 (b) mullite/ZTA (After Low *et al.* 1993). Indentation load of 10 kg was used. The figure shows the curves for mullite/ZTA (—) and mullite/alumina (---) FGMs.

system along its cross-sectional depth (Figure 2.4). The microhardness values observed for the aluminium titanate/alumina system were slightly less than those for pure ZTA (i.e. approximately 14 GPa) and reasonably constant with depth.

The presence of residual stresses in the functionally-graded materials is believed to be responsible for improving the mechanical properties of the materials (e.g., Marple and Green 1991; Low *et al.* 1993 and 1996a). The presence of compressive residual stress in a functionally-graded mullite/alumina composite has been verified using the strain gage approach (Marple and Green 1992) and the neutron diffraction technique (Root *et al.* 1991). These stresses were introduced into the surface region due to the graded composition of mullite from the surface to the center and the resulting thermal expansion mismatch between mullite and alumina.

Presintered alumina cylindrical preforms with 33% porosity were infiltrated with a hydrolyzed ethyl silicate (a SiO₂-rich solution) prior to sintering at 1600° and 1650° C (Marple and Green 1992; Root *et al.* 1991). Upon cooling, the unmodified core of the composites shrank more than the modified outer shell. This produced compressive stresses on the surfaces of the infiltrated samples. The graded composition of mullite (and hence alumina, Figure 1.1) through the depth created a graded stress profile throughout the samples.

Measuring this profile using a strain-gage technique, Marple and Green (1992) concluded that residual stress profiling using this method was not sufficiently sensitive to detect stress changes over a small distance. Nevertheless, compressive residual stresses were detected in the near surface region of the materials.

From neutron diffraction measurements on a functionally-graded mullite/alumina, Root *et al.* (1991) reported a compressive component stress value of -130 ± 30 MPa both parallel to the cylinder axis (relative to the value near the top surface) and perpendicular to the cylinder axis (relative to value near the mid-height of the cylinder) - see Figure 2.5. They also observed an overall tensile shift of the macroscopic stress profile in a fully-infiltrated sample. The shift occurred possibly due to a grain interaction effect between the alumina and the mullite.

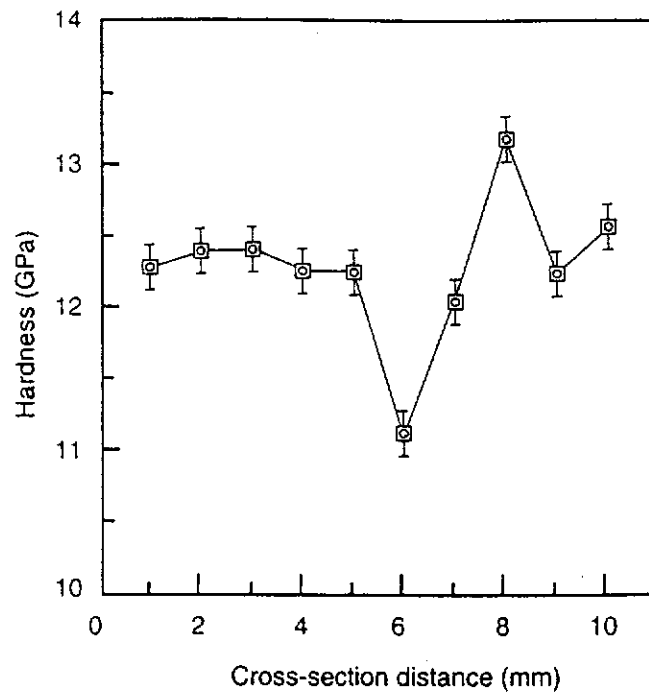
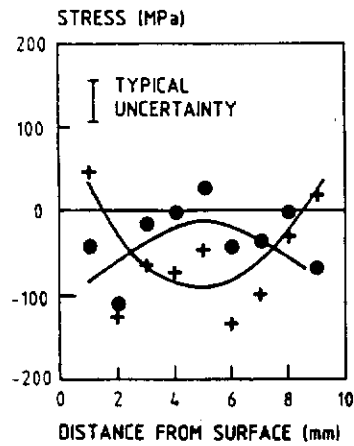


Figure 2.4 Vickers microhardness of functionally-graded aluminium titanate alumina along cross-sectional depth (After Low *et al.* 1996a).

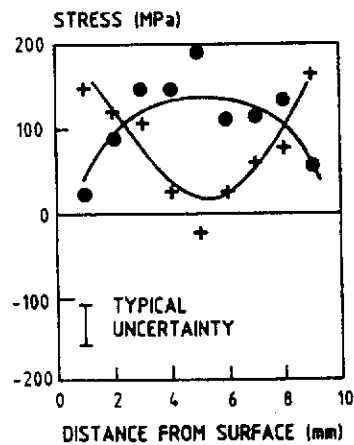
Concavity of the top and bottom surfaces was also observed which can be associated with the compressive stress component parallel to the cylinder axis. The authors explained that the concave surface occurred when the pellet core contracted in the axial direction. As radial shrinkage of the pellet core took place, compressive forces developed in the plane of the concave surface, directed towards the pellet axis. The concavity of both surfaces was caused by the cancellation of all components of the radial forces and the superimposition of the forces along the cylinder axis to give a net force towards the pellet centre.

2.2.4 Modelling of Compositional Distribution Profile in FGMs

Modelling studies on FGMs have been reviewed by Markworth *et al.* (1995a). These models are based on the composition change of an FGM which can vary over a wide range. As a result, microstructure-dependent properties will also vary with depth within the material. Two aspects were reviewed for the modelling procedure (Markworth *et al.* 1995a), i.e. calculation of microstructure-dependent properties and analysis of materials design, fabrication, and performance.



(A) Infiltrated for 1 minute



(B) Infiltrated for 24 h

Figure 2.5 Residual stresses profile of functionally-graded mullite-alumina measured using neutron diffraction technique (After Root *et al.* 1991). Circles show the stress component perpendicular to the cylinder axis, whereas crosses show the stress component parallel to the cylinder axis.

For a mixture or dispersed system, the microstructure-dependent rule of mixture can be used to model properties, e.g. thermal conductivity and Young's modulus, of the material (Callister 1991, p532). The effective value of a property P of a binary system can be estimated using the Voigt-type approach

$$P = f_A P_A + f_B P_B \quad (\text{arithmetic mean}) \quad (2.2)$$

and the Reuss-type approach

$$\frac{1}{P} = \frac{f_A}{P_A} + \frac{f_B}{P_B} \quad (\text{harmonic mean}) \quad (2.3)$$

where P_A and P_B are the values of a particular property for pure A and pure B, respectively, and f_A and f_B are the respective volume fractions of A and B. As these approaches have limited validity, an improvement has been proposed by Markworth *et al.* (1995a) in the form of

$$P = f_A P_A + f_B P_B + f_A f_B Q_{AB} \quad (2.4)$$

where Q_{AB} is a function that depends on P_A , P_B , f_A , f_B , and microstructure-dependent properties such as thermal conductivity (λ), coefficient of thermal expansion, bulk modulus, and shear modulus. A schematic diagram of way in which these functions vary with volume fraction is shown in Figure 2.6.

Equations (2.2) to (2.4) can be used to model the bulk properties of an FGM provided that the spatial variation of composition is known. Several models of composition-property relationship of FGMs have been proposed, for example, Wakashima *et al.* (1990) and Markworth and Saunders (1995b). In these models, the FGM was considered to have two components (or phases) denoted as 1 and 2. Other considerations were that the geometry was one dimensional (consider here as x-direction) and that the material was very dense. The local volume fraction of phase 1, $f_1(x)$, is a continuous function. The model proposed by Wakashima *et al.* (1990) took the form:

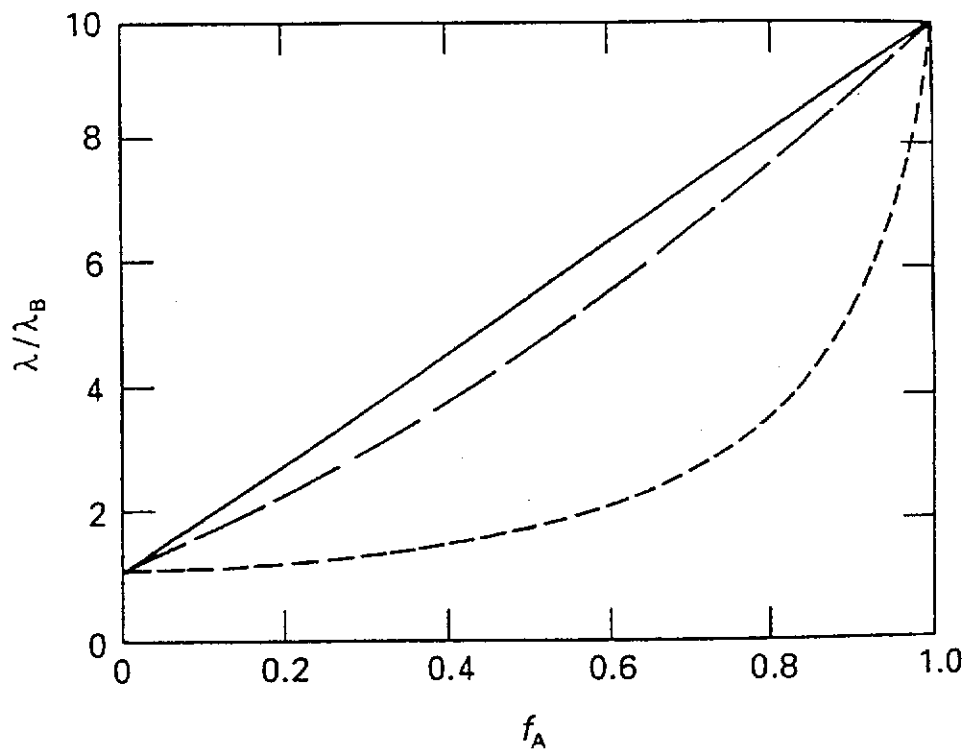


Figure 2.6 Variation of effective property P (as an example here, P is effective thermal conductivity λ with $\lambda_A/\lambda_B = 10$) with volume fraction f_A of phase A, see equations 2.2 - 2.4.
 (—) arithmetic mean; (---) harmonic mean; (— · —) Markworth model.

$$f_1(x) = \left[\frac{x_2 - x}{x_2 - x_1} \right]^N \quad (2.5)$$

where x_1 and x_2 are border regions of pure phase 1 and phase 2, respectively, and N is a variable parameter which determines the curvature of $f_1(x)$. Markworth and Saunders (1995b) proposed a simpler quadratic function model

$$f_1(x) = a_0 + a_1x + a_2x^2 \quad (2.6)$$

where a_0 , a_1 , and a_2 are variable parameters, the values of which are determined by imposed constraints and the optimisation process. The two models for $f_1(x)$ are plotted in Figures 2.7 and 2.8.

Hirano (1995) proposed another form of composition function

$$f(x) = (f_1 - f_0) \left(\frac{x - x_0}{x_1 - x_0} \right)^n \quad (2.7)$$

where f is composition, x is a non-dimensional thickness, and n is a parameter controlled by the compositional distribution profile. Changes in the distribution parameters f , x , and n lead to a various forms of compositional distribution (Figure 2.9). Parameters x_0 and x_1 represent the thickness of non-graded layers and f_0 and f_1 are the corresponding compositions.

Hirai (1996) proposed a simplified function from Equation (2.7) which took the form of

$$f(x) = \left(\frac{x}{d} \right)^n \quad (2.8)$$

where f is the volume fraction, x is the relative distance from the interface or surface, and d is the thickness of the FGM layer. Figure 2.10 shows the relationship described by Equation (2.8).

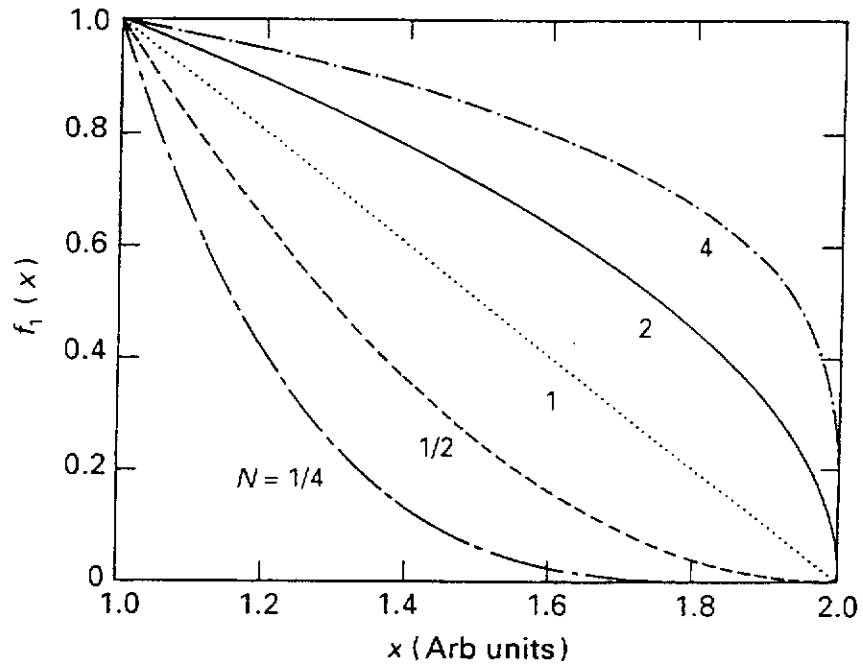


Figure 2.7 Plots of volume fraction (f) versus depth (x) of FGM modelled by Wakashima *et al.* (1990) with Equation 2.5 for selected N values. Here, values $x_1 = 1$ and $x_2 = 2$ were assumed.

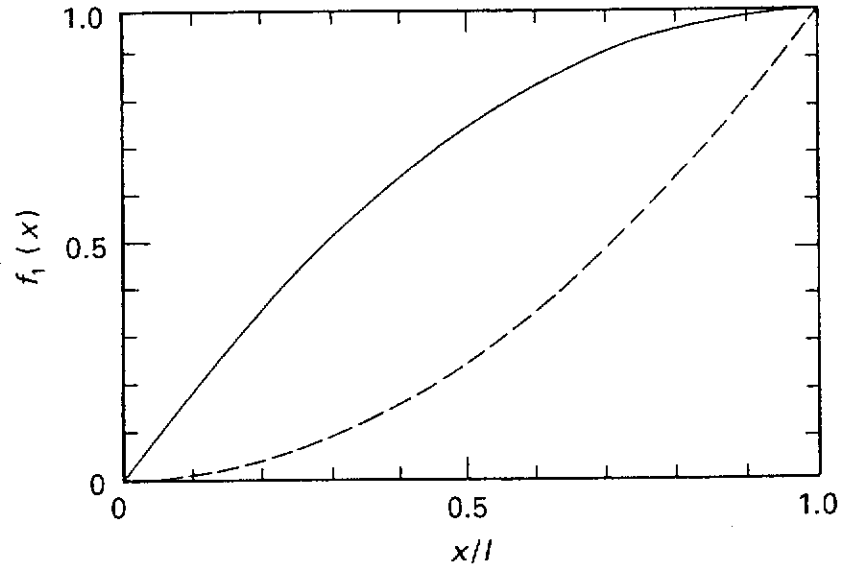


Figure 2.8 Plots of volume fraction (f) versus relative depth (x/l) of FGM modelled by Markworth and Saunders (1995b) for maximum and minimum values of a_2 in Equation 2.6. Symbol x is sample depth and l is the sample thickness.
(—) for minimum a_2 and (---) for maximum a_2 .

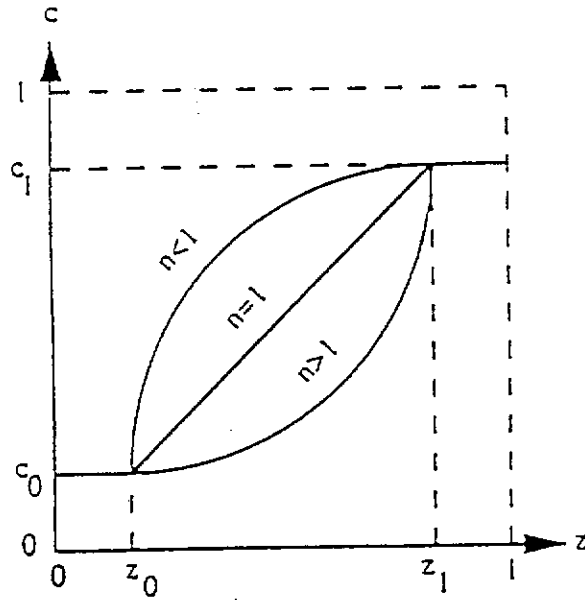


Figure 2.9 Plots of volume fraction (c) versus depth (z) of FGM modelled by Hirano (1995) using Equation 2.7.

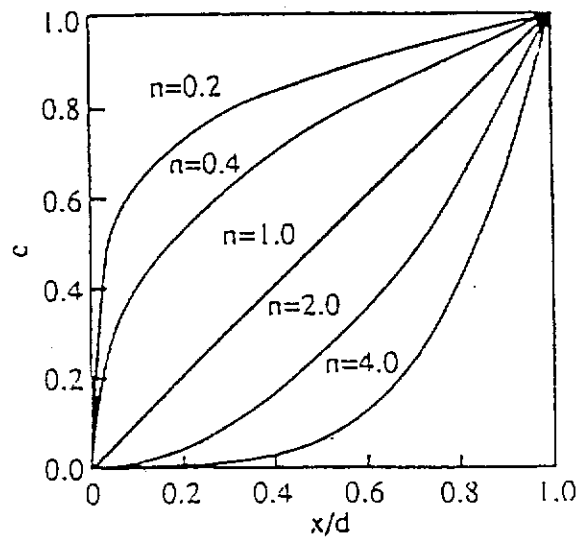


Figure 2.10 Plots of volume fraction (c) versus relative depth (x/d) of FGM modelled by Hirai (1996) using Equation 2.8. d is the sample thickness.

2.2.5 Prediction of Properties in FGMs

With the knowledge of $f_i(x)$ and the composition-dependent microstructure, one can determine the corresponding x -dependence effective values of the properties such as the coefficient of thermal conductivity, $\lambda(x)$, Young's modulus, $E(x)$, and coefficient of thermal expansion, $\alpha(x)$. Furthermore, the knowledge of these values can be used to calculate temperature and stress distributions (Markworth *et al.* 1995a):

(1) temperature distribution (for steady-state conditions)

$$\lambda(x) \frac{dT}{dx}(x) = \text{constant} \quad (2.9)$$

(2) normal stress distribution

$$\sigma(x) = -\kappa \alpha(x) E(x) [T(x) - T_c] \quad (2.10)$$

where $T(x)$ is temperature at position x , T_c is the temperature of the cooler end and κ is a constant. The associated strain field can also be determined from this normal stress distribution function.

2.3 ALUMINIUM TITANATE

The crystal structure, the formation, and the thermal and mechanical properties of aluminium titanate (AT) are described in this section.

2.3.1 Crystal Structure

The crystal structure of AT is of the pseudobrookite type (Figure 2.11). A study by Austin and Schwartz (1953) showed that the crystal structure of AT can be classified under the orthorhombic $Cmcm$ space group with lattice parameters: $a = 3.557 \text{ \AA}$, $b = 9.436 \text{ \AA}$, and $c = 9.648 \text{ \AA}$.

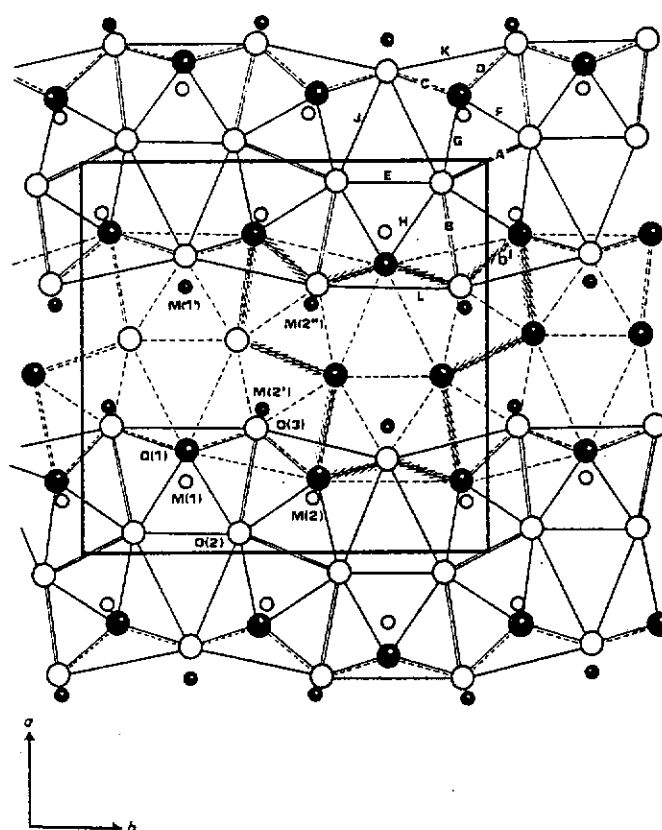


Figure 2.11 Crystal structure of aluminium titanate (Al_2TiO_5) showing the oxygen octahedra distributed about the metal sites. Symbols M_1 and M_2 designate the two metal ion sites, i.e. the Al^{3+} ion and Ti^{4+} ions. Note that the octahedra are edge-shared as indicated by double lines. Dashed lines are used for octahedra about metal sites located at $z = \frac{1}{2}$, filled atoms lie at $z = \frac{1}{2}$ (After Morosin and Lynch 1972).

2.3.2 Formation and Properties

Aluminium titanate or Al_2TiO_5 is a ceramic material which has low thermal expansion coefficient, high melting point, and low thermal conductivity. These characters make it appropriate for structural applications where thermal insulation and thermal shock resistance are required. Possibilities for utilising this material include use for components of internal combustion engines (Buscaglia *et al.* 1994; Thomas and Stevens 1989a) and casting clean metal alloys without residues.

AT may be formed through an equimolar reaction of alumina and titania (rutile) over 1280°C (Kato *et al.* 1980) - see Equation (1.2). Freudenberg and Mocellin (1987) studied the formation of AT by solid-state reaction. They observed several mechanisms operating during the reaction. In the initial reaction stage, nucleation of AT cells took place. The occurrence of this nucleation was confirmed by Buscaglia *et al.* (1994) and observed at 1345°C . In the final stage, elimination of Al_2O_3 and TiO_2 dispersoids, which were trapped during the previous stage, occurred through a diffusion-controlled mechanism. Buscaglia *et al.* (1994) showed that this final stage took place at approximately 1385°C .

Several investigations have been conducted to determine the linear thermal expansion coefficients of AT (Table 2.1). These values illustrate the extreme degree of anisotropy present in AT. This anisotropy creates a complicated internal stress during cooling from the firing temperature. As will be discussed later (Buessem 1952; Bush and Hummel 1959), the degree of anisotropy will influence the fracture strength. AT also exhibits thermal expansion hysteresis (Thomas and Stevens 1989a).

Table 2.1 Linear thermal expansion coefficient of aluminium titanate.

Linear thermal expansion coefficients (10^{-6} K^{-1})			Temperature	Reference
α_a	α_b	α_c		
11.8	19.4	-2.6	up to 1000°C	Buessem <i>et al.</i> (1952)
-3.0	11.8	21.8	up to 1020°C	Bayer (1971)
9.8	20.6	-1.4	room temperature	Morosin and Lynch (1972)

AT has two substantial problems withstanding its applications. The first problem is associated with its thermal instability at high temperatures. Kato *et al.* (1980) reported that AT decomposed into α -Al₂O₃ and TiO₂-rutile at $1280 \pm 1^\circ\text{C}$ according to



Several investigations have been undertaken to understand the reasons for this decomposition. Hennicke and Lingenberg (1986) suggested that the decomposition of AT occurred via metastable anosovite (Ti₃O₅). Experiments by Kameyama and Yamaguchi (1976) concluded that nucleation played a dominant role during the decomposition. This thermal instability can be controlled by adding MgO, SiO₂, and ZrO₂ (Wohlfromm *et al.* 1991; Ishitsuka *et al.* 1987). Study by Ishitsuka *et al.* (1987) showed that substitution of Al by Si or Mg was effective in controlling the thermal decomposition, but substitution of Ti by Zr had little effect. Tilloca (1991) and Battilana *et al.* (1995) showed that addition of iron oxide also enhanced the thermal stability of AT.

The second problem inherent in AT is related to extensive microcracking which develops during cooling from the sintering temperature. The microcracks were associated with the thermal expansion behaviour or the degree of thermal anisotropy (Buessem 1952; Bush and Hummel 1959). They explained that the microcracks preferentially occurred normal to the directions of high expansion caused by the development of tensile stresses.

Ohya *et al.* (1987) applied the energy criterion (Cleveland and Bradt 1987) to explain grain boundary microcracking in AT. Measuring the sample length changes and acoustic emission events during sintering and cooling, they found that the critical grain size of AT was about 1.4 μm and the temperature at which stress-relaxation ceased was the sintering temperature, i.e. 1500°C. Their analysis resulted in a suggestion that the critical grain size for AT was not a unique value but varied according to the sintering temperature. Ohya and Nakagawa (1996) measured the crack volume in aluminium titanate resulted from the thermal

expansion anisotropy. They found that porosity affected the grain-boundary cracking in aluminium titanate specimens.

The effects of additives upon AT properties, other than thermal instability, were also studied by several workers. For example, a study of the effects of MgO addition was conducted by Buscaglia *et al.* (1994) and it was shown that MgO eliminated the expansion process related to titanate formation and lowered the formation and starting sintering temperature of AT. Addition of MgO and ZrO₂ improved the bending strength of the composites (Thomas and Stevens 1989b). The increased strength was related to the distribution of fine particles of corundum, spinel, or zirconia at grain boundaries which would prevent grain growth and reduce microcracking. They also reported that a limited amount of less than 3 wt% of SiO₂ improved the strength of reaction-sintered AT.

The thermal and mechanical properties of AT are also affected by additives. Hamano *et al.* (1981) found that the thermal expansion and strength of AT increased with additive contents. For 5 wt% MgO addition, Ohya (1983) found that the thermal expansion of AT was $7 \times 10^{-6} \text{ K}^{-1}$ in comparison with the value for pure AT, $4.4 \times 10^{-6} \text{ K}^{-1}$. This significant increase shows that improving the mechanical strength of AT is not necessarily beneficial for its usual applications.

Runyan and Bennison (1991) showed that alumina-AT composites exhibited high flaw-tolerance. Flaw-tolerance is an important and desirable property of ceramic where flaw size and subsequent in-service damage do not influence its strength. Improvement of flaw-tolerance is represented by measures such as greater Weibull modulus (through R- or T- curve behaviour) and enhancement of fatigue limit. They synthesised the composites using conventional ceramic powder processing with two different sintering times (1 and 16 h) and measured the indentation-strength of the sintered composites. They found that both composites containing AT with grain size of 5.8 μm and of 14 μm (after 1 and 16 h sintering times, respectively) exhibited low sensitivity of strength to indentation load. This result shows that the composites have pronounced flaw-tolerance.

Another study on the characteristics of AT-based composites was conducted by Wohlfromm *et al.* (1991). They discussed the effect of dispersed monoclinic zirconia particles, occupying sites at triple points and grain boundaries, on the yield strength. Their study, using TEM observation, showed that the improvement of

the composite's strength was due to the ability of ZrO_2 particles to stop the crack propagation. As a result, the composite has a smaller flaw-size and thus a higher strength.

Braun *et al.* (1992) and Padture *et al.* (1993) studied the flaw-tolerance, indentation toughness, and crack-resistance of alumina-AT composites. In an AT-dispersed alumina composite (20 vol% AT), Braun *et al.* found that the alumina matrix with large grains and the presence of AT as a second phase (mean grain size of both phases was 6 μm) were important microstructural elements contributing to the pronounced flaw-tolerance of the composite. This prominent property was shown by the result that the strength of the composite was insensitive to the indentation load. Their SEM study showed that well-defined radial crack patterns around indentations were found. Strong crack deflections occurred at the interphase boundary as a result of strong tensile thermal expansion mismatch stresses. Compression stresses at the adjacent interphase facets enlarged the frictional grain-grain contacts at the separating walls. These created crack bridges and contributed to a shielding K-field (Braun *et al.* 1992).

Padture *et al.* (1993) also showed that significant improvement in flaw-tolerance (indicative of a strong T-curve) was achieved when 20 - 30 vol% AT was added into the alumina matrix both in "duplex" and "duplex-bimodal" systems. This improvement was shown by the decreasing dependence of the strength on the indentation load which indicated the T-curve behaviour. *In situ* SEM observation showed that crack growth provided direct evidence for grain-localised bridging in the crack wake. They concluded that the intense internal residual stresses induced by the thermal expansion mismatch has caused bridge-clamping stress and bridge formation which were responsible for the enhanced T-curve behaviour.

2.4 ALUMINA-ZIRCONIA SYSTEM

The following section discusses the crystal structures of alumina and zirconia polymorphs which is then followed by discussion on the mechanical properties of alumina-zirconia ceramic system.

2.4.1 Crystal Structures

Aluminium oxide (Al_2O_3) is found in several crystallographic forms (e.g., α , β , and γ - see Misra (1986)). The most widely used in structural application is α -alumina or corundum (with its single crystal sapphire). Corundum has a hexagonal close-packed crystal structure (Figure 2.12). Under a space group of R-3c, α -alumina has lattice parameters $a = b = 4.7602 \text{ \AA}$ and $c = 12.9933 \text{ \AA}$ (Lewis *et al.* 1982).

Zirconia is a polymorph with crystal structures of monoclinic, tetragonal, and cubic (e.g., Green *et al.* 1989, p17; Gasgnier 1992). It has also been recently observed that the *t*-structure can transform into orthorhombic (*o*-) structure. The *o*-structure was observed from the transformation of *t*-structure in Mg-PSZ ceramic when cooled (Kisi *et al.* 1989). They also observed the reverse transformation of *o* to *t* on subsequent heating. Figure 2.13 shows the crystal structures of the polymorphs of zirconia. The crystallographic parameters of the polymorphs are shown in Table 2.2.

Table 2.2 Crystallographic parameters of zirconia polymorphs.

Crystal Symmetry & space group	a (\AA)	b (\AA)	c (\AA)	Angle (deg)	Reference
Monoclinic $P2_1/c$	5.156	5.232	5.341	99.25	Smith and Newkirk (1965)
Tetragonal $P4_2/nmc$	3.64	3.64	5.27	-	Teufer (1962)
Cubic Fm-3m	5.13	5.13	5.13	-	Gasgnier (1992)
Orthorhombic $Pbc2_1$	5.068	5.260	5.077	-	Kisi <i>et al.</i> (1989)

2.4.2 Properties of Alumina-Zirconia Composite

The alumina-zirconia composite system has attracted material scientists' attention for decades due to its specific mechanical character, especially the presence of toughening behaviour (Green *et al.* 1989). Alumina is commonly used as the matrix and zirconia is the dispersed phase. The role of the inclusion of zirconia in the microstructure and the properties of alumina-based ceramic are discussed below.

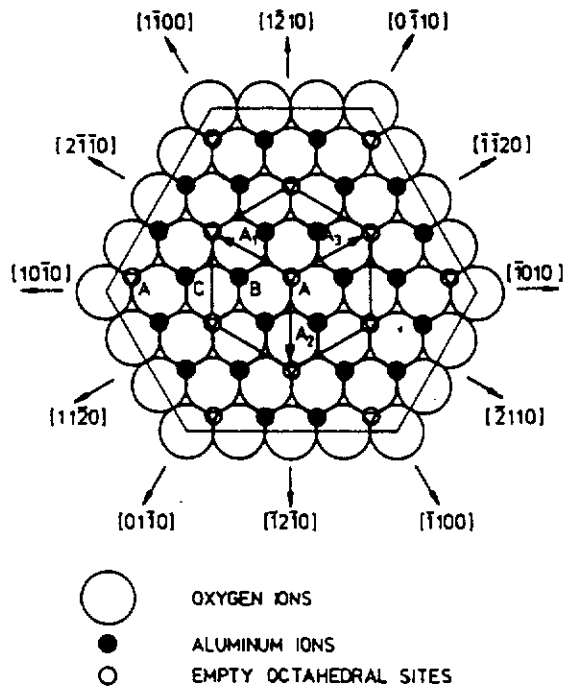
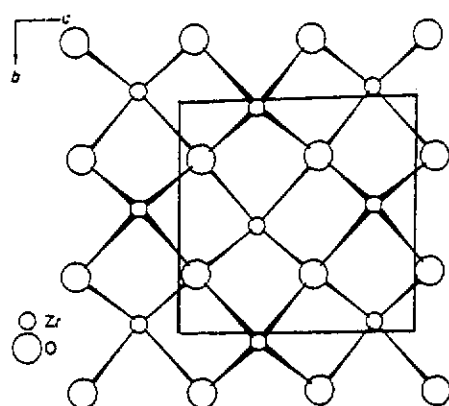
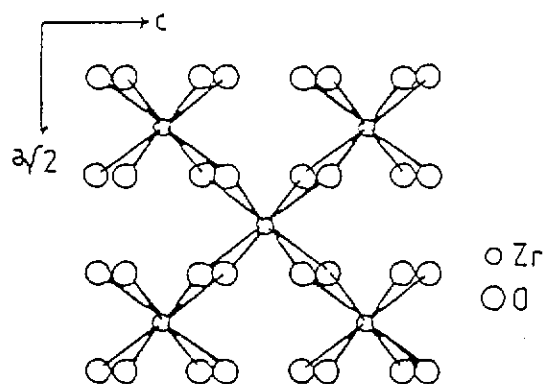


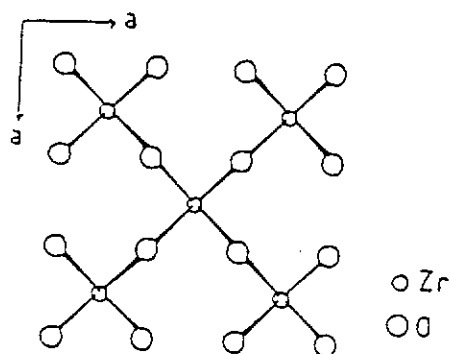
Figure 2.12 Crystal structure of α -alumina. Figure shows the packing of Al and O ions in the basal plane (After Dörre and Hübner 1984).



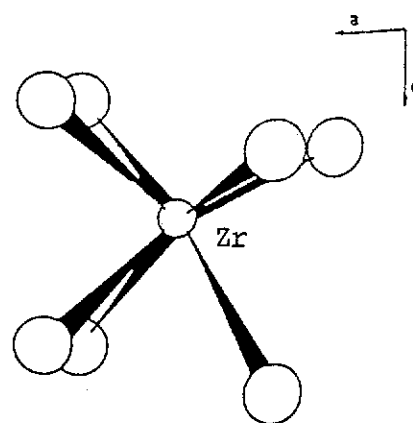
(a)



(b)



(c)



(d)

Figure 2.13 Crystal structure of zirconia polymorphs, (a) monoclinic, (b) tetragonal, (c) cubic and (d) orthorhombic (see Table 2.2 for references).

Alumina experiences grain growth during sintering which causes several disadvantages for its single-phase applications including porosity and exaggerated (or abnormal) grain growth. Introduction of a second phase may control the grain growth of alumina or promote sintering kinetics which leads to a fully-dense ceramic. Over 30 years ago, it was found that MgO was the most effective additive to prevent the discontinuous grain growth of alumina. Addition of 0.25 wt% MgO provided beneficial effects on both the densification rate and full density, i.e. final density was achieved (Coble 1961). Other effective sintering aids for alumina include NiO and TiO₂ (Dörre and Hübner 1984).

It was also found that addition of ZrO₂ was effective in inhibiting grain growth of alumina despite its inability to produce a ceramic with satisfying density (Lange and Hirlinger 1984; Sudre and Lange 1992). Addition of more than 5 vol% ZrO₂ controlled the grain growth of alumina from 6.9 µm in pure alumina to 2.82 µm in 5 vol% ZrO₂ system (Lange and Hirlinger 1984). The grain growth of ZrO₂ was believed to occur by coalescence. This led to the location of the ZrO₂ grains, mostly, at four-grain junctions. They also observed that above 1550°C some ZrO₂ grains were relocated to the interior of the alumina grains and became spherical. This occurrence was attributed to the growth of a group of alumina grains into a large grain which during the process swallowed up the small zirconia grains.

The most interesting aspect of the alumina-zirconia system is its pronounced fracture toughness (Claussen 1976; Green *et al.* 1989) which leads to the term zirconia-toughened alumina, or ZTA. Fracture toughness of the alumina-zirconia system may be up to 10 MPa.m^{1/2}, which is more than twice that of alumina ceramic alone (Claussen 1976). The toughening mechanism in ZTA is due to the martensitic *t*→*m* ZrO₂ transformation which is followed by the absorption of cracking energy so that crack propagation can be hindered. The transformation can be induced by a large tensile stress ahead of a crack tip. The mechanism is, therefore, called stress-induced transformation toughening (e.g., Green *et al.* 1989). Since *t*-ZrO₂ is unstable at room temperature, a certain amount of a stabiliser such as yttria, magnesia, ceria or calcia is added into the system. The strength of the alumina-zirconia ceramic depends on the zirconia particle size and presence of the metastable phase (Claussen 1976). In unstabilised dispersed-

zirconia alumina ceramic, the strength was retained if 1.25 μm zirconia particles were added up to 16 vol% but decreased for larger particle sizes. On the other hand, an yttria-stabilised-zirconia/alumina system showed improvement in strength with zirconia content. The hardness decreased with zirconia content.

Claussen (1976) showed that the fracture toughness of alumina with unstabilised monoclinic dispersed-zirconia improved by a factor of 2. The responsible mechanism for the improvement was thought to be a subcritical crack propagation and crack opening. The microcracks were produced by the expansion of ZrO_2 particles during the $t \rightarrow m$ transformation upon cooling. The residual stresses developed in the matrix led to the behaviour of small ZrO_2 particles as crack formers which reduced the size of internal flaws.

2.5 QUANTITATIVE PHASE ANALYSIS USING X-RAY DIFFRACTION

2.5.1 Introduction

X-ray powder diffraction is a powerful tool to determine the structure and composition of phases present in a material (Klug and Alexander 1974; Cullity 1978). The reference intensity ratio (RIR) method (e.g., Hubbard *et al.* 1976) is one of the methods which have been developed to determine phase composition by making use of the intensity of one or more lines of each phase in a diffraction pattern. A full-pattern refinement method, designated the Rietveld method, was originally developed by Rietveld (1969) to refine crystal structures with powder diffraction data. Subsequently, it was realised that Rietveld refinement method was also a powerful tool for quantitative phase analysis. The main drawbacks of the RIR method over the Rietveld method is that the former does not have capacity to deal with overlapping peaks. From this viewpoint, the Rietveld method has been utilised in the present work. The Rietveld refinement method for quantitative phase analysis is reviewed below.

2.5.2 Rietveld Refinement

Rietveld analysis is a least-square-based refinement method to which aims to obtain the best fit between the observed powder diffraction pattern and the calculated pattern. Rietveld (1967, 1969) initially proposed the use of this “whole-pattern” method to refine structural parameters for polycrystal samples. This

method has been developed to provide composition information (e.g., Hill and Howard 1987; Bish and Howard 1988; O'Connor and Raven 1988). The method is applicable to patterns produced with x-ray, neutron and synchrotron radiation.

Attractions of the method for phase composition analysis (Hill 1993) include:

1. capacity to deal with overlapping lines
2. inclusion of all reflections, thus reducing the preferred orientation and extinction effects,
3. ability to apply background profile function for whole pattern, producing a better definition of peak intensities, and

In the least-square procedure, a model is presumed to be optimum when the sum (S) of the squares of the differences between the measured and the calculated patterns is lowest, that is when

$$S = \sum_i w_i (y_i - y_{ic})^2 \quad (2.12)$$

reaches a minimum. Here, y_i is the observed step intensity, y_{ic} is the corresponding calculated value, and w_i is the weighting factor for point i in the pattern which is normally set as the reciprocal of the variance of the measured intensity at point i , i.e. $w_i = 1/\sigma_i^2$. The calculated intensity is given by summing the contribution from (i) neighbouring Bragg reflections, (ii) background (assuming the crystallites are randomly oriented). For Bragg-Brentano XRPD optics and infinitely thick specimens, the expression for the calculated intensity follows

$$y_{ic} = (K / \mu) \sum_{jk} \left[m_{jk} L_{jk} |F_{jk}|^2 \phi_{ijk} P_{jk} \left(C_k / V_k^2 \right) \right] + y_{ib} \quad (2.13)$$

where K is a constant which is instrumental-dependent, μ is the linear attenuation coefficient of the specimen, m_{jk} is the multiplicity factor, L_{jk} is the Lorentz-polarisation-multiplicity factor for line j of phase k , $|F_{jk}|$ is the structure amplitude, ϕ_{ijk} is the peak shape function, P_{jk} is the preferred orientation function,

C_k is the volume fraction of phase k , V_k is the corresponding unit cell volume and y_{ib} is the background contribution.

The pseudo-Voigt (or Lorentzian-Gaussian) peak shape function

$$\varphi_{ijk} = \frac{2\gamma}{\pi \cdot H_k} \times \frac{1}{\left[1 + \frac{4(2\theta_{ik} - 2\theta_{jk})^2}{H_{jk}^2} \right]} + \frac{(1-\gamma)C_G}{\sqrt{\pi}H_k} \exp\left[-\frac{C_G(2\theta_{ik} - 2\theta_{jk})^2}{H_{jk}^2} \right] \quad (2.14)$$

is commonly used in the refinement of x-ray diffraction pattern since it is relatively simple to calculate. Here, $C_G = 4 \ln 2$, γ is a refinable ‘mixing’ parameter, H_{jk} is the full-width at half-maximum (FWHM) for Bragg peak j of component k . This function varies with angle according to (Caglioti *et al.* 1958)

$$H_{jk} = \left(U_k \tan^2 \theta_{jk} + V_k \tan \theta_{jk} + W_k \right)^{1/2} \quad (2.15)$$

where U , V , and W are peak function parameters.

The profile function can be corrected for peak asymmetry using the semi-empirical function proposed by Rietveld (1969)

$$A_{ik} = 1 - AS[\text{sign}(2\theta_i - 2\theta_k)](2\theta_i - 2\theta_k)^2 \cot \theta_k \quad (2.16)$$

AS is the asymmetry parameter to be determined from the refinement.

Preferred orientation effect may cause systematic error in quantitative phase analysis using x-ray diffraction method. The preferred orientation parameter, P_{jk} , corrects for the platelet-like crystallites in the specimen by applying the March function following Dollase (1986)

$$P_{jk} = \left(G_1^2 \cos^2 \alpha + (1/G_1) \sin^2 \alpha \right)^{-3/2} \quad (2.17)$$

where G_I is a parameter and α is the acute angle between the scattering vector and the normal to the crystallites. It should be noted here that processing (e.g. pressing) may provide substantial preferred orientation bias (Sitepu 1991).

The pattern background may be modelled using the polynomial

$$y_{bi} = B_0 + B_1(2\theta_i) + B_2(2\theta_i)^2 + B_3(2\theta_i)^3 \quad (2.18)$$

where B_0 , B_1 , B_2 , and B_3 are polynomial coefficients and 2θ is the diffraction angle.

Several figures-of-merit or R-values are used to assess the success of the refinement procedure. These are (Young 1993; Kisi 1994):

(i) the profile R factor:

$$R_p = \frac{\sum |y_i - y_{ic}|}{\sum y_i} \quad (2.19)$$

(ii) the weighted profile R factor:

$$R_{wp} = \left[\frac{\sum w_i (y_i - y_{ic})^2}{\sum w_i y_i^2} \right]^{1/2} \quad (2.20)$$

(iii) the expected R factor

$$R_{wp} = \left[\frac{N - P}{\sum w_i y_i^2} \right]^{1/2} \quad (2.21)$$

where $N-P$ is the weighted sum of squared residuals.

(iv) the “goodness-of-fit” indicator (GoF)

$$GoF = \left[\frac{R_{wp}}{R_{exp}} \right]^2 \quad (2.22)$$

The ideal value for GoF is 1.0. For phase analysis, a value of less than 4.0 is acceptable (Kisi 1994).

(v) the Bragg R-factor for each phase

$$R_B = \frac{\sum |I_i - I_{ic}|}{\sum I_i} \quad (2.23)$$

where I_i and I_{ic} are the *observed* and calculated intensities for a Bragg reflection. The *observed* Bragg intensities here are determined assuming they are in the same proportion as their calculated counterparts determined using structural model.

(vi) difference plot between the observed and calculated patterns is also important for assessing the refinement quality. The two patterns should essentially give a flat difference for a well refined model. The difference plots may also provide indications of the presence of previously undetected phase(s) or inaccuracies in the background or peak shape modelling.

2.5.4 Quantitative Phase Analysis using Rietveld Method

The use of Rietveld analysis to accurately estimate the relative and/or absolute abundance of phases in mixtures has been shown by various researchers (e.g., Hill and Howard 1987; Bish and Howard 1988; O'Connor and Raven 1988). For Bragg-Brentano diffractometry, Equation (2.16) can be simplified (Hill and Howard 1986) as

$$y_{ic} = \sum s_k m_{jk} L_{jk} |F_{jk}|^2 G_{jk} P_{jk} + y_{ib} \quad (2.24)$$

where $s_k = \frac{K \cdot C_k}{\mu \cdot V_k}$ is the Rietveld scale factor for phase k .

Hill and Howard (1987) made use of the scale factor s for phase abundance calculation, i.e.

$$C_k = \frac{\mu \cdot V_k}{K} s_k \quad (2.25).$$

Weight fraction of a phase W can be related to volume fraction C as $W = \rho C$. Since $\rho V^2 = ZMV$, where Z is the number of formula units per unit cell, M is the mass of the formula unit, and V is the unit cell volume, from Equation (2.25), the weight fraction of a phase k can be expressed as

$$W_k = \frac{\mu \cdot \rho_k \cdot V_k}{K} s_k = \frac{\mu}{K} (ZMV)_k \cdot s_k \quad (2.26).$$

The relative weight fraction of a phase (if the amorphous content is negligible) is then

$$W_k = \frac{s_k (ZMV)_k}{\sum_{j=1}^n s_j (ZMV)_j} \quad (2.27).$$

Absolute weight fraction of a phase can also be determined using Rietveld method (O'Connor and Raven 1988). The instrument constant K in Equation (2.28) was determined after a subsequent experiment with similar conditions was conducted. In determining the compositions, they made use of iterative trial and error calculations since the MAC value was not measured. Independent measurements of MAC were suggested which included:

- (i) accurate elemental data measured by x-ray fluorescence spectrometry
- (ii) narrow beam attenuation (Norrish and Chappell 1977)
- (iii) Compton scattering measurement (Reynolds 1963)

In the present work, absolute weight fraction of phases in the FGM and reference specimens was determined using external standard x-ray diffraction Rietveld method. Equation (3.7) was used for the analysis. The mass attenuation coefficient values were corrected utilising Compton scatter measurement. More detailed procedure of the experiments is described in section 3.3.2.

CHAPTER 3

EXPERIMENTAL METHODS

3.1 EXPERIMENTAL DESIGN

Experiments were designed to ensure that the objectives of the project outlined on section 1.2 were achieved. The experimental design consists of three components, (i) *processing* of the FGM, (ii) *characterisation* of its graded profile and (iii) *properties and microstructure* observation.

3.1.1 Processing

The first important step in the processing of the material was to produce homogeneous and narrow distribution particle size alumina-zirconia mixture. Attrition milling was selected for this purpose because of its ability to break down the spray-dried alumina and zirconia powders in short periods of time and provide homogeneous powder mixture with fine particle size and narrow size distribution. The break down of the spray-dried powders was regarded to be important in terms of reaction between alumina and rutile. The latter phase would be introduced via liquid infiltration and heating.

The formation of the powder mixture into shapes would render the possibility of reproducing compacted mixture for structural applications. Uniaxial pressing at a moderate pressure was chosen for bar shape formation to produce powder compacts with reasonable porosity which was important in the infiltration process. The strength of the pressed powders was another important aspect of liquid infiltration. The procedure selected for this purpose was pre-sintering the compacts at a temperature when the initial densification occurred. The infiltration was carried out in order to introduce a new material (i.e. TiO_2) into the preform.

The firing step was an important experimental element which would allow reaction(s) and densification to occur. From this point of view, the sintering temperature and time were carefully selected to make possible the formation of AT and also to achieve reasonable densification.

3.1.2 Characterisation

Microstructural characterisation was an important feature of the experiments in view of the pronounced influence of microstructure on various properties. A differential thermal analysis was employed to monitor the formation of AT during synthesis of the AT/zirconia-alumina FGM. X-ray diffractometry was also employed to monitor the formation of AT.

Characterisation of the FGM graded profile was of fundamental importance in the study. Construction of the graded composition profiles involved various techniques. The Rietveld method was selected as the primary technique for determining phase distribution. Back-scattered electron microscopy and electron-probe microanalyzer were also employed to qualitatively verify the elemental (and hence the phase) distribution.

3.1.3 Properties and Microstructure

The final part of the experiment was the assessment of properties and microstructure, i.e. two intimately related elements in a material. The experiment focussed on the thermal and mechanical properties of the FGM. Thermal expansion and decomposition studies were conducted to observe the change of thermal expansion with depth and the effect of zirconia in stabilising AT. High-temperature neutron diffraction data were collected in an effort to explain the non-linear thermal expansion behaviour of the FGM.

The assessment of mechanical properties involved Young's modulus, microhardness, indentation fracture toughness, and Hertzian contact response. Microhardness measurements were conducted at various depths and loads. These tests, together with compositional analysis, would allow investigation of the correlation between graded compositional character and mechanical properties. Indentation fracture toughness was examined only qualitatively due to the difficulty in observing the indentation cracks. Hertzian contact testing was conducted to study the stress-strain relationships and also subsurface damage behaviour.

The value of investigating the microstructural features of a material relies on their use in examining the relationships between properties and microstructure. Features such as grain size and shape, microcracks, porosity, and damages can be

revealed from optical and electron microscopy. A microstructural study of the FGM was therefore conducted using Nomarski optical (for subsurface damage) and scanning electron microscopy.

3.2 MATERIAL PROCESSING

3.2.1 Powder Processing

The starting materials used in the experiment consisted of:

- (i) high-purity α -alumina (α -Al₂O₃) powder, A1000SG grade Alcoa (USA), of median particle size 0.39 μ m,
- (ii) high-purity, spray-dried monoclinic zirconia (ZrO₂) powder, SF Ultra Z-Tech (Australia), of median particle size 0.40 μ m,
- (iii) a solution containing 30 (w/v) % titanium tetrachloride (TiCl₄), BDH Limited Poole, England.

ZrO₂ powder (40 g) was mixed with 100 mL de-ionized water and sufficient ammonium hydroxide (NH₄OH) to take the pH up to 10-12 in order to facilitate the break up of the spray-dried agglomerated grains. Small alumina (99.9% purity) milling balls (100 g) were put into the slurry. The slurry was then stirred for 1.75 h. Al₂O₃ (360 g) was then added with 300 mL of de-ionized water, 250 g of small milling balls, and 5 g of polyethylene glycol as a binder. The mixture was then attrition milled for 45 minutes at a speed of 300 rpm.

The as-milled mixture was dried in an oven at 100°C for 48 h. The dried mixture was then sieved until free-flowing with 710, 150 or 125, 75, and 45 μ m grid-size sieves.

The powder mixture was pressed uniaxially in a metal die at a pressure of 15 MPa to yield a bar sample of height 5 mm, width 12 mm and length 60 mm. A partial sintering at 1000°C was then used to increase its strength but maintain the porosity prior to infiltration. The apparent porosity (P_a) and bulk density (D_{as}) of the samples were measured following the Australian Standard AS 1774.5, i.e.

$$P_a = \frac{m_s - m_D}{m_s - m_i} \times 100 \quad (3.1)$$

$$D_{as} = \frac{m_D}{m_D - m_i} \times D_i \quad (3.2)$$

where m_D is the mass of dried specimen, m_i is the mass of the test specimen, saturated with and suspended in liquid, m_s is the mass of the test specimen, saturated with liquid and suspended in air, and D_i is the density of the immersion liquid at the temperature prevailing during the test. In the present work, de-ionized water was used, $D_i = 997 \text{ kgm}^{-3}$ (Hansson 1972).

3.2.2 Ceramic Processing

The pre-sintered green bodies were 46% porous and robust for infiltration. The dimensions and mass of the preforms before infiltration were measured using a vernier calliper (Toledo) with a nominal accuracy of $\pm 0.01 \text{ mm}$ and a precision top loading balance (FR 200, A&D Company, with nominal accuracy of $\pm 0.0001 \text{ g}$), respectively. The TiCl_4 -contained solution was poured into a plastic container so that the green bodies could be fully immersed during infiltration. The infiltration process was conducted at room temperature for 24 h. The samples were turned over twice during infiltration to ensure uniform liquid diffusion throughout the bodies. The infiltrated preforms were then dried at $70\text{-}80^\circ\text{C}$ for 24 h. They were finally heat-treated in a Ceramic Engineering (Model HT 04/17) high-temperature furnace following the schedule below:

- 1°C min^{-1} to 450°C for 30 mins. This stage was used to allow decomposition of organic materials (binder) and removal of residual water.
- 5°C min^{-1} to 1550°C for 3 h. This step was used to densify the bodies and allow the formation of aluminum titanate.
- furnace cooled.

Control samples were not infiltrated with the solution, but were sintered following the same heating schedule.

The dimensions, mass, apparent porosity and bulk density of the sintered samples were measured. The percent reduction in volume was used to determine the shrinkage (S) values of samples, i.e.

$$S = \frac{(V_i - V_f)}{V_i} \quad (3.3)$$

where V_i is volume before infiltration and V_f is volume after infiltration and sintering.

3.3 CHARACTERISATION

3.3.1 Differential Thermal Analysis (DTA)

Differential thermal analysis was conducted to monitor the formation of aluminium titanate. A piece of zirconia-alumina preform (approximate weight 0.1 g) was immersed in the TiCl_4 -contained solution and then dried in air. The piece was then analysed with a Stanton Redcroft STA-780 thermal analyzer. The sample was heated to 1500°C in flowing air at a rate $10^\circ \text{Cmin}^{-1}$. High purity Al_2O_3 powder was used as a reference.

3.3.2 Phase Analysis

X-ray Powder Diffraction Pattern Collection

X-ray diffraction data were collected with a Siemens D500 Bragg-Brentano instrument. An infiltrated, as-fired sample was cut into 10 mm x 10 mm x 3 mm (thickness) dimensions. To obtain the graded composition profile, the x-ray data were collected from the sample at depths of 0.0, 0.1, 0.2, 0.3, 0.4, 0.8, 1.2, and 1.5 mm. The sub-surface measurements were made after polishing away the material to the designated depth. Samples were mounted on aluminium sample holders using a viscous adhesive (BlueTack, Bostik Australia Pty. Ltd.). The height of each sample was adjusted using a glass slide.

The following operating conditions were utilised: $\text{CuK}\alpha$ radiation ($\lambda = 1.5418 \text{ \AA}$) produced at 40 kV and 30 mA, 0.3° divergence for the incident beam and 0.15° receiving slit, goniometer range = $17\text{--}100^\circ$, step size = 0.04° , counting time = 2 s/step, and post-diffraction graphite monochromator with NaI detector and PHA. The computer program DCM (SOCABIM, France) was used to store the diffraction data into the computer disk.

The use of 0.3° incident beam divergence was to obtain an accurate intensity measurement at small Bragg angles as suggested by Klug and Alexander (1974, p371); see Figure 3.1. The x-ray beam will be entirely received by the sample surface if

$$\sin(\gamma l / 2A) \leq \theta \quad (3.4)$$

where θ is the incident angle, γ is the incident beam divergence, l is the goniometer radius, and $2A$ is the sample size. Since the sample width was only about 10 mm, $l \cong 200.5$ mm, and the first diffraction line of a phase (aluminum titanate) appeared at $2\theta \cong 18^\circ$, the beam divergence of 0.3° was chosen. The sample size was then selected as $2A = 7.10$ mm (starting $2\theta = 17^\circ$).

Manual and computer-based search-match procedure was applied to identify the diffraction peaks and thus phases present in the sample. The International Centre for Diffraction Data (ICDD) diffraction pattern database and computerised Micro-ID search-match program (Materials Data Inc.) were employed for the identification.

The raw data collected from the diffractometer were converted to ASCII data using RAWASC software provided by SOCABIM (France). The data were then utilised for quantitative phase analysis using the Rietveld refinement.

Rietveld Refinement

The refinement was conducted with the parameters as shown in Table 3.1. The scale factor (s) was the parameter for quantitative analysis. The overall temperature factor (B) and position coordinates (x , y , and z) were refined only for AT because of the lack of satisfactory crystal data from the literature.

In present work, the input model for parameters, i.e. space group, lattice parameters (a , b , c , α , β , and γ), position coordinates for each atom in a phase (x , y , and z), and thermal factors (B) of each phase was adopted from the following references:

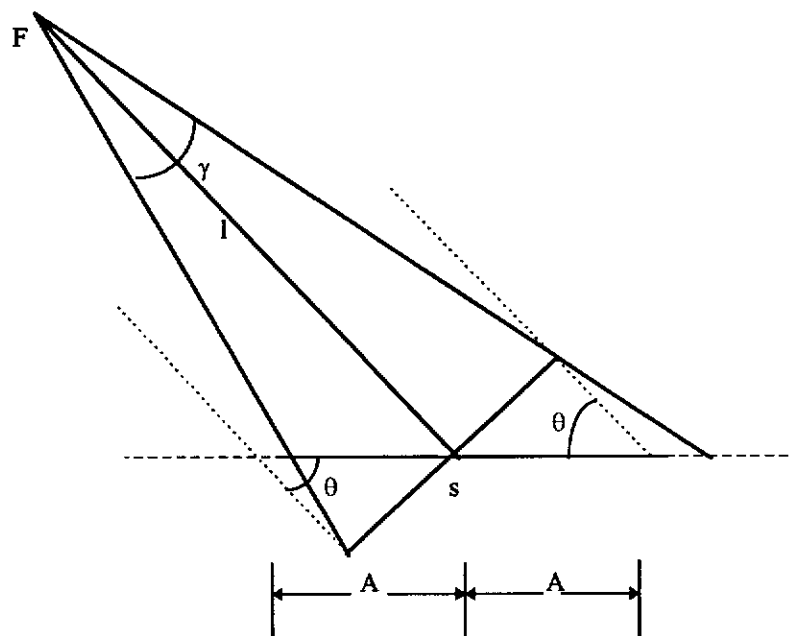


Figure 3.1 X-ray beam related to the geometry of a sample
(After Klug and Alexander 1974, p371).

Table 3.1 The refinable parameters for phase analysis.

Parameter	Symbol	Note
Scale factor	s	All phases
Profile parameters	u, v, w	All phases
Lattice parameters	a, b, c	All phases
Preferred orientation	PO	All phases
Overall thermal parameter	B	Only for AT
Position coordinates	x, y, z	Only for AT
2 θ -zero	$\Delta 2\theta$	Global
Background function	B_0, B_1, B_2	Global

	Phase	Reference
1	α -Al ₂ O ₃	Lewis <i>et al.</i> (1982)
2	monoclinic ZrO ₂	Smith and Newkirk (1965)
3	aluminum titanate	Austin and Schwartz (1953)
4	tetragonal ZrO ₂	Teufer (1962)

The crystallographic data for each phase used in the refinements are presented in Appendix 1. The refinements were conducted using a Rietveld refinement program LHPM written by Hill and Howard (1986).

Quantitative Phase Analysis using Rietveld Method

In this experiment, an external standard method and direct measurement of MAC were used to determine the phases weight fractions at various depths of the specimen. The external standard was high-purity alumina powder (Praxair Surface Tech. Inc., grain size of 1.0 μ m). The powder was ball milled for 30 mins to obtain narrow grain distribution. Assuming that the external standard is 100% crystalline, using the expression (2.27) (O'Connor and Raven 1988)

$$W_s = 1 = \frac{s_s \rho_s V_s^2 \mu_s}{K} \quad (3.5)$$

where subscript *s* designates the (external) standard. Comparing the two expression leads to the basic equation for determining the absolute weight fraction of phase *i* using external standard

$$W_i = \frac{s_i \rho_i V_i^2 \mu}{s_s \rho_s V_s^2 \mu_s} \quad (3.6)$$

Since $\rho V^2 = ZMV$ (see for example Hill (1991), Equation (3.6) can be written as

$$W_i = \frac{s_i(ZMV)_i \mu}{s_s(ZMV)_s \mu_s} \quad (3.7)$$

The μ value was determined by x-ray fluorescence spectrometry using Compton scattering measurements. Detail procedure of this measurement is explained in the following section.

The level of amorphous phase in the sample was estimated using the assumption that the total sum of the crystalline and amorphous phases concentration was unity. On this basis, the weight fraction of the amorphous phase (W_G) is

$$W_G = 1 - \sum_{i=1}^n W_{ci} \quad (3.8)$$

where W_{ci} is the absolute weight fraction of crystalline phase i and n is the number of crystalline phases present in the specimen.

Since the MAC of a specimen is the summation of the multiplicity between MAC and absolute weight fraction of each phase over all phases, the MAC of the amorphous phase can be determined by

$$\mu_G = \frac{\mu - \sum_{i=1}^n \mu_i W_{ci}}{W_G} \quad (3.9)$$

where n is the number of crystalline phases.

Mass Attenuation Coefficient Measurement

As indicated by O'Connor and Raven (1988), the MAC of a specimen can be determined by x-ray spectroscopy Compton scatter measurements. O'Connor and Chang (1985) used the Compton scattered line of a filtered primary beam of MoK α radiation to estimate MAC values. Compton scatter can be used to estimate

MACs at wavelength λ according to the peak intensity of the Compton scatter profile I_C as

$$\mu_\lambda = \frac{k_\lambda}{I_C} \quad \text{or} \quad \mu_\lambda \propto \frac{1}{I_C} \quad (3.10)$$

provided that no absorption edge effects occur between the wavelength and the measured Compton line.

Measurements were conducted on the functionally-graded AT/zirconia-alumina composite. Compton scatter intensities were collected at the surface, and at 0.1, 0.2, 0.3, 0.4, 0.8, 1.2, and 1.5 mm depths after polishing the sample to the designated depth. Various compositions of zirconia-alumina powders were used as “standards”. The conditions of the measurement are shown in Table 3.2.

Table 3.2 Compton scatter measurement conditions.

Instrument	Siemens SRS200 wavelength-dispersive type
X-ray tube	Mo anode
Generating voltage	60 kV at 40 mA
Spectral line	MoK α ($\lambda = 0.709 \text{ \AA}$)
Crystal	LiF200
Primary beam aperture	8 mm (diameter)
Detector	Scintillation (NaI)
Single Channel Analyser	530 kV, 1.7 and 0.8 window and lower level
Counting time	4 s (chosen to provide 1% accuracy in the counting statistics)

The measurement procedure is as follows:

- (i) The Compton line was determined from measurement of intensities around where the theoretical Compton (MoK α) line would exist. Possible overlapping peaks and edge effects were carefully considered to avoid systematic errors.

- (ii) “Standard” samples of alumina-zirconia (pressed powders) were made with ZrO_2 contents 0, 5, 10, 15, and 20 wt%. Compton scatter intensities (I_C 's) of the standards were collected from the $\text{MoK}\alpha$ line and then the values were plotted versus I/μ . The plot provided a calibration curve by which the MACs of the samples could be estimated at the wavelength of the Compton scatter line.
- (iii) Compton scatter intensity of the sample at each depth was collected. The calibration curve from step (ii) was used to estimate the MAC value of the sample at the $\text{Mo-K}\alpha$ wavelength.
- (iv) The MAC values were converted from those at the $\text{MoK}\alpha$ to those at the $\text{CuK}\alpha$ wavelength, i.e. radiation used for XRD data collection, using a conversion curve developed for the MAC values between the two radiation.

Electron-probe Microanalysis

Scanning electron microscopy (SEM) and microprobe analysis were used to qualitatively display the graded profile of the FGM sample. A sample of $3.5 \times 6.0 \times 1.5 \text{ mm}^3$ was obtained by cutting the as-fired sample. The sample was mounted into an acrylic support (Transoptic Powder, Buehler, USA). The cross-sectioned surface was polished using a Struers Pedamat polisher employing 20 and 10 μm (diamond pads); and, 15, 9, 6, 3, and 1 (diamond paste) polishers. The polishing conditions were 200 rpm speed, 5-15 N load, and 2-10 mins polishing time. The sample was then removed from the mounting by heating in a microwave oven at approximately 200°C .

For microanalysis, the sample was placed in a sample holder for SEM observation and then carbon coated. This coating was applied to avoid interference of high atomic number coating element with the elements in the specimen. X-ray mapping and SEM pictures of the cross-sectioned sample were then collected.

Point-by-point measurements were made using the energy dispersive spectrometry with an accelerating voltage of 20 kV and specimen current of 0.1 μA . A beam size of 50 μm was used. The step size was 50 μm . The recording time for each position was 50 s. Aluminium, titanium, and zirconium characteristic x-ray emissions were recorded at each step.

Neutron Powder Diffraction

Neutron powder diffraction (Howard and Kennedy 1994) data was collected from the as-fired sample at various temperatures to explain the anomalous thermal expansion behaviour of the material at high temperature. The data collection was conducted at the High Flux Australian Reactor (HIFAR) operated by the Australian Nuclear Science and Technology Organisation (ANSTO), Lucas Height Research Laboratory, New South Wales. The following operating conditions were followed: $\lambda = 1.664 \text{ \AA}$ using the medium resolution powder diffractometer (MRPD), 2θ range = $5 - 138^\circ$, step size = 0.1° , counting time $\approx 40\text{-}50 \text{ s}$ per step, 8 monochromator of Ge crystals [(115) reflection], and 15-24 He^3 detectors 4° apart. Neutron diffraction patterns of the FGM at room temperature, 750°C , 850°C , and 1000°C were collected. Access to the facility was provided by the Australian Institute of Nuclear Science and Engineering (AINSE) - see acknowledgements.

3.4 THERMAL PROPERTIES

3.4.1 Thermal Expansion Behaviour

Four samples ($20 \times 3 \times 3 \text{ mm}^3$ in dimensions) were prepared for thermal expansion coefficient (TEC) measurements, i.e. an as-fired AT/zirconia-alumina FGM sample, 0.3 and 0.5 mm-polished FGM samples and a zirconia-alumina control (10 wt% ZrO_2) sample. The effect of surface layer on the TEC of FGM sample was analysed by its removal through polishing. The TEC measurement was conducted using a Rigaku Thermal Measurement Apparatus, located at the Niihara Laboratory of Osaka University in Japan. The measurement conditions were air atmosphere, $10^\circ\text{C}/\text{min}$ rate, 0.6 s sampling time, and Al_2O_3 as reference sample.

3.4.2 Decomposition Study of Aluminum Titanate

Some AT/zirconia-alumina FGM samples were prepared for decomposition study of aluminum titanate. The study was conducted using a high-temperature furnace (Ceramic Engineering HT 04/17) and an x-ray diffractometer (Siemens D500). X-ray diffraction patterns were collected from the samples which had been

annealed at 1050°C for 0, 2, 4, and 6 h. The decomposition rate was determined using integrated intensity ratios (AT:alumina) and (rutile:alumina). The alumina (024), AT (023), and rutile (110) peaks were selected for the study (Hwang *et al.* 1994).

3.5 MECHANICAL PROPERTIES

3.5.1 Microhardness and Fracture Toughness

The samples prepared for microhardness and fracture toughness measurements consisted of AT/zirconia-alumina FGM and one zirconia-alumina ceramic as a control. Preparation of samples was similar to that for electron probe microanalysis (sub-section 3.3.2), i.e. the samples were polished to a 1 µm surface finish.

Indentations along the cross-section were made using a ZWICK microhardness tester with Vickers diamond pyramid indenter at loads from 10 N to 100 N. For the FGM sample, the impressions were performed at 100, 300, 600, and 1200 µm depths. At least three indentations were made for both hardness and fracture toughness. The lengths of both diagonals of the indentation and radial cracks were measured using the calibrated ruler inside the eye-piece.

Microhardness variation with load was measured in both materials after polishing up to 1 µm surface finish. The polishing was carefully undertaken so that less than 0.2 mm surface layer was removed. Indentation loads from 2 to 100 N were applied to the specimens.

The hardness was determined using

$$H_v = 1.854F/d^2 \quad (3.11)$$

where F is load (N) and d is average length of diagonals (m). The fracture toughness at various loads was calculated using (Evans and Charles 1980)

$$K_{ic} = 0.16H_v(d/2)^{1/2}(2c/d)^{-3/2} \quad (3.12)$$

where c is radial crack length (m) - see Figure 3.2.

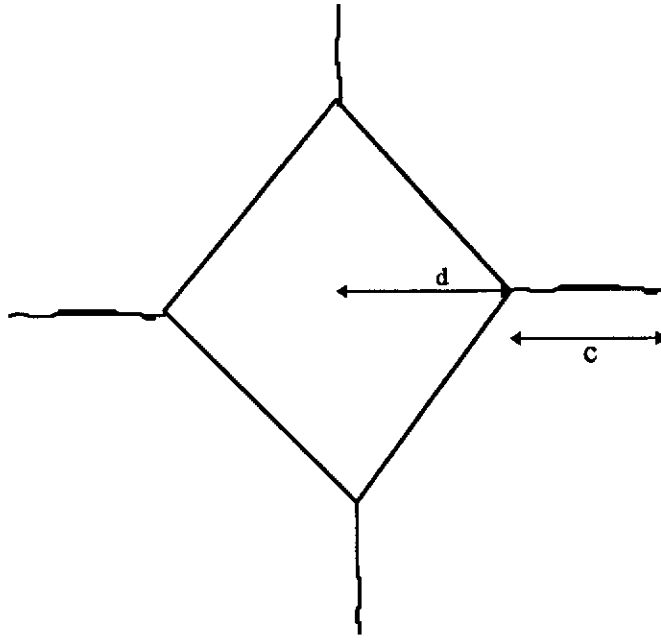


Figure 3.2 Vickers microhardness indentation. Measurement of the impression's diagonals, d , and crack-lengths, c , allows the determination of hardness and fracture toughness.

3.5.2 Young's Modulus

Bar samples with dimensions $3 \times 10 \times 50 \text{ mm}^3$ were prepared for Young's modulus measurement which was conducted using a flexural resonance vibration method (Fukui *et al.* 1994) at ambient conditions. The bar samples were coated with graphite on one side to act as an electrode and suspended on two thin tungsten wires in correspondence of the nodal points. The resonance frequency was recorded and the Young's modulus (E) was calculated using:

$$E = 0.9468 \frac{L^3 P f^2}{d^3 w} \quad (3.13)$$

where L is the sample length, d is thickness, w is width, P is weight, and f is resonance frequency. Depth profiling of Young's modulus was evaluated by gradually polishing away the surface of the sample. The experiment was conducted at the Niihara Laboratory of Osaka University.

3.5.3 Contact Hertzian Response

Tungsten carbide spheres were used to make the Hertzian indentations. The indentations were made on polished functionally-graded aluminium titanate/zirconia-alumina (approximately at 0.2 mm depth) and zirconia-alumina bar samples (Figure 3.3). The surfaces were gold coated before indentation to facilitate measurement of residual contact radius, a . The measurement enabled determination of an indentation stress, $p_0 = P/\pi a$, and indentation strain, a/r , for each contact. The stress-strain curves were constructed after data collection over a range of sphere radius from $r = 1.59$ to 12.7 mm at loads up to $P = 3000$ N. Hertzian contact damage experiments were conducted on similar bar samples, using a tungsten carbide sphere of radius 3.18 mm. The tests were conducted using the bonded-interface configuration shown in Figure 3.3, to provide information on subsurface damage. These samples were prepared by bonding two edge-polished rectangular half-blocks together with a thin ($< 10 \mu\text{m}$) layer of adhesive. Indentations were made symmetrically across the trace of the bonded interface on the polished top surface. The specimens were then immersed in a solvent to dissolve the adhesive and expose the section beneath the indentations. Single cycle tests were conducted at slow loading rates, typically over a period of ~ 100 s. The indented sections were coated with a thin layer of gold and were viewed with an optical microscope in Nomarski illumination to reveal the macroscopic damage patterns. This contact damage experiment was conducted at the National Institute of Standards and Technology, USA.

3.6 MICROSTRUCTURE

A cross-sectioned FGM sample, as used in the electron probe microanalysis experiment, was prepared for microstructural study. The sample was thermally etched at 1500°C for 10 mins to reveal grain boundaries. The temperature was chosen to avoid the decomposition temperature range of aluminium titanate, i.e. between 900 - 1200°C . The samples were mounted on a sample holder and gold coated for 1 minute at 50 mA. Micrographs were taken using a JEOL 35C electron

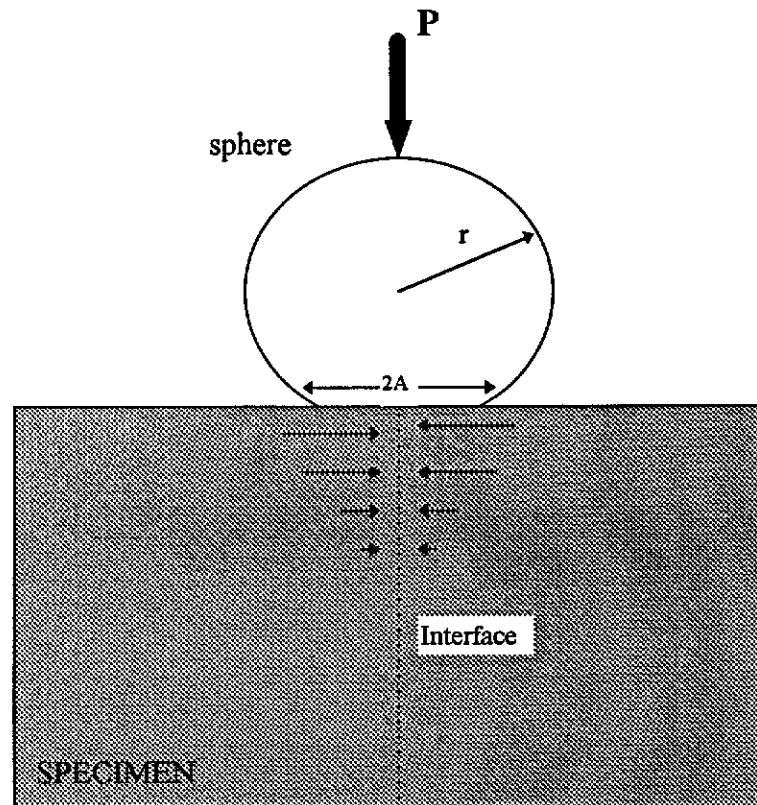


Figure 3.3 Contact Hertzian test of a material. A load P is delivered by a tungsten carbide sphere (radius r) over contact radius of a . Two polished halves of the specimen are bonded together, and the load P is applied on the interface (After Cai *et al* 1994).

microscope at 25 kV and 0.1 μ A. The micrographs of the FGM sample were taken near the edge region, at depths of approximately 300, 600 and 1000 μ m. Most of the micrographs were taken in back-scattered mode. Phase identification was conducted by recognising the color contrast of the grains. This technique is possible since the atomic numbers of aluminum, titanium, and zirconium are sufficiently different. The size of the grains was computed using the lineal intercept method (Wurtz and Nelson 1972).

The microstructure of the microhardness impressions and cracks was also observed using SEM. Some of the cracks were magnified to elucidate the micromechanism of the deformation in the vicinity of the indent.

CHAPTER 4

SYNTHESIS AND MICROSTRUCTURAL CHARACTERISATION OF A FUNCTIONALLY-GRADED ALUMINIUM TITANATE/ZIRCONIA-ALUMINA COMPOSITE

4.1 INTRODUCTION

The development of functionally-graded ceramic materials by infiltration has been demonstrated by various researchers which include Glass and Green (1987), Marple and Green (1990), Low *et al.* (1993 and 1996a), Pratapa and Low (1996), and Honeyman-Colvin and Lange (1996). Physical properties of the functionally-graded materials (FGMs), such as changes in mass and density, indicate the introduction of new phase(s) due to infiltration (e.g., Glass and Green 1987; Marple and Green 1990).

The profile of FGMs can be tailored to obtain a gradual change in composition, porosity, crystallinity, etc. Most of the materials which have been developed involve composition change (Hirai 1996). This development is popular because most available methods of producing FGMs such as CVD, electro-deposition, sol-gel processing, plasma spraying and slip-casting, may be readily used for this purpose.

A graded composition profile is an important aspect in designing FGMs since it continuously bridges two different properties imparted by two different materials. Two desirable properties can be combined with gradual change in property from one face to another by controlling the phase composition. Therefore, characterising the phase compositional distribution throughout FGMs is an important part of understanding the properties of these materials.

Characterisation of elemental distribution (hence, phase composition) in FGMs is usually conducted using x-ray microanalysis (e.g., Marple and Green 1990; Requena *et al.* 1992; Marple and Boulanger 1994; and Sarkar *et al.* 1993). In this technique, an FGM was cross-sectionally cut and then finely polished (up to 1 μm grade). Characteristic x-ray intensity lines of each element were collected from various sample depths and then converted into phase abundance. The use of x-ray diffractometry was only to observe the presence of phases in the material (Marple and Green 1990; Low *et al.* 1993 and 1996a).

Phase distribution in FGMs can also be determined by using scanning electron microscopy. For example, Sarkar *et al.* (1993) used the back-scattered mode to collect images of an YTZP-Al₂O₃ FGM. Since Zr has much higher atomic number than Al (40 against 13), the ZrO₂ grains appear lighter than Al₂O₃ grains. This technique was used in this study to characterise the nature, size, and distribution of grains. X-ray dot-mapping can also be used to determine the elemental distribution, and hence phase distribution in FGMs (Low *et al.* 1993 and 1996a; Pratapa and Low 1996).

Inclusion of a second phase into a ceramic matrix may affect its microstructure. For instance, inclusion of MgO and ZrO₂ into an alumina matrix may both reduce grain size and inhibit exaggerated grain growth of alumina (Dörre and Hübner 1984). Marple and Green (1990 and 1993) observed a gradual change in both of these characters when a graded composition of mullite was introduced into an alumina matrix.

In this chapter, physical properties of an AT/zirconia-alumina FGM, i.e. changes in mass, bulk density, apparent porosity, shrinkage, and shape of the material are discussed. The mass difference and density were used to calculate the amount of the new phase (AT) introduced into the bulk system.

The graded profile of phase compositions in the FGM was characterised using Rietveld x-ray diffraction analysis. Mass attenuation coefficient corrections were applied using Compton scatter intensities measured by x-ray emission spectrometry. The graded composition of the material was also qualitatively studied using an energy-dispersive microprobe analyser.

4.2 RESULTS

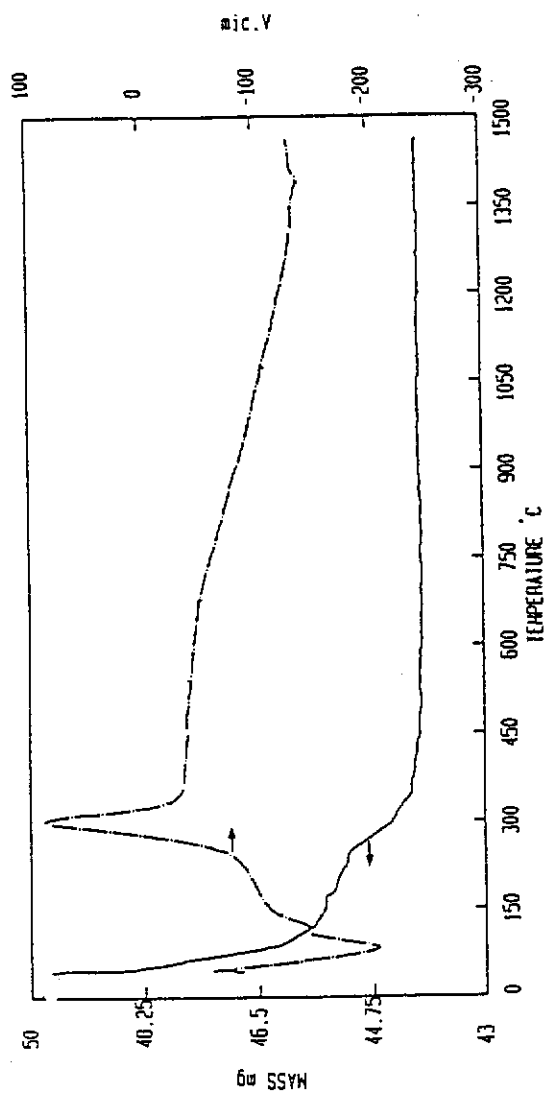
4.2.1 Physical Character

The porosity of the alumina-zirconia preform after pre-sintering was $45 \pm 2\%$. Porosity of as high as this value (Low *et al.* 1996a; Pratapa and Low 1996) was also used for producing mullite/ZTA and mullite-AT/ZTA FGMs via infiltration. The SEM micrograph (backscattered mode) of the alumina-zirconia preform is shown in Figure 4.1. The figure shows that the porosity of the preform is well-distributed in the material.

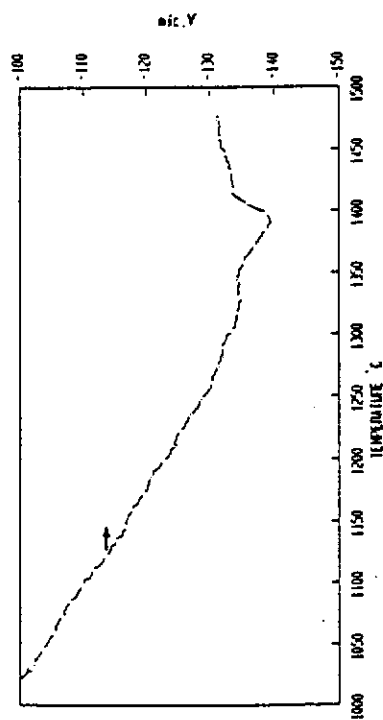
Figure 4.2 shows the DTA results during the firing of the material from room temperature to 1500° C. An endothermic peak appears at about 80° C which can be related to the de-chlorisation of TiCl₄. Another endothermic peak at 120° C



Figure 4.1 SEM back-scattered micrograph of alumina-zirconia preform before infiltration. Note that the porosity (fine black dots) is well-distributed in the material.



(a)



(b)

Figure 4.2 Differential thermal analysis result for the TiCl_4 -infiltrated alumina-zirconia mixture.
(a) between room temperature and 1500°C, (b) between 1000 and 1500°C.

indicates the removal of physically-adsorbed water. The pronounced exothermic peak at 280° C can be related to the combined removal of residual hydroxyl groups and organic materials. The endothermic peak at approximately 1380° C indicates the formation of AT.

Table 4.1 shows the mass change, bulk density, apparent porosity, and shrinkage of the as-fired, both infiltrated and uninfiltrated, zirconia-alumina composites.

Table 4.1 Mass change, density, porosity, and shrinkage of the infiltrated and uninfiltrated (control) specimens.

Specimen	ΔM_a (%)	ΔM_b (%)	ΔM_c (%)	D_i (g.cm ⁻³)	D_f (g.cm ⁻³)	P_i (%)	P_f (%)	S (%)
Infiltrated	23.8(8)	5.4(4)	4.2(6)	2.3(1)	4.07(2)	45(1)	3.3(3)	40.1(25)
Control	-	-0.2(2)	-0.6(5)	2.3(1)	4.06(3)	45(1)	2.1(4)	46.5(14)

ΔM_a = relative mass difference after and before infiltration.

ΔM_b = relative mass difference after drying and before infiltration.

ΔM_c = relative mass difference after sintering and before infiltration.

D and P = density and porosity.

S = volume shrinkage.

Subscripts i and f indicate initial (before infiltration) and final (after sintering), respectively.

Figures in parentheses are the estimated standard deviation of the values to the left.

The preforms gained a certain amount of TiO₂ precursor after the 24 hours infiltration. The “wet” mass gain of the preform was determined by measuring the mass of the preform before and after infiltration. With initial mass of approximately 7.9 g, the preforms gained 0.4 g of TiO₂ precipitate during infiltration. The mass difference between the preform prior to infiltration and the composite body after sintering was also recorded. A mass increase (ΔM_c) of 4.2 ± 0.6 % was achieved. This mass increase is evidence that a new phase had been introduced into the preform and can be related to the formation of AT via the equimolar reaction between alumina and TiO₂ (rutile) during sintering - see Equation (1.2). The formation of AT has been reviewed previously in section 2.3.2.

The mass gain measurement is useful for estimating the amount of AT incorporated into the infiltrated specimen. Marple and Green (1990) also made use

of this approach to determine the amount of mullite incorporated in their alumina preform. Note that this approach can only be used to calculate the bulk amount of AT, not its distribution. The graded distribution of phases will be discussed in section 4.2.2.

There are two approaches for estimating the AT content in the sintered FGM. Firstly, by using the mass of infiltrant present in the preform, and the titanium chloride content of infiltrant which was converted into rutile (“wet” method). The second method uses the mass difference (ΔM_s) between the preform prior to infiltration and the composite after sintering (“dry” method). For the “wet” method, by using the reactions



the mass losses during the reactions can be calculated.

Since the molar masses of titanium chloride and titania are 189.7 and 79.9g, respectively, a mass loss of approximately 58% was achieved during the reaction. Therefore, knowing that the as-received solution contained 30 wt% titanium chloride, and the mass gain after infiltration (ΔM_s) was 23.8%, the preform should contain 7.1% titanium chloride or 3.0% titania. For the “dry” method, the mass gain of titania could be determined directly and a value of $\Delta M_c = 4.2\%$ was obtained. This value is higher than that calculated via the “wet” method. The slight discrepancy may be related to the fact that the latter method calculates the AT content based on the analysed titania content of the infiltrating solution, whereas the former method measures the ‘real’ titania content after sintering.

Assuming that all TiO_2 had reacted completely with alumina in the matrix to form AT [Equation (1.2)] and that 3 wt% tetragonal zirconia was present in the ceramic (as shown by the composition analysis in section 4.2.2), the “dry” mass increase can be related to the *average* content of AT (9.2 wt% or 10.0 vol%) present in the bulk. As described in section 4.2.2, the concentration of AT was not uniform throughout the sample. Instead the content of AT varied from 44.5 wt% on the surface to 5.3 wt% at a depth of 1.5 mm towards the core.

The theoretical density of sintered specimens can be calculated from the “rule of mixtures”. In the green body (hence in the control specimen), the $\text{Al}_2\text{O}_3\text{:ZrO}_2$ volume ratio was 92.92:7.08. The theoretical densities of alumina, AT, monoclinic

zirconia, and tetragonal zirconia (ICDD Powder Diffraction File patterns 10-173, 41-258, 36-420 and 42-1164, respectively) are 3.99, 3.692, 5.80, and 5.86 g.cm⁻³, respectively. Using this information, the theoretical densities of the control and FGM samples were calculated as respectively 4.12 and 4.08 g.cm⁻³. The measured densities of the as-fired control and FGM samples were respectively 4.06 ± 0.03 and 4.07 ± 0.02 g.cm⁻³, which represent 98.5% and 99.7% theoretical densities, assuming that respectively 5 and 3 wt% tetragonal zirconia were present in the ceramics - see phase analysis result in section 4.2.2. This suggests that both the control and FGM samples experienced a similar degree of sintering and had achieved near full densification, as indicated by their low measured porosity values (see Table 4.1).

The mass of the as-fired control sample was slightly lower than the green body. This decrease is due to the removal of organic binder (polyethylene glycol) present which occurs during the initial sintering stage. As expected, the infiltrated specimen increased in mass after infiltration, drying, and sintering.

The apparent porosity of the as-fired specimens was reasonably low, i.e. less than 4%. Table 4.1 shows that the porosity of the infiltrated sample was 3.3% whereas that of the uninfiltrated specimen was 2.1%. These values suggest that densification of both materials is satisfactory. This value is lower than that reported when prehydrolyzed tetraethyl orthotitanate was used, i.e. 4.5% (Pratapa and Low 1996). It appears that the solution containing TiCl₄ is more advantageous in densifying the system by virtue of its lower viscosity and lower organic residue. Moreover, this AT-zirconia-alumina system has a considerable higher final density when compared with similar systems developed by Freudenberg and Mocellin (1987), Persson *et al.* (1981), and Hasselman *et al.* (1993) where at least 12% apparent porosity was observed.

The shrinkage of the specimens was determined by measuring their volume before infiltration (V_i) and after sintering (V_f). The shrinkage S was calculated using Equation (3.3). The volumes of the infiltrated and control specimens were reduced by as much as 40.1% and 46.5% respectively after sintering. The lower shrinkage of the infiltrated sample can be attributed to the presence of AT which expands by 11% during its formation and this hinders sintering and thus reduces the shrinkage of the ceramic.

The bar-shaped samples are shown in Figure 4.3. Samples A, B, and C had been infiltrated and sintered. Sample A was infiltrated for 24 hours without the

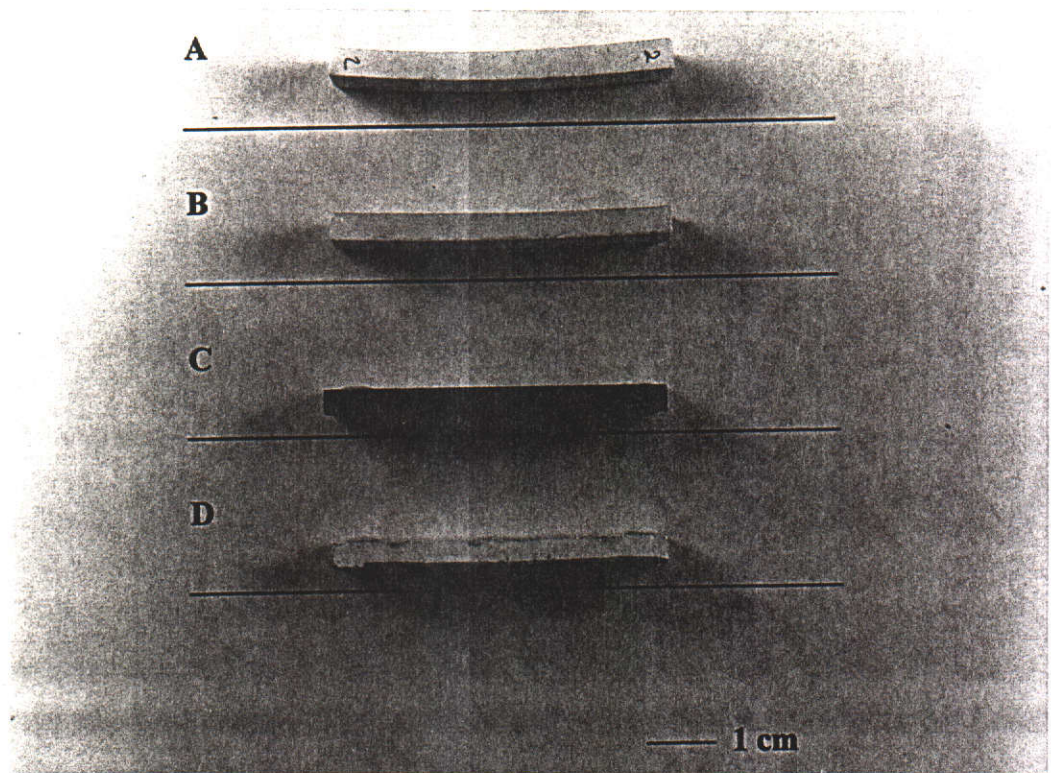


Figure 4.3 Photograph of as-fired infiltrated (A, B, and C) and uninfiltrated (D) specimens. Sample A was not turned over during both infiltration and drying. Sample B was turned over during infiltration but not during drying. Sample C was turned over during both infiltration and drying. Sample C is black-in-colour due to carbon coating.

sample being turned over during infiltration and drying. Sample B was turned over during infiltration, but not during drying. Sample C was turned over both during the infiltration and drying steps. Sample A had bent during final heat treatment. Concavity measurements indicated that sample A had bent as much as 1.5 mm. Sample B was less bent (concavity 1.0 mm) and sample C was straight. The as-fired zirconia-alumina control sample (D) was also straight.

4.2.2 Graded Compositional Character

X-ray Diffraction

Figure 4.4 shows the x-ray diffraction patterns collected from the AT/zirconia-alumina composite at depths of 0.0 to 1.5 mm. Search and match procedures were employed to identify the individual peak in each pattern. The phases present in the material were AT, α -alumina, monoclinic zirconia, and tetragonal zirconia. These phases were observed at all depths. Unassigned peaks were not detected at each depth indicating that the qualitative phase analysis was acceptable.

Figure 4.5 shows x-ray diffraction patterns for the alumina-zirconia control sample and pure α -alumina powder used as an external standard. The control sample contained α -alumina, monoclinic zirconia, and tetragonal zirconia. α -alumina was the only phase observed in the standard specimen. Peaks due to contamination of the diffractometer tube were observed in each pattern and assigned as C.

Figure 4.4 shows that the intensity of AT lines decreased gradually from the surface to the centre of the sample. On the other hand, the intensity of α -alumina peaks increased with depth. These changes in intensity with depth indicate that the sample has a graded composition. The tetragonal (t-) zirconia peak intensity appears to increase slightly with depth. The figure shows no other titania-related peaks which indicates that TiO_2 (rutile) had reacted completely with α -alumina to form AT. It is interesting to note that the t-zirconia peak is lower than that of m-zirconia in this FGM. By contrast, the m-zirconia peak is lower than that of t-zirconia in the control sample.

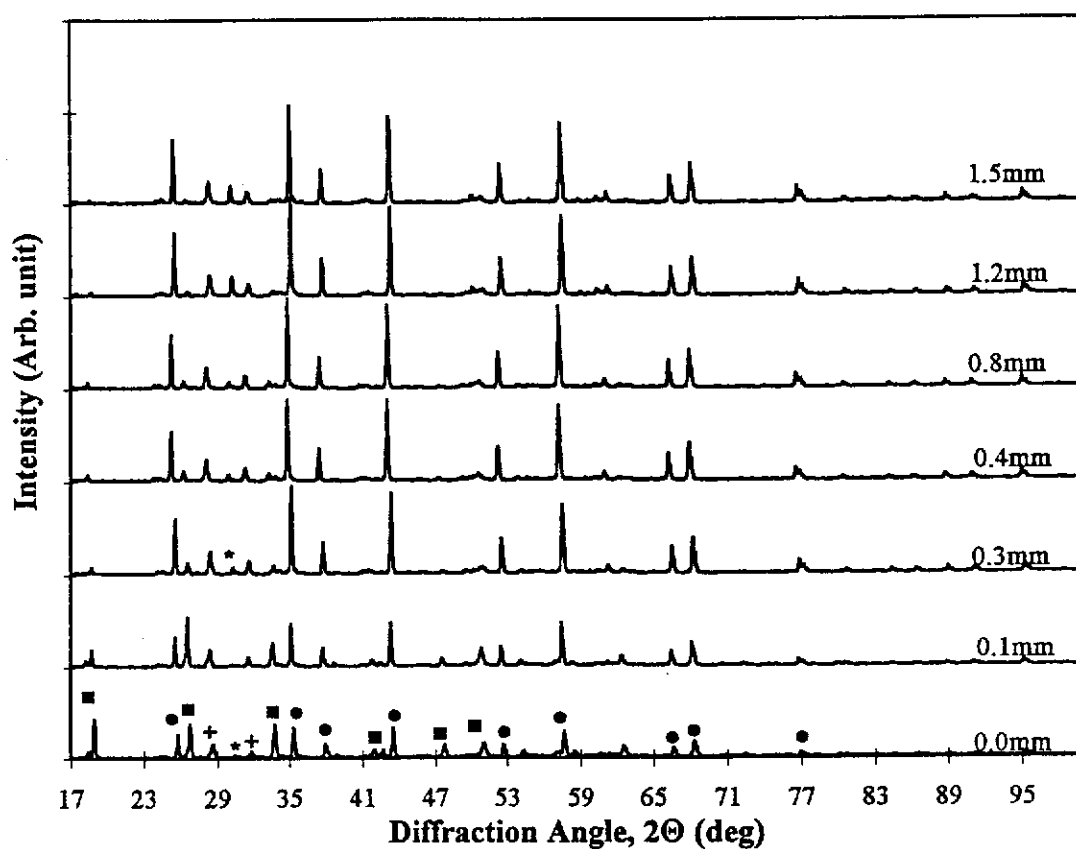


Figure 4.4 X-ray diffraction patterns of AT/zirconia-alumina FGM at various depths. Cu-K α radiation was used. Legend: ■ = aluminium titanate, ● = alumina, + = monoclinic zirconia, and * = tetragonal zirconia.

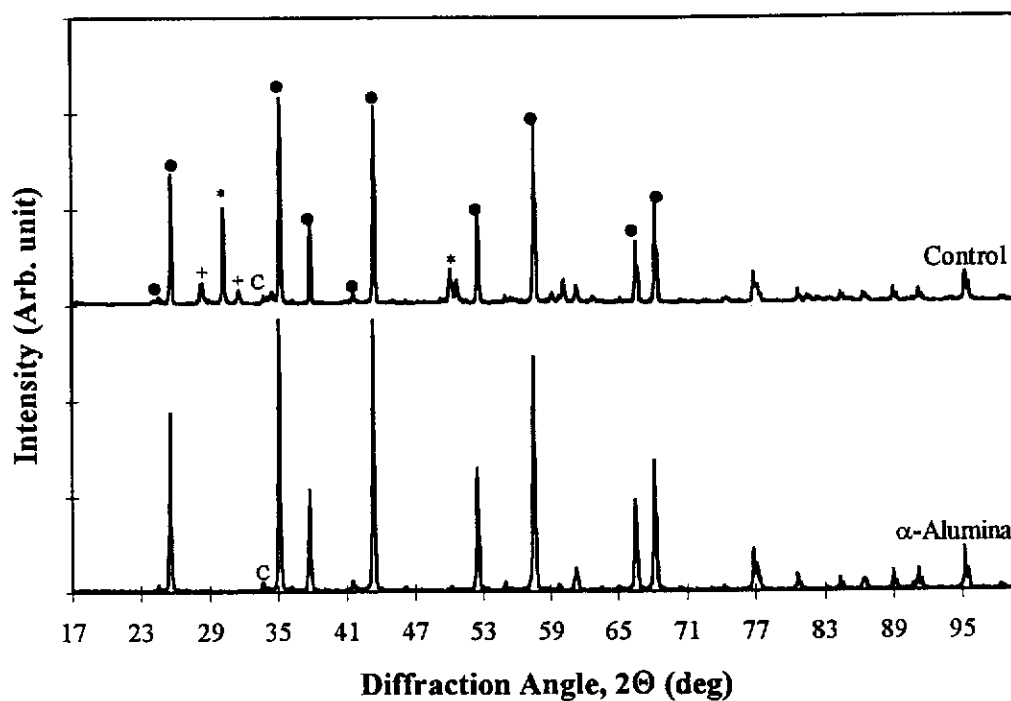


Figure 4.5 X-ray diffraction patterns of zirconia-alumina control sample and high-purity alumina external standard. CuK α radiation was used.

Legend: ● = alumina, + = monoclinic zirconia and * = tetragonal zirconia. C = peaks due to contamination of the diffractometer tube.

Rietveld whole-pattern refinement was then applied to each of the x-ray diffraction patterns. The refined parameters are background profile parameters (B 's) and 2θ -zero shift (2θ) (both are global parameters), scale factors (s), profile broadening parameters (u , v , w), lattice parameters (a , b , c), preferred orientation factor (PO), asymmetry factor (As), and mixing parameter (G). Position coordinates (x , y , z) and thermal parameter (T) were only refined for AT due to the lack of crystallographic data from literature. The output parameters of the refinement of each pattern are shown in Appendix 2 (Table A2.1).

For compositional analysis, the parameters of interest were the scale factor (s) and lattice parameters (a , b , c). Table 4.2 shows the scale factor of each phase at each depth resulting from the refinements. As can be seen from the table, the scale factor of AT decreases with depth. By contrast, the scale factor of α -alumina increases with depth. The scale factor of monoclinic zirconia is lower at the surface than at the centre. For tetragonal zirconia, the scale factor tends to increase with depth. The table also depicts the scale factor of phases in the alumina-zirconia control sample and the external standard α -alumina. The scale factor of t-phase in this control sample is clearly higher than that from the FGM.

The refined lattice parameters (a , b , and c) are as shown in Appendix 2 (Table A2.1). They were used to calculate the unit cell volume of each phase and were then applied to the compositional calculation. The values of the unit cell volumes calculated from the refined lattice parameters are depicted in Table 4.3. The table shows that there is no significant change in these values for all phases in the AT/zirconia-alumina FGM. It should be noted, however, that the estimated standard deviations for unit cell dimensions parameters were 16 times underestimated (Hill and Cranswick 1994). For further analysis, the 'corrected' standard deviations as shown in Table 4.3 were used. The volume of unit cells of phases in the alumina-zirconia ceramic control sample and in the α -alumina external standard are also shown in the table.

There were three measures used to decide the completion of each refinement, i.e. the figure-of-merit, difference plot, and estimated standard deviation. Figures-of-merit from each refinement are presented in Appendix 2 (Table A2.2). Estimated standard deviations are shown in parentheses after each figure in Table A2.1 in Appendix 2. Figure 4.6 shows representative output plots from Rietveld refinement of patterns of the FGM at depths of 0.1 and 1.2 mm. The three measures showed that the refinements were acceptable which enables the use of the

Table 4.2 Scale factors from Rietveld refinement of phases in the functionally-graded aluminium titanate/zirconia-alumina composite at various depths, the alumina-zirconia ceramic control sample, and the α -alumina external standard.

Depth (mm)/ specimen	Scale Factor ($\times 10^6$)			
	α -Al ₂ O ₃	AT	m-ZrO ₂	t-ZrO ₂
0.0	275(4)	180(4)	75(3)	60(10)
0.1	379(5)	152(4)	89(3)	45(8)
0.3	674(5)	52(3)	135(3)	91(7)
0.4	671(5)	46(3)	136(3)	82(5)
0.8	689(5)	40(3)	133(3)	89(6)
1.2	730(5)	44(5)	130(3)	195(6)
1.5	760(5)	31(5)	137(3)	174(6)
Control*	752(5)	-	76(3)	387(8)
Standard	1150(10)	-	-	-

AT : aluminium titanate

m-ZrO₂ : monoclinic zirconia

t-ZrO₂ : tetragonal zirconia

Figures in parentheses indicate the estimated standard deviation at the least-significant figures to the left.

* Scale factor of the external standard = $(1082 \pm 8) \times 10^{-6}$

scale factors and lattice parameters for compositional analysis. The calculation of phase compositions is based on the external standard 'ZMV' method described in Chapter 3 [Equation (3.7)].

Attenuation Corrections

The use of external standard "ZMV" method requires the application of attenuation corrections. In this study, mass attenuation coefficient (MAC) was not determined by calculation, as applied by Gan (1996), but by Compton scatter measurement. The measurement was conducted using x-ray emission spectrometry with a MoK α tube. After determining the Compton peak intensities and investigating the possible peak overlapping, a set of alumina-zirconia compact powders (zirconia weight fraction from 0% to 20%) was prepared. Compton peak intensities of the set were measured and the mass attenuation coefficient (MAC, μ)

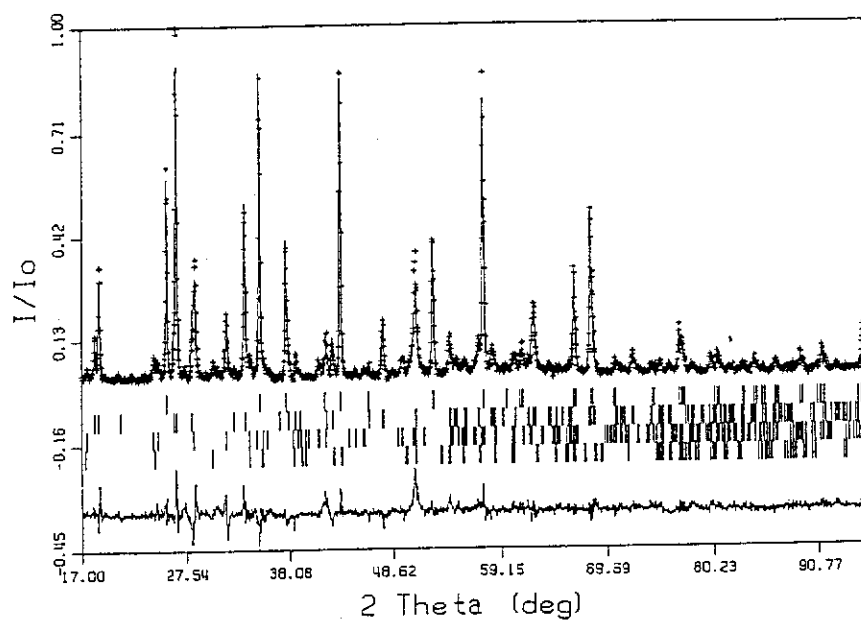
Table 4.3 Calculated unit volume cells of phases in the functionally-graded aluminium titanate/zirconia-alumina composite at various depths, the alumina-zirconia ceramic control sample, and the α -alumina external standard from refined lattice parameters (Appendix 2).

Depth (mm)/ specimen	Unit Cell Volume (10^{-10}) ³ in m ³			
	α -Al ₂ O ₃	AT	m-ZrO ₂	t-ZrO ₂
0.0	255.6(1)	329.4(1)	138.7(1)	65.3(1)
0.1	254.8(1)	327.9(1)	138.2(1)	66.8(1)
0.3	254.8(1)	327.5(1)	137.8(1)	66.9(1)
0.4	253.8(1)	326.6(1)	137.3(1)	66.8(1)
0.8	253.9(1)	326.2(1)	137.5(1)	66.7(1)
1.2	254.9(1)	326.5(1)	137.3(1)	66.9(1)
1.5	254.7(1)	327.1(1)	137.5(1)	66.8(1)
Control	255.3(1)	-	140.1(1)	67.6(1)
Standard	254.9(1)	-	-	-

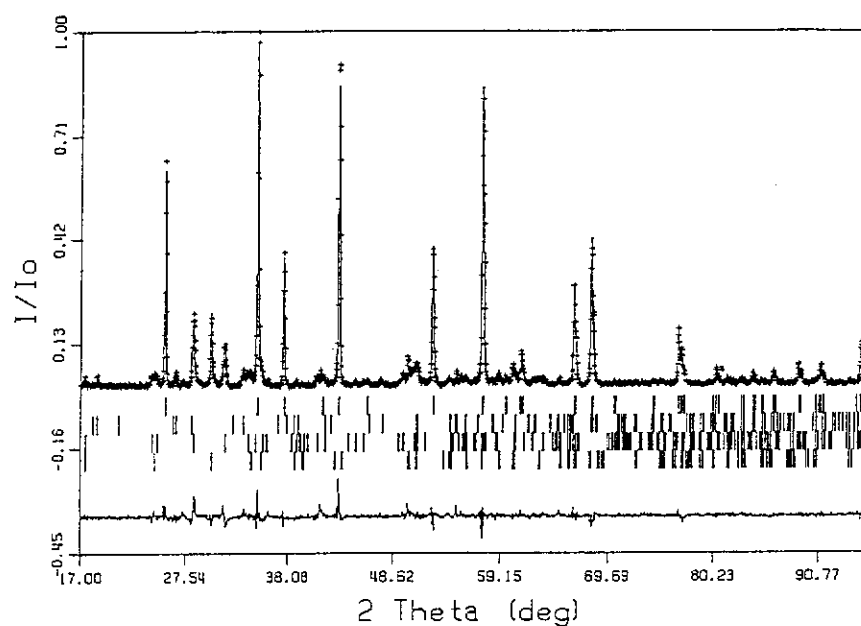
Estimated standard deviations are corrected after Hill and Cranswick (1994).

at MoK α wavelength of each standard was calculated (Toolkit software, O'Connor and Thomas (without year)). The Compton intensity versus I/μ plot resulting from the calculations is shown in Appendix 3, Figure A3.1. A calibration curve (solid line) was extracted from the plot. MAC values at the MoK α wavelength of the specimen at each depth were determined using the calibration curve. After measuring Compton scatter intensity at a certain depth, its MAC value at the MoK α wavelength was estimated from the projection of the point in the calibration curve to the I/μ axis and taking the reciprocal value of this horizontal intercept.

Another calibration curve (Figure A3.2, Appendix 3) was developed to convert the MAC values from those at the MoK α to those at the CuK α wavelength, the wavelength of the radiation used for the x-ray diffractometry. Table 4.4 shows the measured Compton scatter intensities from various depths and the MAC values at the CuK α wavelength. The Compton scatter intensities and MAC values of the alumina-zirconia control sample are also presented in the table.



(a)



(b)

Figure 4.6. Rietveld refinement plot of the specimen at a depth of (a) 0.1 mm and (b) 1.2 mm. The observed data are represented by a (+) sign, and the calculated data by a solid line. Vertical lines represent the positions of diffraction lines of alumina, AT, monoclinic zirconia, and tetragonal zirconia, respectively. The line below the plot is the difference profile.

Table 4.4 Compton scatter intensities and calculated MAC values for CuK α radiation of the functionally-graded aluminium titanate/zirconia-alumina composite at various depths and the alumina-zirconia ceramic control sample.

Depth (mm)/ Specimen	Compton Intensity (counts)	MAC for CuK α (cm ² g ⁻¹)
0.0	7337(83)	56.2(12)
0.1	7804(66)	52.0(10)
0.3	9447(79)	41.6(8)
0.4	9517(103)	41.2(9)
0.8	9517(103)	41.2(9)
1.2	9729(35)	40.2(5)
1.5	9912(39)	39.4(5)
Control	10454(51)	37.5(4)

Table 4.5 Absolute weight fraction of phases in the functionally-graded aluminium titanate/zirconia-alumina composite at various depths and the alumina-zirconia ceramic control sample.

Depth (mm)/ specimen	Weight fraction (%)				
	Al ₂ O ₃	AT	m-ZrO ₂	t-ZrO ₂	Amor.
0.0	44.4(12)	44.5(15)	5.3(3)	1.0(1)	5(2)
0.1	56.4(15)	34.6(12)	5.8(2)	0.7(1)	2(2)
0.3	80.2(19)	9.5(6)	7.0(2)	1.2(1)	2(2)
0.4	78.9(20)	8.3(6)	7.0(2)	1.0(1)	5(2)
0.8	81.0(20)	7.2(6)	6.8(2)	1.1(1)	4(2)
1.2	84.1(16)	7.7(9)	6.5(2)	2.4(1)	0(2)
1.5	85.7(17)	5.3(9)	6.7(2)	2.1(1)	0(2)
Control	90.3(18)	-	4.0(2)	5.0(1)	1(1)

Amor. = amorphous phase.

Phase Composition

The estimated MAC values were then applied using Equation (3.7) to calculate the absolute weight fraction of phases in the AT/zirconia-alumina FGM at all depths. μ is the CuK α MAC value at a certain depth in the sample, whereas μ_s is that of the α -alumina external standard.

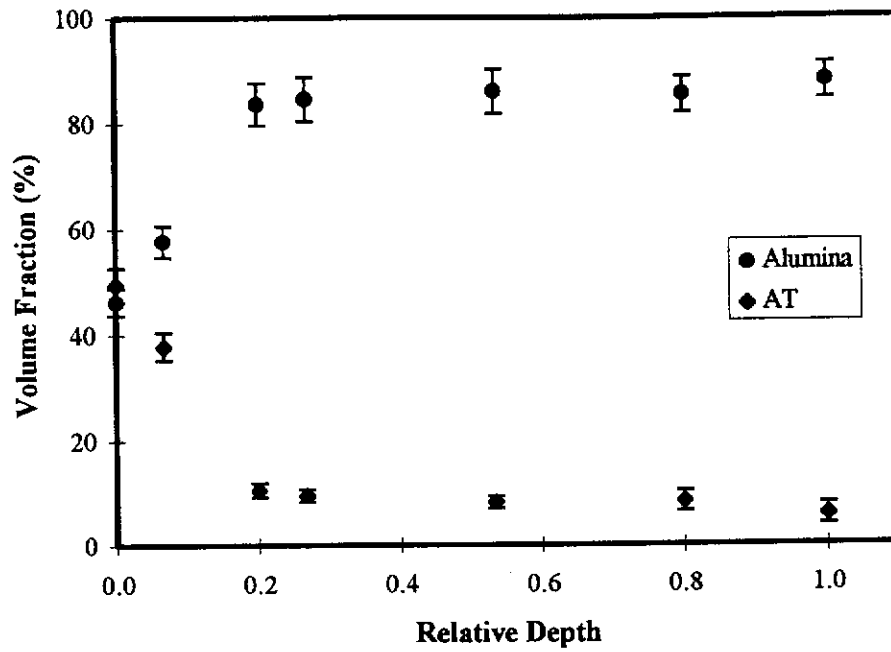
Table 4.5 shows the absolute weight fraction of phases in the FGM at various depths and of the alumina-zirconia control sample. As can be seen from the table, the absolute weight fraction of AT is 44.5 wt% on the surface and reduces with depth to 9.5 wt% at 0.3 mm, and then to 5.3 wt% at 1.5 mm. On the other hand, the alumina content increases with depth from 44.4 wt% at the surface to 80.2 wt% at 0.3 mm, and then to 85.7 wt% at 1.5 mm. It is worth of note that AT was distributed all through the material.

The weight fraction of tetragonal zirconia increased slightly with depth. On the surface of the infiltrated sample the weight fraction of this t-phase was 1.0% and this value achieved 2.4% at a depth of 1.2 mm. The weight fraction of the t-phase in the control sample, however, was higher, i.e. 5 wt%.

The weight fraction of the amorphous phase was determined by subtracting the total amount of the crystalline phases from unity [Equation (3.8)]. The amorphous phase content at each depth is shown in Table 4.5. Approximately 3 wt% (on average) amorphous material was found in the FGM.

The volume fraction of phases in a composite is an important measure to predict the properties of the material. This measure is applied in the “rule of mixtures”. It is, therefore, necessary to calculate the volume fraction of phases in the functionally-graded AT/zirconia-alumina composite. Assuming that the amount of amorphous phase is negligible within the whole sample, the normalised (constrained to 100%) volume fractions are calculated by dividing the absolute weight fractions of phases with the associated density of phases. The results are shown in Figure 4.7. Figure 4.7a clearly shows that the volume fraction of AT decreased linearly with depth whereas that of α -alumina increased complementarily. A marginal increase of t-zirconia content with depth is shown by Figure 4.7b, but the m-zirconia content was reasonably constant. Figure 4.7b also shows the slight increase of total zirconia content with depth. This increase is due to the introduction of TiO₂ during infiltration which produced a graded amount of AT with depth.

(a)



(b)

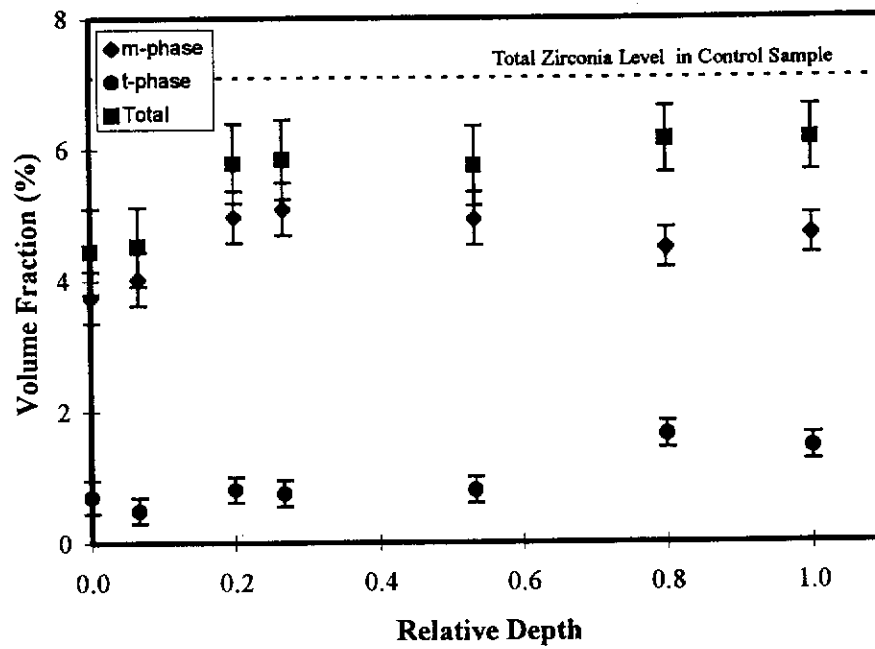


Figure 4.7 Volume fraction of phases in the AT/zirconia-alumina FGM.

(a) Gradual change in volume fraction with depth of AT and α -alumina.

(b) Moderate change in volume fraction with depth of zirconia phases.

Error bars indicate 2x estimated standard deviations.

Energy-dispersive X-ray Microanalysis

Qualitative energy-dispersive x-ray microanalysis was used to verify the graded compositional character. A cross-sectionally cut and finely polished FGM specimen was used for the analysis. X-ray emission intensities of $\text{TiK}\alpha$, $\text{AlK}\alpha$, and $\text{ZrL}\alpha$ were collected from the (near) surface to the centre with both spot size and step size of 50 μm . Figure 4.8 shows the plot of the x-ray emission integrated intensities of the lines versus sample depth. It is clearly shown that titanium emissions gradually reduce with depth whereas those of aluminium and zirconium are fairly constant. This observation suggests that infiltration has led to the formation of an FGM. Similar graded profiles were obtained for the mullite/alumina system by infiltration (Marple and Green 1990). Therefore, these results complement those of x-ray diffraction quantitative phase analysis.

Another qualitative energy-dispersive x-ray microanalysis study was conducted by obtaining a titanium (Ti) dot map of a cross-sectionally cut region of the FGM. Figure 4.9a shows the Ti dot map for the region of approximately 0 - 500 μm within the FGM. The back-scattered SEM micrograph of the associated region is shown by Figure 4.9b. A gradual decrease in Ti (and hence AT) content with depth is clearly evident. This fact, once again, indicates that an FGM with graded composition of AT has been produced.

4.2.3 Microstructure

The microstructure of the infiltrated sample was observed using scanning electron microscopy (SEM). A cross-section of the specimen was polished following a standard ceramographic procedure, i.e. up to a 1 μm finish. Thermal etching at 1500°C for 10 minutes was applied to the specimen to reveal grain definitions.

Micrographs of the infiltrated sample are shown in Figure 4.10. The micrographs were taken at sample depths of approximately 20 μm (near surface), 300 μm , 600 μm , and 1000 μm . All micrographs are in backscattered electron mode. The grain identification was conducted both from the colour of the grains as well as from the elemental x-ray analysis using energy-dispersive spectrometry (EDS) on the grains. The alumina grains exhibit a dark colour and AT grains are slightly lighter (grey-coloured). The small bright grains are zirconia. At 20 μm depth, many grey grains are observed. These grains reduce in number with depth.

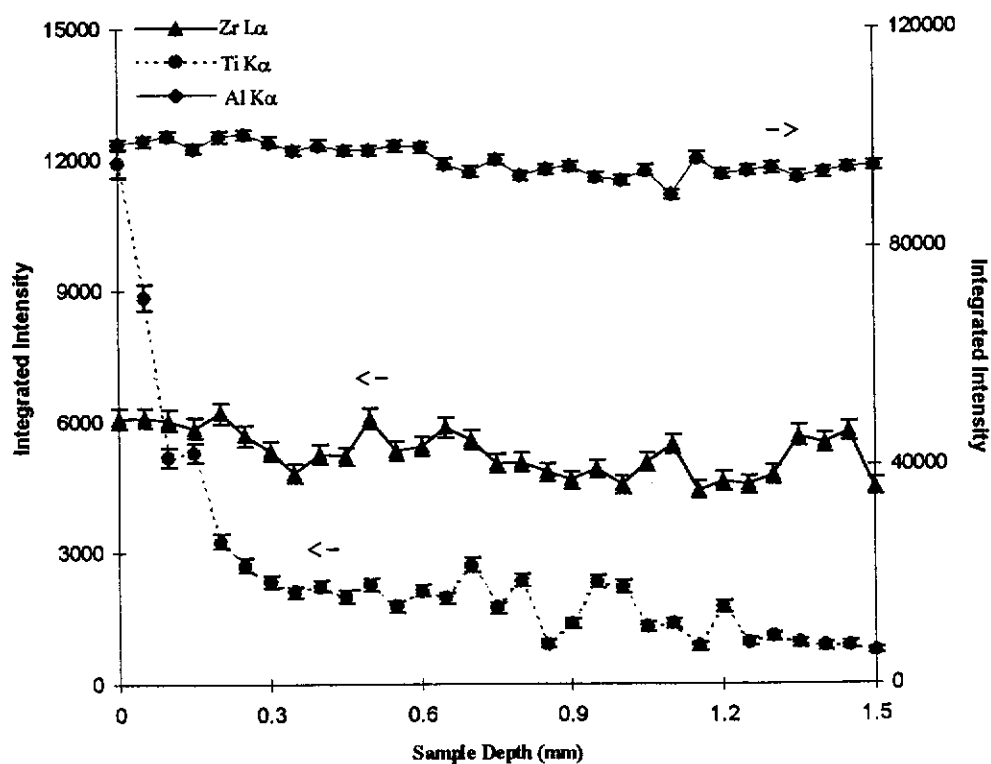


Figure 4.8 X-ray characteristic emissions of TiK α , AlK α , and ZrL α with depth of FGM sample measured using energy-dispersive x-ray microanalysis.

Error bars indicate 2 \times estimated standard deviations.

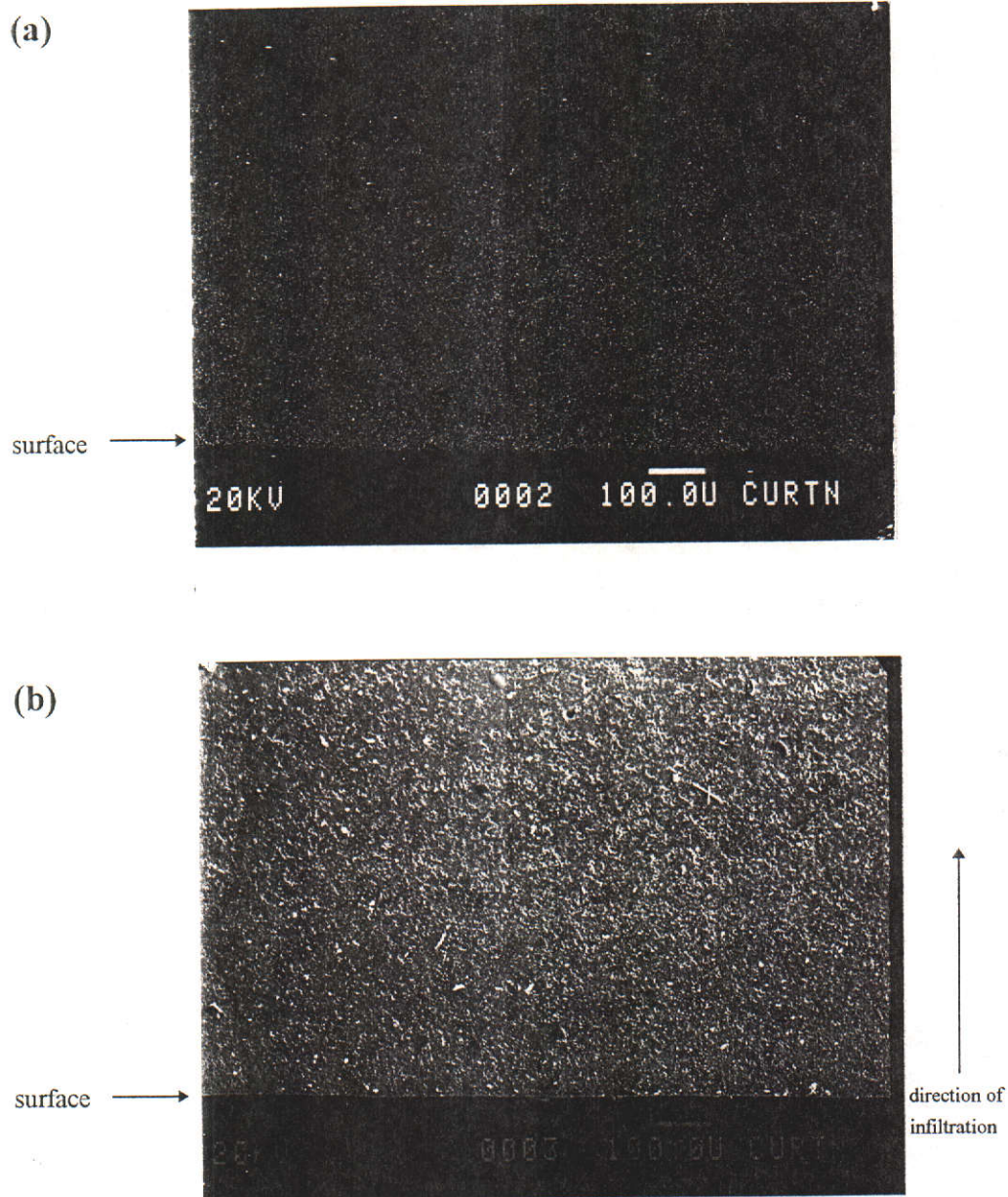
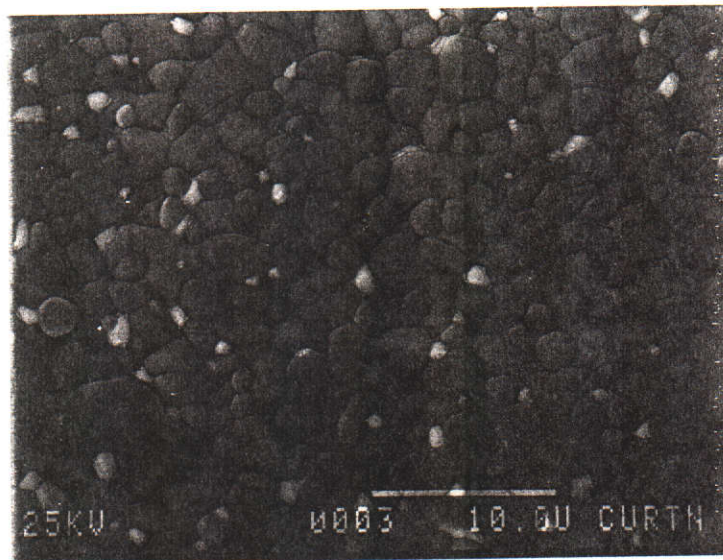


Figure 4.9 (a) Ti dot map at region of approximately 0 - 500 μm within the AT/zirconia-alumina FGM.
(b) back-scattered SEM micrograph of the associated region. Note the same size of the indicator bars.

(a)



(b)

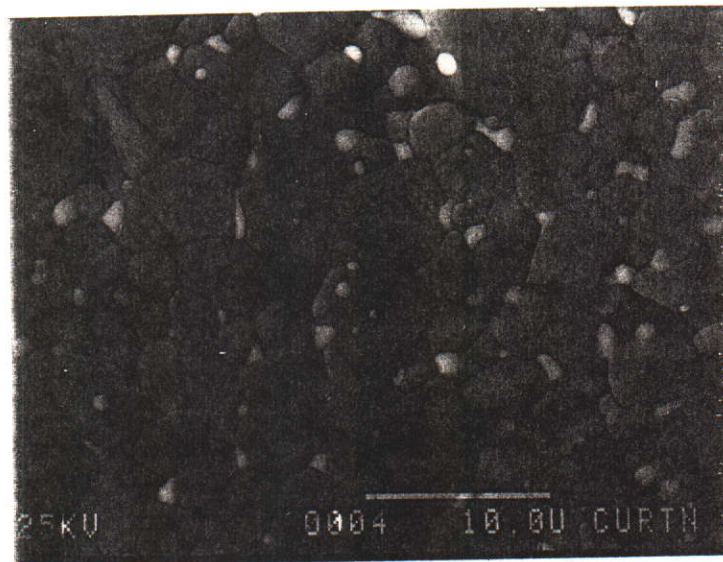
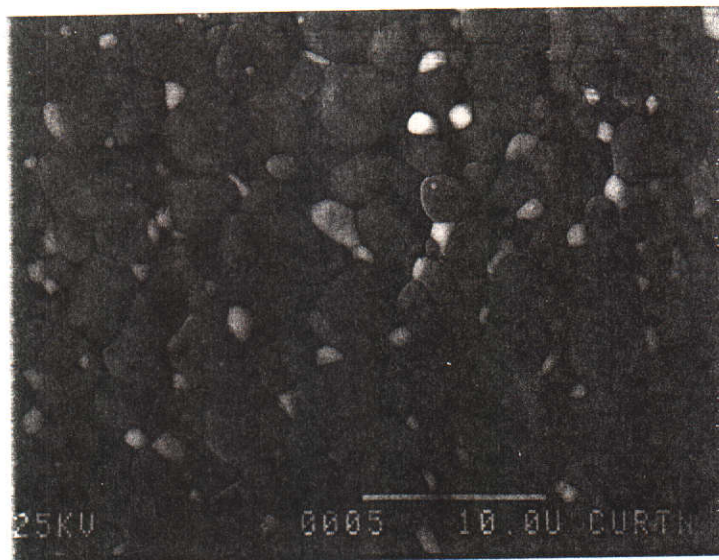


Figure 4.10 Back-scattered SEM micrographs of the as-fired infiltrated specimen at depth of (a) 0.02 mm (near the surface) and (b) 0.3 mm. Dark grains are alumina, grey ones are aluminium titanate, and light ones are zirconia. Sample was polished to 1 μm finish and then thermally-etched at 1500° C for 10 mins. Note the increase in grain size of Al_2O_3 with depth.

(c)



(d)

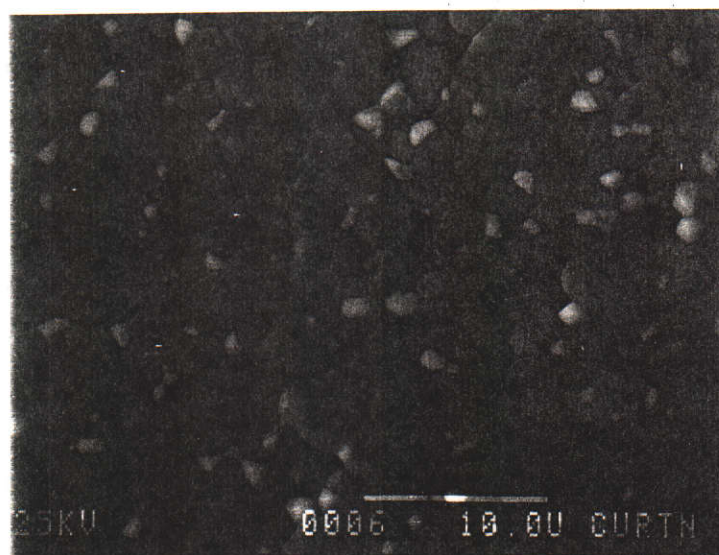


Figure 4.10 (Cont'd) Back-scattered SEM micrographs of the as-fired infiltrated specimen at depths of (c) 0.6 mm and (d) 1.0 mm. Note the increase in grain size of Al_2O_3 with depth.

This indicates that the surface of the as-fired infiltrated specimen is AT rich and that the amount of AT reduces with depth.

Figure 4.10a was taken in the near-surface region (10 - 20 μm). The presence of small-grained ($\cong 2 \mu\text{m}$) alumina is evident particularly at the top of the figure (near the surface). The alumina grains become larger ($\cong 7 \mu\text{m}$) in the inner region (lower part of the micrograph). It appears that the grain growth of alumina is controlled by the presence of AT. In the AT-rich region, small grains of alumina (generally smaller than the AT grains which are $\cong 3 \mu\text{m}$) are located at the multi-grain junctions of AT. Larger alumina grains are observed in the AT-poor region.

Microstructures of the material at depths of 300, 600, and 1000 μm are presented in Figures 4.10b - 4.10d. As can be seen from the micrographs, these regions are less AT-rich than the near-surface. Here, AT grains tend to grow in an elongated manner. Large-grained aluminas (up to 12 μm) are observed at 1000 μm depth. Comparing these figures, it is evident that larger alumina grains are found in the inner region than in the outer.

Zirconia (light coloured) grains are well-distributed in the material. In the near-surface region (Figure 4.10a), most of the zirconia grains are surrounded by AT grains. They are mostly located at triple- or four-grain-junctions. Almost no zirconia grains are located inside AT grains. On the other hand, in the inner region, where alumina grains predominate, many zirconia grains are embedded in alumina grains (for example Figure 4.10b - 4.10d). Triple- and four-grain-junctions as well as grain boundaries are also common locations of zirconia grains in this region.

Figure 4.10a shows a dense microstructure. "Porous" microstructures are found in Figures 4.10b and 4.10c. This observation is in contrast with the density measurement which showed that favourable densification had been achieved.

Table 4.6 depicts the grain size measurement results. The maximum grain size of alumina tends to increase from the surface to the centre. Alumina grains of maximum size 12.5 μm were observed at 1.0 mm depth. This size reduces to 7.9 μm at 0.3 mm and to 7.1 μm in near surface.

The average grain size of alumina also generally increases with depth. Alumina grains with average size of as small as 2.1 μm were observed near the surface. This average value increases up to 3.0 μm at 0.3 mm depth, then to 3.2 μm at 0.6 mm depth, and increases again to 3.7 μm near the core.

Table 4.6 Grain size measurement results for the AT/zirconia-alumina FGM.

Depth (μm)	Average grain size (μm)*			Maximum grain size (μm)*		
	Alumina	AT	Zirconia	Alumina	AT	Zirconia
20	2.1	1.9	1.0	7.1	5.4	1.3
300	3.0	1.8	1.2	7.9	2.5	1.7
600	3.2	1.6	1.2	7.1	2.9	4.7
1000	3.7	1.8	1.0	12.5	3.3	1.7

relative standard deviation 10 - 20%

* estimated standard deviation = $\pm 0.08 \mu\text{m}$.

The maximum grain size of AT decreases with depth but then increases slightly in the near-core region, i.e. $5.4 \mu\text{m}$ near the surface, then $2.9 \mu\text{m}$ at 0.6 mm depth, and finally $3.3 \mu\text{m}$ near the core. A slight change in AT average grain size with depth was observed.

There is no certain trend in both maximum and average grain sizes of zirconia with depth.

Microcracking was observed in the AT/zirconia-alumina FGM. AT intragranular microcracks were observed - see, for example, Figure 4.11. This type of microcracking is quite well-distributed within the near-surface region and occurs usually along the short axis, normal to the long axis (Figures 4.10a and 4.11). It is worth noting that these intragranular microcracks generally occur in AT grains which are larger than $2 \mu\text{m}$. It appears that there is a critical grain size for the microcrack formation. Intergranular or grain-boundary microcracking is occasionally observed.

Figure 4.11 shows that intragranular microcracking also occurs in zirconia grains. In this case, microcracks also occur along the short axis. Note that the microcracked zirconia grains are surrounded by AT grains. Microcracks were not observed in alumina-surrounded zirconia grains. It appears that the microcrack in the zirconia grains is driven by the intragranular microcrack in AT grains.

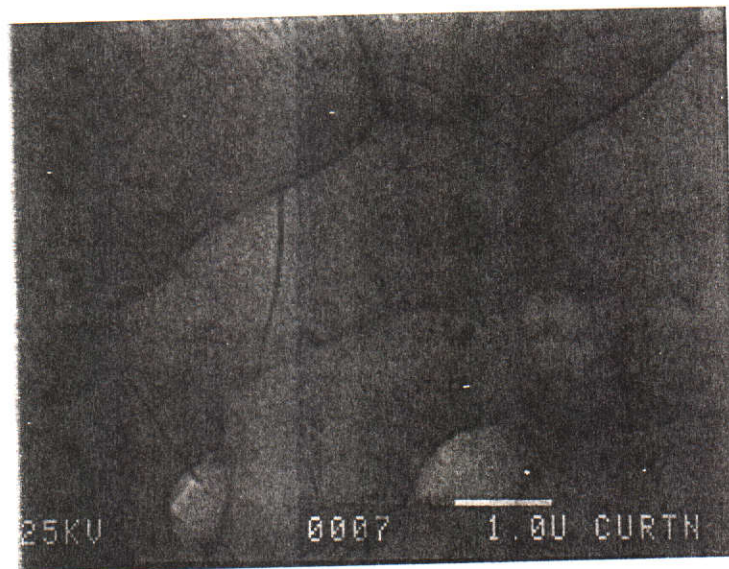


Figure 4.11 Microcracking phenomena in AT and zirconia grains of AT/zirconia-alumina FGM.

4.3 DISCUSSION

Both DTA results and x-ray diffraction patterns collected at room temperature indicate that AT formed in the as-fired alumina-zirconia preform, which had been infiltrated with a solution containing TiCl_4 . An endothermic peak at approximately 1380°C in the DTA curve (Figure 4.2) indicates the formation of AT. Assessing the patterns with the ICDD database, it was found that phases present in the infiltrated specimen were AT, α -alumina, monoclinic zirconia, and tetragonal zirconia, whereas only the latter three phases were present in the uninfiltrated composite.

AT (Al_2TiO_5) in the material has formed via the sintering reaction (Kato *et al.* 1980) between alumina and rutile - see Equation (1.2). Hennicke and Lingenberg (1986) proposed that the formation of AT occurs in two stages. Stage one is phase nucleation which occurs between 1230 and 1280°C . The second stage, grain growth period, starts above 1280°C . The reaction rate was highest between 1300°C and 1400°C . The DTA result for the present study showed that AT formed at approximately 1380°C (Figure 4.2). This result, therefore, agrees with that of Hennicke and Lingenberg (1986) in terms of the reaction rate.

The chemistry of hydrolysis of titanium chloride and its subsequent conversion to amorphous TiO_2 during heat treatment can be described according to reaction Equation (4.1). The amorphous phase was then crystallised at a higher temperature to form anatase. The anatase subsequently transformed into its polymorph TiO_2 (rutile) during the intermediate stage of sintering (Navrotsky and Kleppa 1967; Vasudevan *et al.* 1995). Titania-related phase peaks (such as anatase and rutile) are absent from the pattern. The absence of these peaks indicates that (1) the transformation of anatase to rutile, and (2) the complete reaction between rutile and α -alumina to form AT.

As can be seen from Figure 4.3 the shape of the as-fired infiltrated specimen depends on the processing. It appears that the uniform infiltration throughout the whole green body can be achieved by turning over the specimens during infiltration and drying. Root *et al.* (1991) and Marple and Green (1992) also observed concavity in their disc-shape mullite/alumina specimens. There was no report on the "turning over" of their specimens during infiltration and drying. They proposed that the inner core of the specimens shrank faster than the outer case during cooling resulting in the concavity. In this study, the bending of the AT/zirconia-alumina specimen may be due to the presence of large residual stresses as a result

of thermal expansion mismatch and non-uniform shrinkage during cooling. One side of the sample, which has less AT, shrank faster than the other side. When the specimen was turned over during infiltration, the diffusion of the infiltrant was more uniform. This resulted in a less bent as-fired specimen (sample B). Turning over during infiltration and drying provided a more uniform infiltrant distribution, leading to a more uniform shrinkage rate and a straight sample (C).

The x-ray diffraction patterns show that the phases present in the infiltrated composite are AT, α -alumina, monoclinic zirconia, and tetragonal zirconia. These phases are present at all depths. This indicates that the phases are distributed throughout the whole material. There is an indication of graded composition within the material in regard to the intensities of AT and alumina peaks. A reduction of AT peak intensity with depth suggests that the amount of AT decreases with depth. The concentration calculation shows that this indication is correct, i.e. the absolute weight or volume fraction of AT decreases sharply with sample depth. In contrast, the alumina peak intensities tend to increase with depth and the weight and volume fraction calculations show that the content of alumina increases with depth. Figure 4.7 displays the AT and alumina composition profile versus sample depth. It is clearly evident that the AT/zirconia-alumina composite exhibits a graded profile in compositions of AT and alumina. This suggests that the infiltration route is a useful method to produce functionally-graded materials (FGMs), as also observed by others (Glass and Green 1987; Marple and Green 1989-1993; Low *et al.* 1993, 1996a; Pratapa and Low 1996; and Honeyman-Colvin and Lange 1996). However, the back-pressure from the infiltrant can significantly reduce the infiltration rate with time (Marple and Green 1990) and this is believed to account for the sharp reduction in the content of AT with depth. It follows that removal of this back-pressure during infiltration via pore size control will lead to a FGM with a much gradual change in AT content.

The mathematical models for composition function in FGMs proposed by Wakashima *et al.* (1990), Markworth and Saunders (1995), Hirano (1990), and Hirai (1996) appear to be inappropriate in this AT/zirconia-alumina system. The inability to apply the models can be seen clearly from the abrupt linear decrease and increase in AT and zirconia contents, respectively, from the surface to a depth of 0.3 mm which is then continued by a slow linear change in those contents from 0.3 mm to the core.

The composition function for the AT/zirconia-alumina FGM developed here is based on the nature of the volume fraction “curves” with depth of AT, α -alumina, zirconia (monoclinic + tetragonal); see Figure 4.7. The composition profile is constructed as a function of relative depth (x/d), where x is the sample depth and d is the sample thickness (i.e. 1.5 mm, assuming similar graded profile is found in the other sample face). Two-step linear equations are obtained for each phase:

(A) AT

$$\begin{aligned} V_{AT} &= -194.0 (x/d) + 49.3 & 0 \leq x/d \leq 0.2 \\ &= -5.75 (x/d) + 11.6 & 0.2 \leq x/d \leq 1 \end{aligned} \quad (4.2a)$$

(B) α -alumina

$$\begin{aligned} V_A &= 188.5 (x/d) + 46.0 & 0 \leq x/d \leq 0.2 \\ &= 5.4 (x/d) + 82.6 & 0.2 \leq x/d \leq 1 \end{aligned} \quad (4.2b)$$

(C) Zirconia (monoclinic + tetragonal)

$$\begin{aligned} V_Z &= 6.7 (x/d) + 4.4 & 0 \leq x/d \leq 0.2 \\ &= 0.5 (x/d) + 5.7 & 0.2 \leq x/d \leq 1 \end{aligned} \quad (4.2c)$$

The first two equations express the steep decrease and increase of AT and α -alumina volume fractions, respectively, between the surface and a relative depth of 0.2. Slow change in volume fractions are found for these phases between relative depth of 0.2 and 1. Total volume fraction of zirconia phases also exhibits slight increase with depth, particularly between 0 and 0.2 relative depth. This change is believed to be due to the introduction of new material (rutile) after infiltration, which changed the whole composition of the sintered composite.

It is worth noting that the changes in volume fractions of AT and α -alumina are certainly complementary. This can be seen from the slopes of both curves at the same domain. Between 0 and 0.2 region, the slope of the AT curve is -194.0 which is very close to that of α -alumina, i.e. 188.5, but in opposite direction. At the rest

of the region, the slope values for AT and α -alumina are respectively -5.8 and 5.4, which is, once again, similar but also in opposite direction.

Tetragonal zirconia is present in both FGM and control specimens. In the latter (10:90 by weight), the content of the t-phase is approximately 5 wt% (Table 4.5). In the former, the weight fraction of this phase increases slightly with depth. In the presence of AT, this t-ZrO₂ content appears to reduce considerably. On the surface of the FGM sample, where AT is approximately 45 wt%, the weight fraction of t-phase is 1.0% and this value increases up to 2.4% at a depth of 1.2 mm. Wohlfrohm *et al.* (1991) proposed that weak AT grains were responsible for the inability to retain the tetragonal zirconia phase at room temperature in their AT-mullite-zirconia system. Apart from this explanation, it appears that the presence of AT has induced residual tensile stresses which may be responsible for enhancing the $t \rightarrow m$ phase transformation. As shown by the micrographs, almost no zirconia grains are embedded within alumina grains in the near-surface region. Embedded-within-alumina zirconia grains are commonly found in the inner region. Lee and Hiraga (1994) showed that the embedded zirconia were found preferentially having a tetragonal structure. Therefore, the microstructure observation agrees with the composition calculation, i.e. tetragonal zirconia is more likely to be found in inner regions of the FGM where the AT content is lower than at the surface. Regarding the weakness of AT (Wohlfrohm *et al.* 1991), it can also be argued that, since the amount of AT decreases with depth, the ability to retain t-zirconia is higher in the centre than near the surface of the FGM.

The Rietveld 'external standard' method has allowed the amount of amorphous phase to be computed. This phase is possibly present due to the incomplete crystallisation of the infiltrant precursor. The content of the amorphous phase is low, i.e. less than 5 wt%, suggesting that crystallisation of the precursor is near complete. The value of the amorphous phase MAC (CuK α) at each depth is between 69.8 and 125.8 cm²g⁻¹. This value indicates that the phase is either amorphous TiO₂ [MAC (CuK α) = 127.25 cm²g⁻¹], which experiences incomplete crystallisation to form TiO₂-rutile, or amorphous Al₂TiO₅ (Feltz and Schmidt 1991).

Electron-probe microanalysis was used to qualitatively verify the graded character. Titanium emissions gradually reduce with depth whereas those of aluminium and zirconium are fairly constant. The Ti dot map of the 0 - 500 μ m region also indicated the gradual change in titanium (hence AT) content. These

results suggest that the infiltration has led to the formation of an FGM. Therefore, these results complement the quantitative phase analysis results from x-ray diffraction. A similar graded profile was obtained for a mullite/alumina system by infiltration (Marple and Green 1990).

Micrographs of the specimen taken from several depths show several interesting features. Firstly, the number of AT grains reduces with depth indicating that the amount of AT decreases with depth. This feature shows that the synthesised AT/zirconia-alumina composite exhibits compositional graded character resulting in an AT/zirconia-alumina FGM. Quantitative phase analysis, conducted using x-ray diffractometry, clearly verified the graded composition (section 4.2.2).

Secondly, alumina grain size tends to increase with depth. The grain size of alumina is affected by the amount of AT. It is evident that the presence of AT hinders the grain growth of alumina. It is believed that the addition of AT has suppressed the abnormal grain growth of alumina through a pinning mechanism (Brook 1976; Runyan and Bennison 1991; and Padture *et al.* 1993). The hindrance of abnormal grain growth of alumina was also shown after additions of ZrO_2 (Lange and Hirlinger 1984) and mullite (Marple and Green 1993). Therefore, in the present study, both inclusions (AT and zirconia) led to the hindrance of the alumina grain growth. Graded composition and microstructure have been observed in this composite, as also noted by Marple and Green (1993) for other FGMs (e.g. mullite/alumina) produced by infiltration. They concluded that a mullite content greater than 6 vol% caused the microstructure of alumina to develop in a controlled fashion. Asymmetric, elongated alumina grains were found in regions with less than 6 vol% mullite. These types of grains were not observed in this AT/zirconia-alumina FGM since, when the amount of AT reduces, the zirconia can still control the grain growth of alumina.

The next notable feature in the micrographs is the “porosity” of the AT-poor region. This “porous” structure is believed to be caused by preferential grain pullout of AT during specimen polishing, which has also been observed in an AT-dispersed alumina composite (Runyan and Bennison 1991; Wohlfromm *et al.* 1991; and Hwang *et al.* 1994). They concluded that difficulty in obtaining a good quality polished AT-based ceramic was due to grain pullout during polishing. From this point of view it can be argued here that, in relation to the grain size measurement, the bonding between AT grains and small alumina grains in the near-surface region

is stronger than that between AT grains and large alumina grains in the near-core region. Large thermal expansion mismatch between AT and alumina will serve to reduce further the bonding and thus promote grain pull-out. This phenomenon may offer another explanation to account for the sharp reduction in AT content with depth (see Figure 4.7a) by virtue of its preferential pull-out during polishing.

Another feature is that the location and grain size of zirconia were also affected by the presence of AT. It appears that the grain growth of AT prohibits the coalescence of zirconia grains in the near-surface region resulting in fine intergranular zirconia grains. In AT-poor regions, zirconia grains are located in both intergranular and intragranular positions, as commonly found in alumina-zirconia composites (e.g., Lange and Hirlinger 1984; Lee and Hiraga 1994; and Okada and Sakuma 1996). Coalescence of zirconia grains (Lange and Hirlinger 1984) occurs more readily in alumina-rich regions resulting in larger zirconia grains. Lee and Hiraga (1994) showed that the relatively small sized and spherical shaped zirconia embedded within the alumina grains had a tetragonal structure. Therefore, tetragonal zirconia would preferably be found in the inner region of the material rather than in the near-surface region. This, therefore, agrees with the quantitative phase analysis.

The last interesting feature revealed from the micrographs is that the infiltrated specimen shows microcracking. Brittle polycrystalline materials showing anisotropic thermal expansion behaviour tend to exhibit microcracking during their processing. In such materials, there is a critical grain size for microcracking which is dependent upon the degree of anisotropy in thermal expansion. With very high degree of anisotropy (e.g., Morosin and Lynch 1972) AT displays microcracking with quite low critical grain size, i.e. as small as 1-2 μm (Cleveland and Bradt 1978) or 2.5 μm (Ohya *et al.* 1983). Intragranular microcracks in AT have been observed in this study - see, for example, Figure 4.11. This microcracking occurs commonly along the short axis and normal to the long axis (Figures 4.10a and 4.11). Anisotropic grain growth of AT is responsible for this microcracking. The grains prefer to grow along the long axis rather than the short, causing tensile stress along the long axis, and finally resulting in the break-up of the grains parallel to the short axis.

Intergranular or grain-boundary microcracking has been occasionally observed in the FGM. This type of microcracking has been commonly observed in conventional AT-alumina composites (e.g. Persson *et al.* 1981; Padture *et al.*

1993; Hwang *et al.* 1994). This microcracking is due to the thermal expansion mismatch between alumina and AT and the anisotropic grain growth of AT.

Intragranular microcracking of zirconia was also observed (Figure 4.11). Intragranular cracking of monoclinic zirconia grains was found in an alumina-zirconia (24 vol% zirconia) composite (Lee and Hiraga 1994). They suggested that such a crack lost a large amount of its propagation driving force, caused by the plastic deformation of the m-phase grain. In the case of the AT/zirconia-alumina FGM system, however, it appears that the presence of such microcracks are triggered by the intragranular microcrack in AT grains.

4.4 CONCLUSIONS

A functionally-graded aluminium titanate (AT)/zirconia-alumina composite has been successfully synthesised through infiltration of an alumina-zirconia preform with a solution containing titanium chloride. The mass change in the as-fired infiltrated specimen indicated that an average amount of 9.2 wt% or 10.0 vol% AT was formed within the bulk. The concentration of AT decreased from 44.5 wt% on the surface to 9.5 wt% at 0.3 mm depth and then to 5.3 wt% at 1.5 mm depth. By contrast, the concentration of α -alumina increased complementarily from 44.4 wt% on the surface to 80.2 wt% at 0.3 mm depth and then to 85.7 wt% at 1.5 mm depth.

Several conclusions can be drawn from the phase composition analysis. Firstly, the quantitative graded character of the AT/zirconia-alumina FGM has been established by the compositions of phases present in the material, particularly AT and alumina. This result emphasizes that the infiltration process can be a useful technique to produce ceramic-ceramic FGMs. It was found that the composition function with depth of AT and α -alumina followed a rapid linear change at one fifth of the near-surface region and then proceeded by a slow change at the remainder region. There was a slight linear change in volume fraction of zirconia with depth.

Secondly, x-ray Rietveld refinement, with mass attenuation coefficient correction, can be used effectively to analyse the composition profile of an FGM, with the particular case here being AT/zirconia-alumina FGM. The content of amorphous material in the FGM can be determined by this method which gives superior results over the electron-probe microanalysis technique. Moreover, the

former technique can be used to determine the amount of tetragonal zirconia, which is impractical in the latter technique.

Thirdly, the qualitative energy-dispersive x-ray microanalysis results show good agreement with the graded composition character of the FGM. Finally, the presence of AT appears to reduce the content of tetragonal zirconia near the surface, possibly due to the formation of AT-induced residual stresses in the microstructure.

The microstructural study showed qualitatively that graded AT composition was found in the material. This observation agrees with the evidence based on the phase composition analysis.

Grain growth of alumina was hindered by the presence of AT inclusion. This grain growth control resulted in an AT/alumina-zirconia composite with graded microstructure.

Both intragranular (in AT and zirconia grains) and intergranular microcracks were observed in the material. It is believed that microcracking in the AT grain arises from induced tensile stresses along the direction of its preferred grain growth.

CHAPTER 5

THERMAL AND MECHANICAL PROPERTIES OF A FUNCTIONALLY-GRADED ALUMINIUM TITANATE/ZIRCONIA-ALUMINA COMPOSITE

5.1 INTRODUCTION

There have been extensive studies on the graded composition characters of FGMs (e.g., Marple and Green 1990 and 1993; Sarkar *et al.* 1993; Marple and Boulanger 1994; Tu and Lange 1995; Tuffe and Marple 1995; Honeyman-Colvin and Lange 1996; Ruys *et al.* 1996). However, a little work has been done on characterising the graded thermal and mechanical properties of FGMs. For example, the graded hardness and indentation fracture toughness of an alumina/Y-TZP FGM produced by electrophoretic deposition method were observed by Sarkar *et al.* (1993). Low *et al.* (1996b) showed the presence of graded thermal and mechanical properties in an epoxy-modified/ZrP FGM produced by infiltrating ZrP preform with epoxy resin.

In this chapter, thermal and mechanical properties of the AT/zirconia-alumina FGM produced by infiltration are reported. Results were obtained from experiments following procedures which have been described in Chapter 3, i.e. section 3.4.1 for thermal expansion coefficient, 3.4.2 for thermal decomposition of AT, 3.5.1 for microhardness and indentation fracture toughness, 3.5.2 for Young's modulus, and 3.5.3 for Hertzian contact response. The graded properties of the material are described and discussed. The microstructure, composition, and properties relationships are also discussed.

5.2 RESULTS

5.2.1 Thermal Expansion

The thermal expansion behaviour of materials was observed using a Rigaku thermal measurement apparatus (TMA) calibrated with an alumina standard. A bar-shaped AT/zirconia-alumina FGM and a zirconia-alumina control sample were prepared for the measurement. The zirconia-alumina ceramic was chosen as the control sample to provide a comparison of thermal expansion behaviour with that for the FGM. The graded thermal expansion behaviour of the FGM was studied by measuring the thermal expansion before and after polishing the surface of the material to 0.3 and 0.5 mm depths.

Plots of thermal dilation ($\Delta L/L_0$) with temperature for both FGM and control samples are shown in Figure 5.1. The average thermal expansion coefficient (TEC) value (Table 5.1) of the FGM increases from $5.6 \times 10^{-6} \text{ }^\circ\text{C}^{-1}$ for the unpolished sample to $7.3 \times 10^{-6} \text{ }^\circ\text{C}^{-1}$ after polishing to 0.3 mm depth. A negligible increase of TEC value, i.e. to $7.4 \times 10^{-6} \text{ }^\circ\text{C}^{-1}$, was observed after polishing the FGM to 0.5 mm depth. The change in TEC from the surface to 0.3 mm depth is associated with the removal of the low-thermal expansion AT from the surface of the material. Table 5.1 also shows that the TEC values of the 0.3 and 0.5 mm - polished FGM has approached that of the control sample.

It is interesting to note that the as-fired FGM exhibits an anomalous thermal expansion curve between 750° and 850° C (Figure 5.1). The TEC drops from $5.5 \times 10^{-6} \text{ }^\circ\text{C}^{-1}$ at 750°C to $4.5 \times 10^{-6} \text{ }^\circ\text{C}^{-1}$ at 850°C. To explain the phenomenon responsible for this thermal expansion “kink”, high temperature neutron diffraction measurements were performed.

Neutron diffraction patterns of the FGM at room temperature (RT), 750°C, 850°C, and 1000°C were collected using medium resolution powder diffractometry - MRPD (located at Lucas Height, NSW and operated by Australian Nuclear Science and Technology Organisation - ANSTO) at $\lambda = 1.664 \text{ \AA}$ to explain the anomalous thermal expansion behaviour of the FGM - see section 3.3.2 for experimental details. The results are shown in Figure 5.2. Highlighted patterns are presented to identify any possible pattern changes particularly with the minor phases. As can be seen from the figure, the monoclinic-zirconia peaks (denoted as Z-m) reduce significantly with increasing temperature. This trend is accompanied by an increase of the tetragonal peaks (denoted as Z-t). This type of transformation is followed by a reduction in unit cell volume by 4% (Stevens and Wang 1989). Thus the observation confirmed that the anomalous thermal expansion behaviour of the FGM was due to the $m \rightarrow t$ zirconia transformation.

Another anomalous behaviour in thermal expansion is also observed in the control sample at approximately 1100°C (see Figure 5.1b). The thermal expansion coefficient value drops by approximately $0.2 \times 10^{-6} \text{ }^\circ\text{C}^{-1}$. This decrease is due to the $m \rightarrow t$ zirconia transformation. Such a drop was not observed at 1100° C in the FGM samples since monoclinic zirconia had already been transformed into the tetragonal structure at a lower temperature, i.e. 750° C. The thermal expansion coefficient drop in the FGM is larger than that in the control sample since the

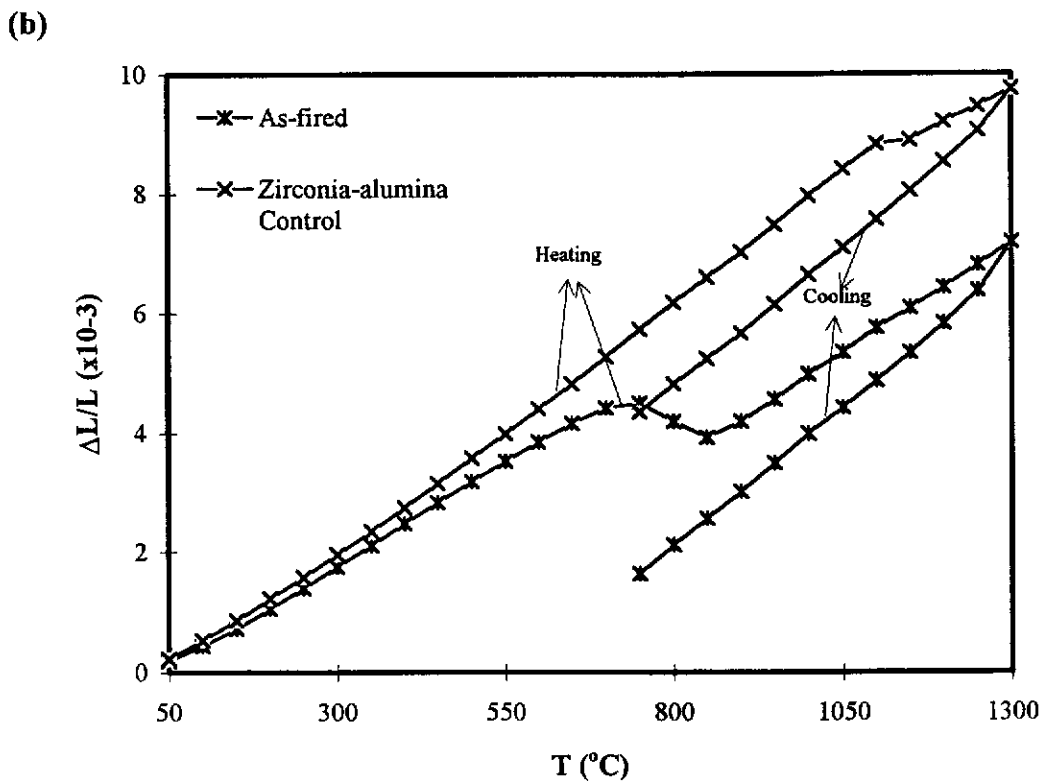
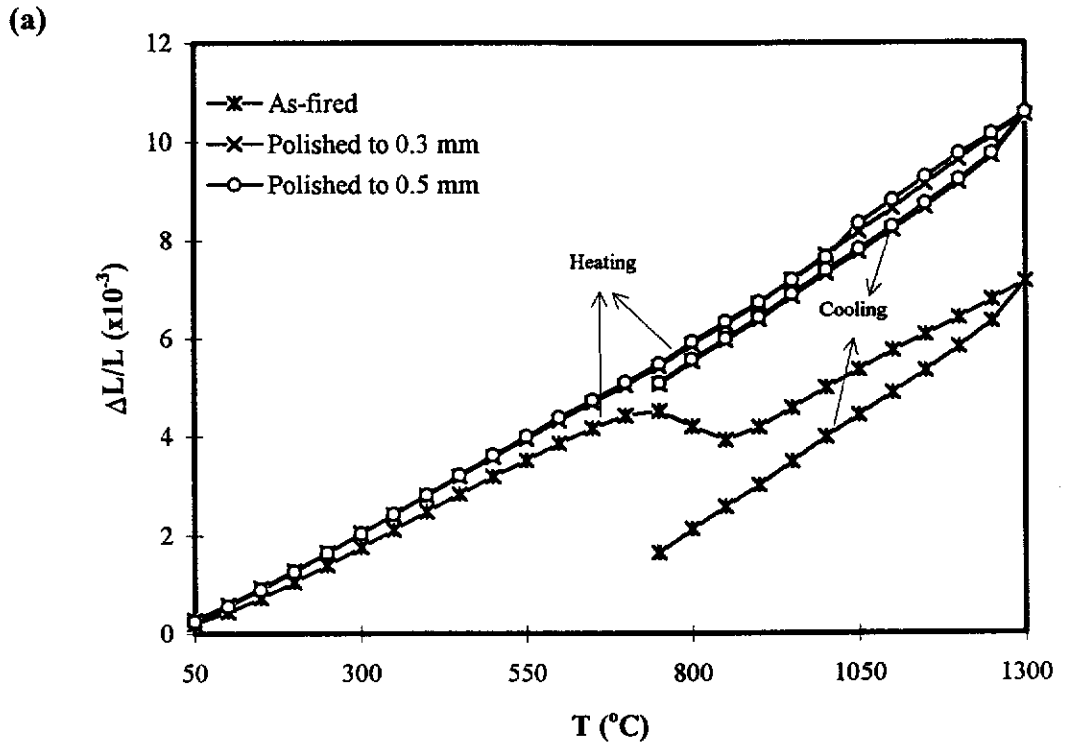


Figure 5.1 Thermal expansion behaviour of AT/zirconia-alumina FGM and zirconia-alumina control sample between 20° and 1300° C; (a) the FGM, as-fired and after polishing up to 0.3 and 0.5 mm depths, (b) the as-fired FGM and zirconia-alumina control samples.

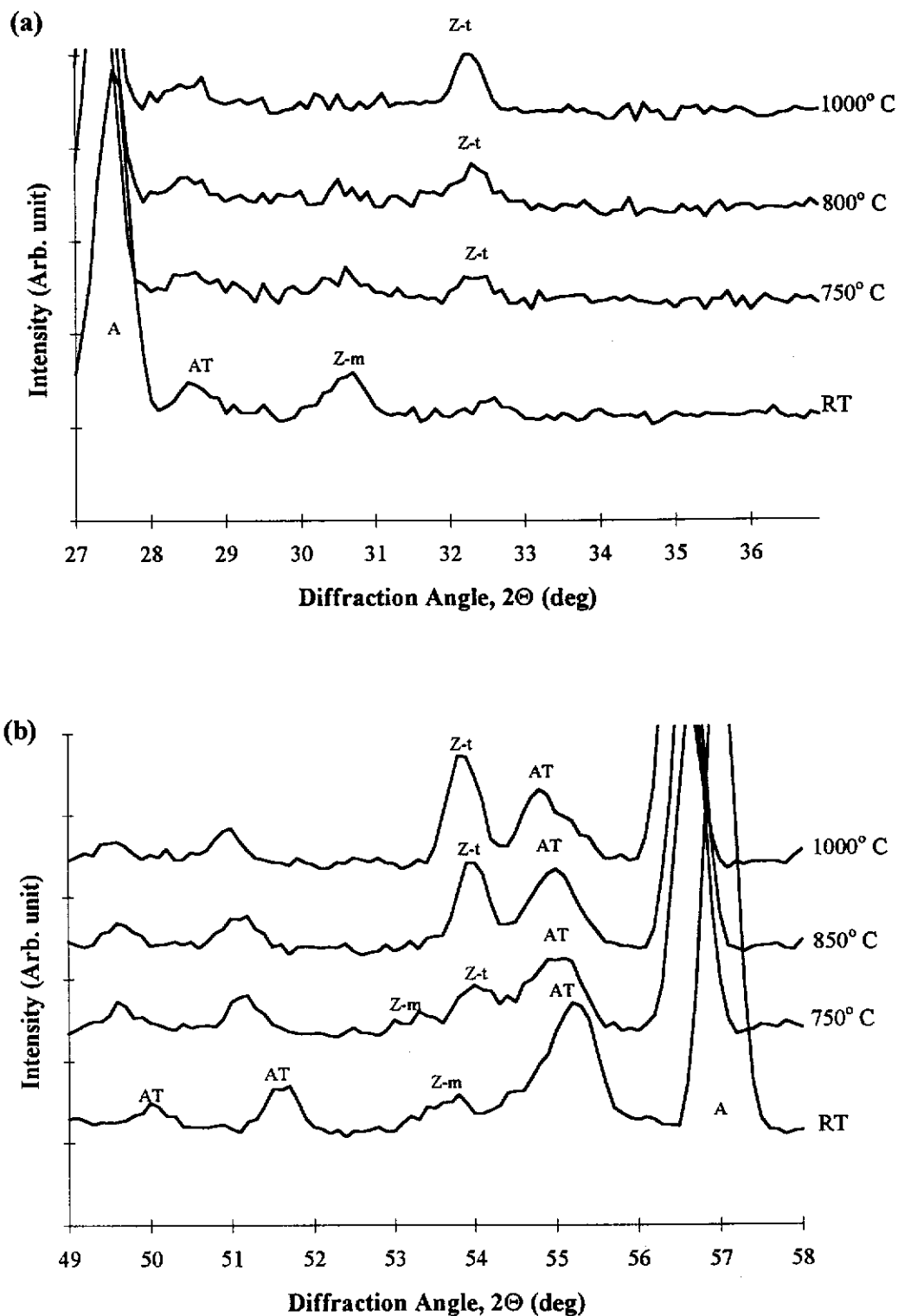


Figure 5.2 Neutron diffraction patterns of the AT/zirconia-alumina FGM collected at room and high temperatures ($\lambda = 1.664 \text{ \AA}$). Patterns are highlighted at 2θ -range of: (a) $27\text{-}37^\circ$ and (b) $49\text{-}59^\circ$. Symbol: AT = aluminium titanate, A = α -alumina, Z-m = monoclinic zirconia, and Z-t = tetragonal zirconia.

Table 5.1 Thermal expansion coefficient value of the AT/zirconia-alumina FGM and alumina-zirconia control sample between 20° and 1300° C.

Specimen		Average expansion coefficient value (10 ⁻⁶ °C ⁻¹)
FGM	Unpolished ⁽¹⁾	5.9
	Unpolished ⁽²⁾	5.0
	Unpolished ⁽³⁾	5.6
	0.3 mm polished	7.3
	0.5 mm polished	7.4
Control Sample (Non-FGM)	-	7.4

(1) between 20° and 750° C.

(2) between 800° and 1300°C.

(3) between 20° and 1300°C.

former has more monoclinic zirconia at room temperature than the latter - see phase analysis results in section 4.2.2. The presence of AT has apparently lowered the transformation temperature of m-ZrO₂ to t-ZrO₂ from 1100° C to 750° C.

5.2.2 Thermal Decomposition of AT

One of the drawbacks of AT is thermal decomposition of the material into its parent phases, i.e. α -alumina and rutile, at between 900° - 1100° C (Kato *et al.* 1980). Extensive studies have been conducted by various workers to understand the mechanism of decomposition and to stabilise the material by incorporating other phases, such as ZrO₂ (Ishitsuka *et al.* 1987), SiO₂ (Ishitsuka *et al.* 1987), MgO (Ishitsuka *et al.* 1987; Battilana *et al.* 1995), and Fe₂O₃ (Battilana *et al.* 1995 and Tilloca 1995). It has been shown by these researchers that MgO and Fe₂O₃ are the most effective material for stabilising the material. ZrO₂ and SiO₂ are less effective in preventing the decomposition.

A decomposition study of AT in the FGM was conducted using x-ray diffractometry to ascertain the extent of AT reduction and rutile formation (Hwang *et al.* 1994). Figure 5.3 shows the x-ray diffraction patterns from the surface of the FGM after annealing at 1050°C for 0, 2, 4, and 6 h. Note that, from the compositional analysis (Chapter 4), the surface of FGM contained 44.5 wt% AT, 44.4 wt% α -alumina, and 6.3 wt% zirconia. It is evident from the figure that AT

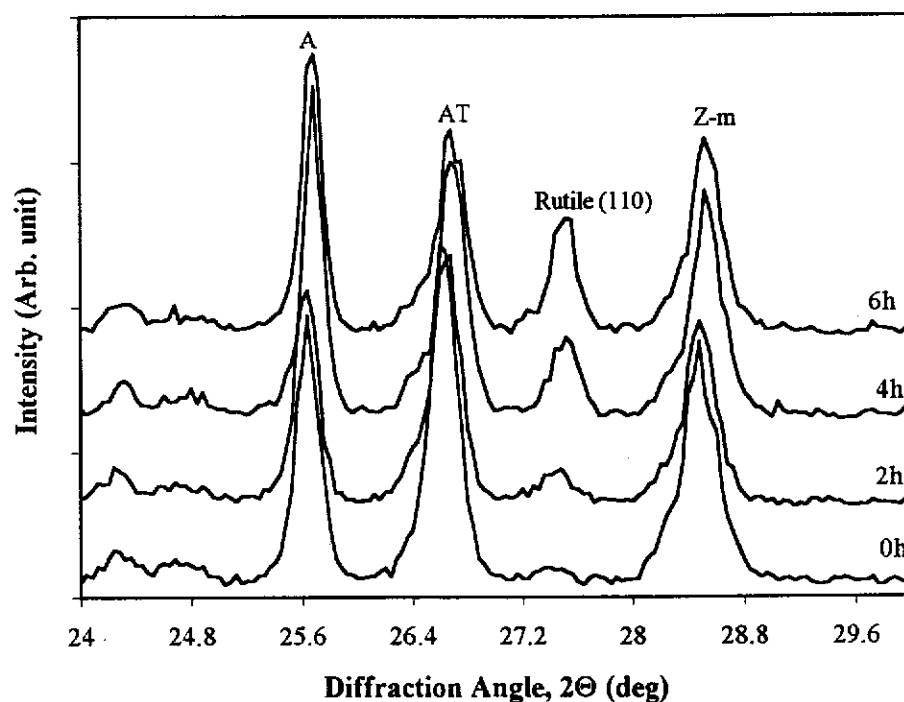


Figure 5.3 X-ray diffraction patterns (CuK α radiation) from the surface of the FGM for decomposition study after annealing at 1050°C for 0, 2, 4, and 6 hours. Note, in particular, the peak increase in rutile (110). Legend: A = α -alumina, AT = aluminium titanate, Z-m = monoclinic zirconia.

on the surface of FGM decomposed into α -alumina and rutile. The evident can be seen, particularly, from the increase of rutile (101) peak with annealing time.

The decomposition rate was determined using integrated intensity ratios of (AT:alumina) and (rutile:alumina). Alumina (024), AT (023), and rutile (110) peaks [Hwang *et al.* (1994)] were selected for the study. Figure 5.4 shows the results of thermal decomposition of FGM at various annealing times. Results from a study by Hwang *et al.* (1994) on the thermal decomposition of AT-dispersed alumina are also presented for comparison. It is clear that, for the FGM, (AT:alumina) peak ratio decreases slowly with annealing time (especially between 0 and 4 h), while the (rutile:alumina) peak ratio increases with annealing time. By contrast, the (AT:alumina) peak ratio for the AT-dispersed alumina sample decreases rapidly, and the (rutile:alumina) peak ratio increases abruptly with annealing time indicating a high degree of thermal decomposition.

These results indicate that the presence of zirconia has apparently affected the decomposition of AT in a positive way. Figure 5.4 shows that the decomposition rate of FGM is clearly much less than that of the AT-dispersed alumina system (Hwang *et al.* 1994). While AT in the latter decomposed rapidly with annealing time, the former was reasonably stable for short-term annealing times (< 6 h). However, it is believed that the thermal stability of FGM will eventually degrade with longer annealing times.

5.2.3 Microhardness

Microhardness measurement as a function of depth for the FGM was performed on the cross-section of the polished surface using a Vickers indenter. Indentations were made at depths of 0.1, 0.3, 0.6, and 1.2 mm. Loads of 10, 20, and 100 N were applied at each depth. An alumina-zirconia ceramic was used as a control sample.

Measurements of microhardness as a function of load were performed both in the FGM and the control sample. Loads from 10 N up to 100 N were used. For the FGM, 0.3 and 1.5 mm depths were chosen for the measurement. For the control, indentations were made at the centre of its cross-section.

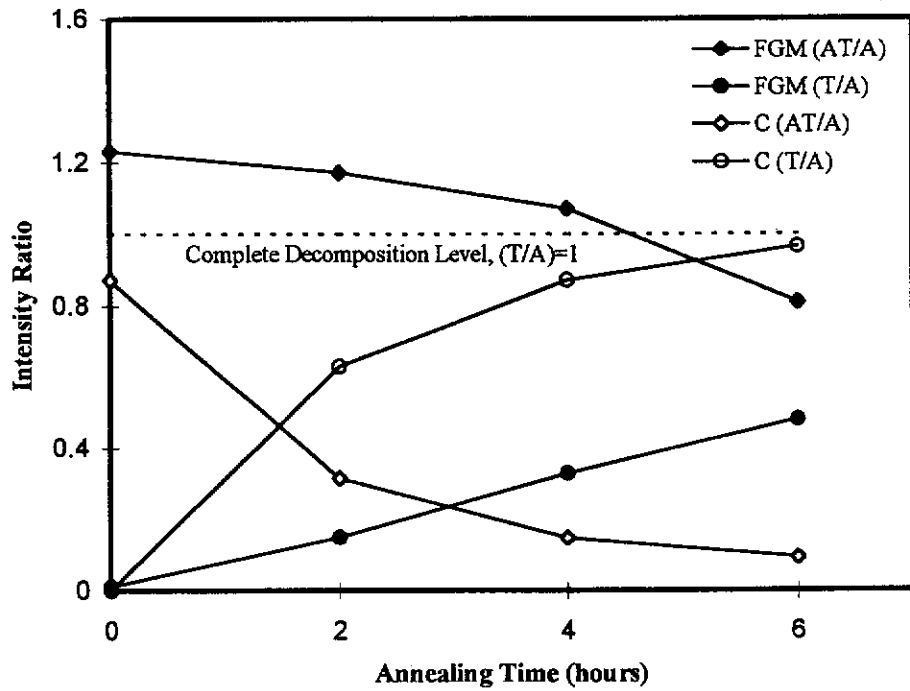


Figure 5.4 Decomposition rate of AT in the AT/zirconia-alumina FGM. Represented ratios are for integrated intensities of [AT(023)/alumina(024)] and [rutile (110)/alumina(024)] lines. Alumina and rutile are denoted as A and T, respectively. Decomposition rate of AT in AT/alumina system [denoted as C, Hwang *et al.* (1994)] is also presented for comparison.

The trend of microhardness with depth in the FGM is shown in Figure 5.5. It is clearly evident that, for all the loads used, the microhardness of the material increases with depth. For instance, at 10 N load, the microhardness is only 5.1 GPa near the surface, then increases to 8.2 GPa at 0.6 mm depth, and finally to 11.8 GPa at the core of the specimen. At 100 N, the value increases from 5.2 GPa at 0.3 mm depth, to 8.5 GPa at 0.6 mm depth and then to 10.2 GPa at the core of the specimen. This increase in microhardness with depth is as expected since the concentration of relatively soft AT decreases with depth as shown by the compositional distribution (Figure 4.7a). The core of the specimen is very much harder than the surface but still softer than the alumina-zirconia control sample, which is approximately 16 GPa. This result indicates that, with inclusion of only approximately 5 wt% AT in the core, the composite has become relatively soft.

Figure 5.5 shows the upper- and lower-bound “rules-of-mixture” hardness curves computed from Equations (2.2) and (2.3). The upper bound is the Voigt-type whereas the lower bound is the Reuss-type. The microhardness curves of the FGM at all depths lie between the bounds. This curve trend indicates that the “modified” rule of mixtures (Markworth *et al.* 1995a) is applicable to the microhardness of the functionally-graded AT/zirconia-alumina composite.

The measurement of microhardness at various loads indicates that the microhardness of FGM drops significantly with load at the near-surface region (0.3 mm) but only a slight drop in the core (1.5 mm). Figure 5.6 shows the plot of microhardness versus indentation load at both positions together with that for the control specimen.

Several aspects can be pointed out from Figure 5.6. Firstly, the FGM is softer than the control sample at all loads. A drop in hardness by a factor of up to 3 is observed at near the surface region of FGM when compared with the control sample, i.e. 16 GPa (control sample) versus 5 GPa (lowest value, near-surface region of FGM). The core of FGM is also softer than the control sample, i.e. 10 GPa (on average).

Secondly, as has been pointed out before, the near-surface region of the FGM is much softer than the core. This can be easily explained by the fact that the amount of soft AT decreases rapidly from the surface to the core.

Thirdly, the FGM displays microhardness values which are strongly load-dependent. A quite large drop in hardness with load is observed near the surface region (0.3 mm), i.e. 9.5 GPa at 10 N, which decreases to 7.9 GPa at 50 N, and

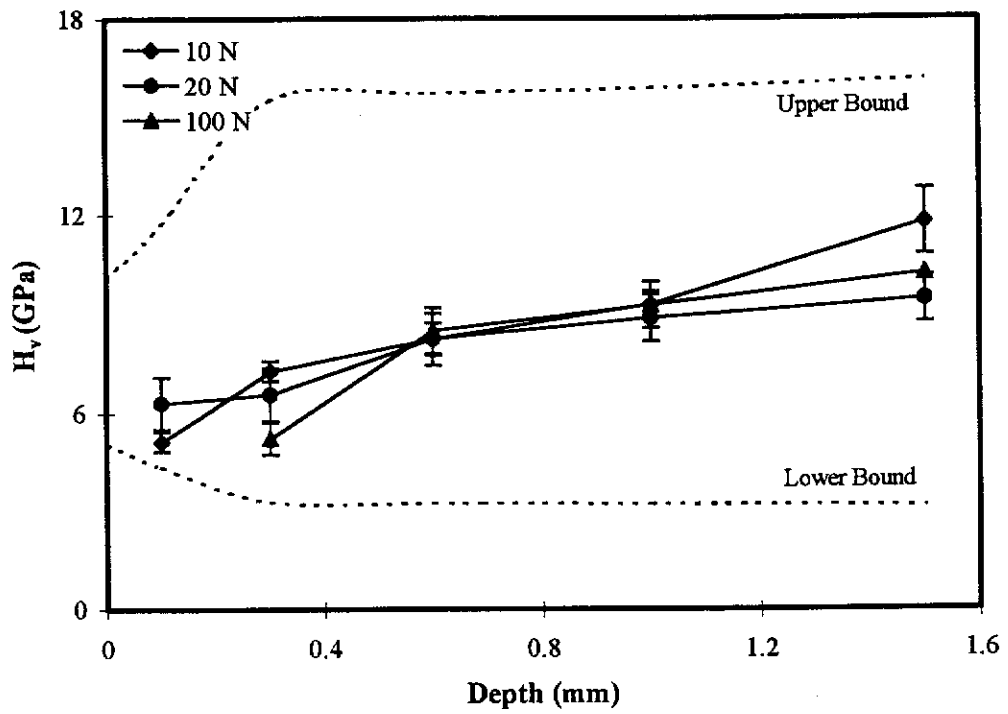


Figure 5.5 Variation of Vicker's microhardness with depth of AT/zirconia-alumina FGM for several indentation loads. Upper and lower bound curves were developed from Voigt-type and Reuss-type "rules-of-mixtures", respectively [Equations (2.2) and (2.3)]. Error bars indicate $2\times$ estimated standard deviations.

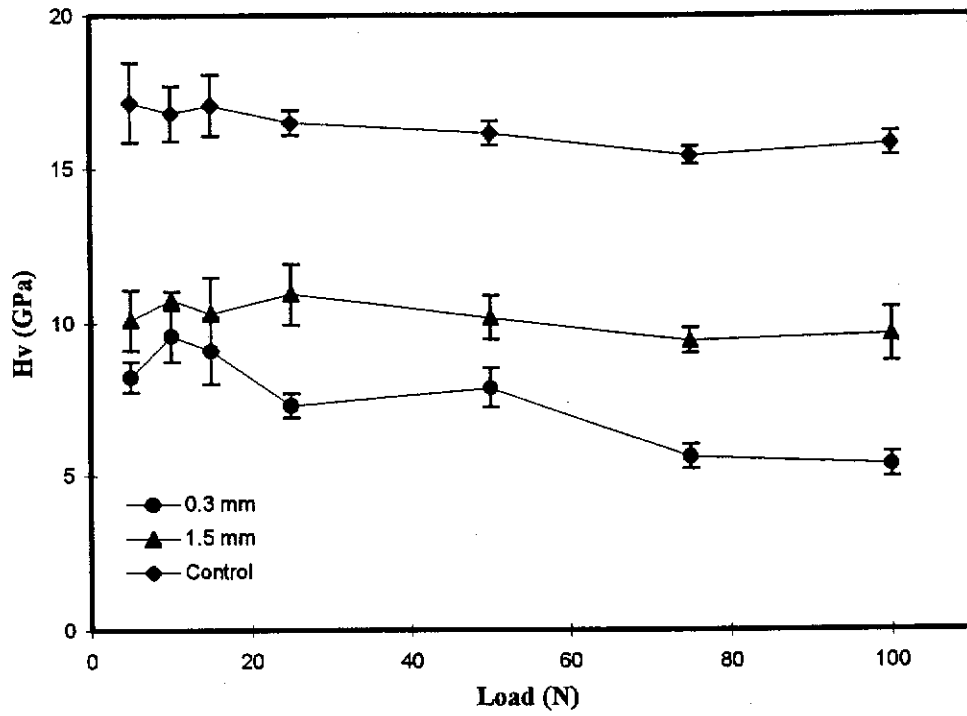


Figure 5.6 Microhardness as a function of indentation load in the near-surface region and the core of the AT/zirconia-alumina FGM. Plot for the control specimen is also presented. Error bars indicate 2× estimated standard deviations.

then drops significantly to 5.5 GPa at 100 N. Only a slight drop in hardness with load is observed at the core of FGM and in the control sample. The decrease in microhardness with load was also observed in the Ti_3SiC_2 ceramic (Goto and Hirai 1987; Pampuch *et al.* 1993). Their observations showed that this behaviour could be correlated to the “quasi-ductile” character of the material. Therefore, it is believed that the near-surface region of AT/zirconia-alumina FGM is soft and “ductile”.

5.2.4 Fracture Toughness

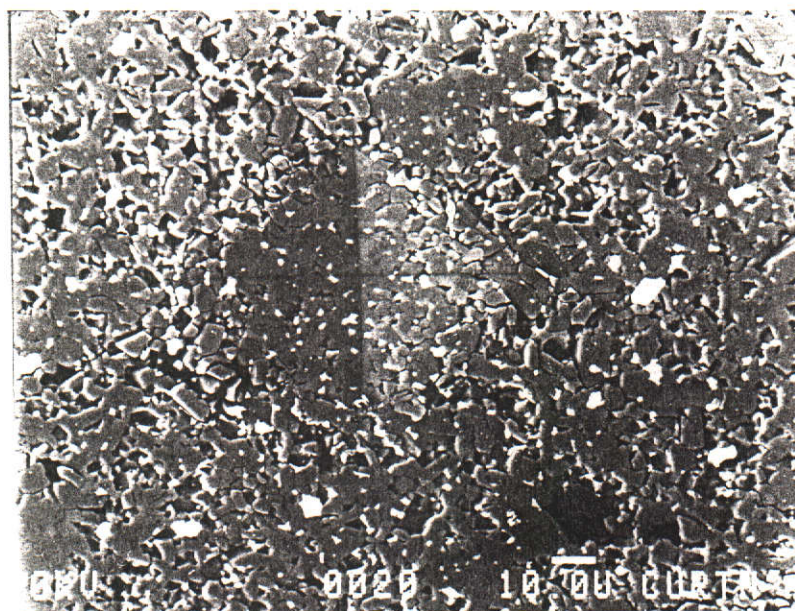
Fracture toughness was determined from Vickers microhardness and crack length measurements. However, unlike “pure” brittle materials which exhibit crack propagation at all four indentation corners, the AT/zirconia-alumina FGM exhibited either no cracks, microcracks distributed within the indentation impression, or short cracks in one or two corners of the indentation.

Figures 5.7 and 5.8 show the representative scanning electron micrographs of the indentation at various depths and loads. All micrographs show that cracks are hardly found at the corners of the impressions. On the other hand, the alumina-zirconia control sample exhibited characteristic long cracks at all indentation corners (Figure 5.9). In view of this, it is difficult to quantitatively determine the fracture toughness of the FGM using Vicker’s indentation.

The indentation micrographs, however, can be used to qualitatively explain the toughness of the FGM. The absence of cracks, for example, indicates that the material is tough. Figure 5.10a shows an indentation corner which exhibits no crack (see arrow). The indentation tip ends in a large grain, but no crack is generated.

Grain pullout due to indentation was commonly observed around the indentation impressions. Figure 5.10b shows a representative SEM micrograph showing a grain prior to pullout (labelled as “G”) and “porosity” due to grain pullout (labelled as “P”). Prior to pullout grains are lifted up from their original position during indentation, whereas the “porosity” (P) was formed from the polishing of sample. It appears that most of the indentation energy is used for debonding the grains and lifting them from the surface rather than for crack formation or propagation. This process of crack energy dissipation is believed to impart considerable fracture resistance to the material.

(a)



(b)

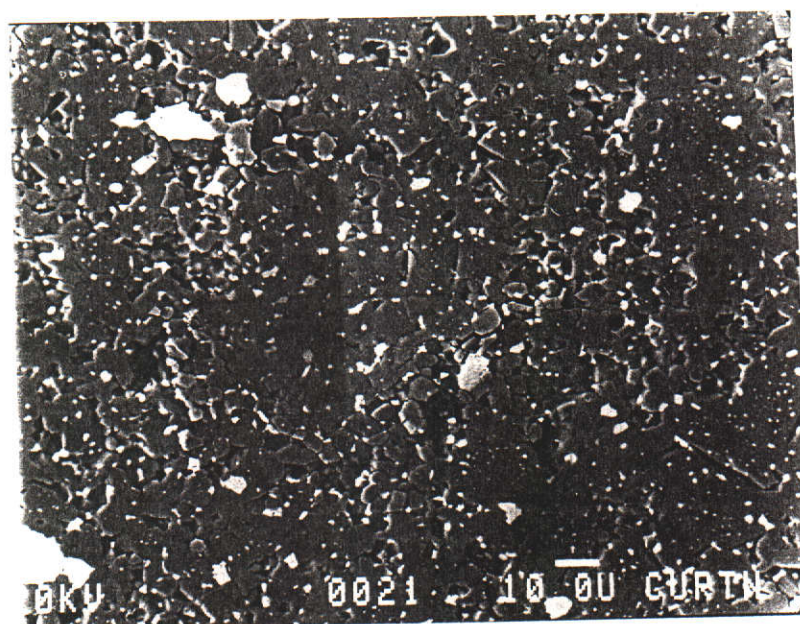
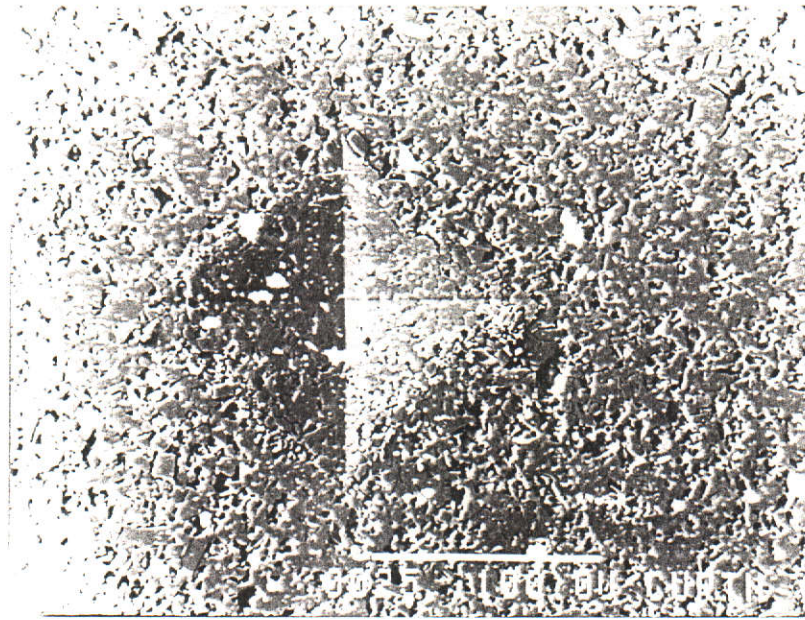


Figure 5.7 Back-scattered SEM micrographs of microhardness indentation of near the surface (0.3 mm) of AT/zirconia-alumina FGM at (a) 25 N and (b) 75 N loads. Associated Vickers hardness (on average) are (a) 8.2 GPa and (b) 5.9 GPa.

(a)



(b)

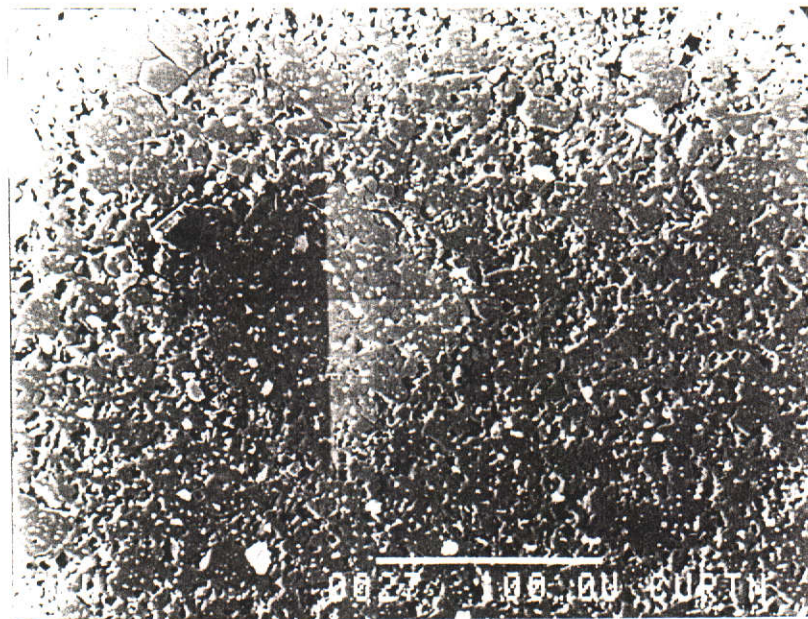


Figure 5.8 Back-scattered SEM micrographs of microhardness indentation of (near) the core (1.2 mm) of AT/zirconia-alumina FGM at (a) 25 N and (b) 75 N loads. Associated Vickers hardness (on average) are (a) 10.3 GPa and (b) 9.1 GPa.

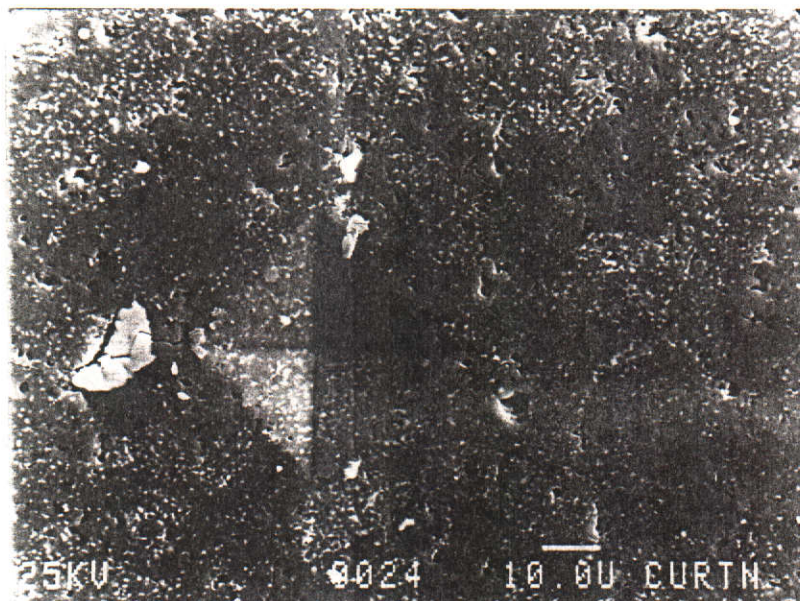
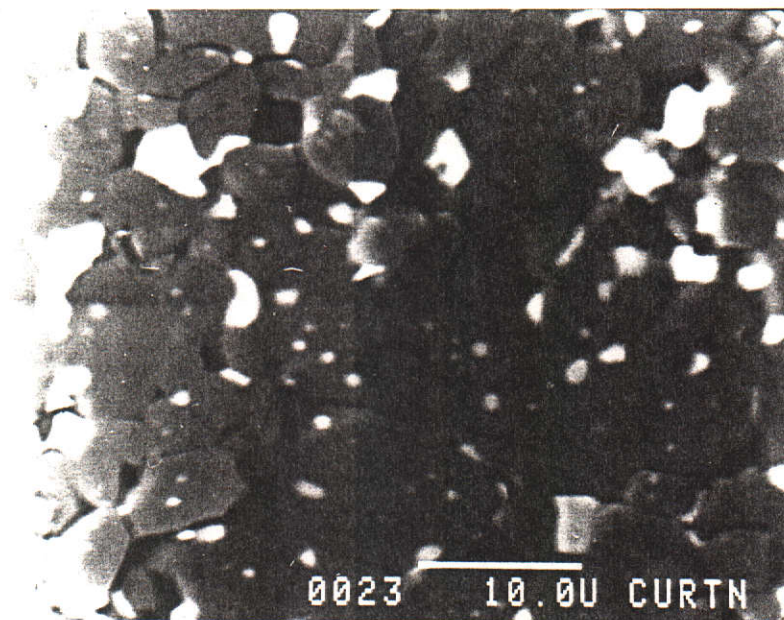


Figure 5.9 A back-scattered SEM micrograph of a microhardness indentation of zirconia-alumina control sample at 15 N load. Associated Vickers hardness (on average) is 15.4 GPa. Note the presence of cracks at all of the indentation tips.

(a)



(b)

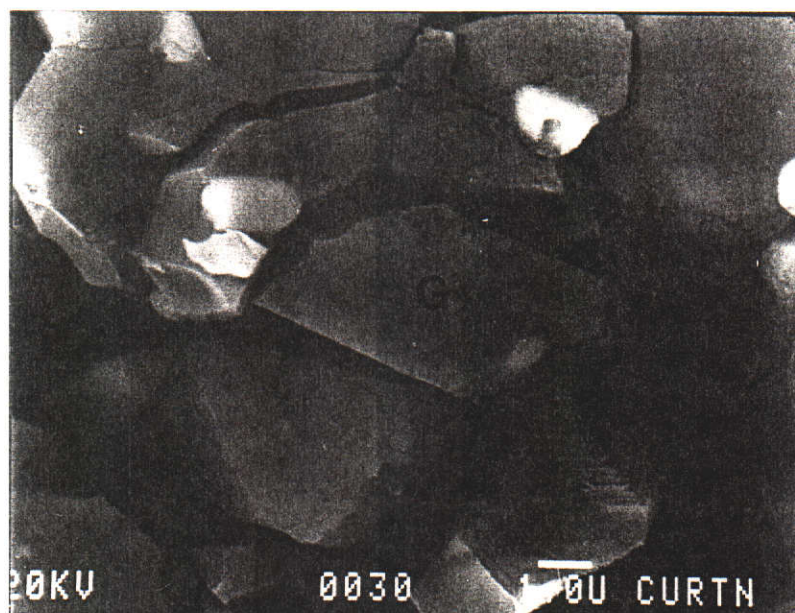


Figure 5.10 Back-scattered SEM micrographs of microhardness indentation of AT/zirconia-alumina FGM showing (a) no-crack indentation tip (see arrow) and (b) grain pullout; P = pulled-out grains and G = a grain prior to pullout.

As previously described indentation cracks were infrequently formed in the FGM. If formed, crack deflections and grain bridgings were prominent. Figure 5.11 shows SEM micrographs of crack deflection and grain-bridging which occur in the vicinity of indentation impressions. These processes can be associated with the flaw-tolerant property of the FGM (Braun *et al.* 1992).

5.2.5 Young's Modulus

The Young's modulus of both FGM and control sample was determined by a flexural resonance vibration method. To observe the effect of graded composition on the variation of Young's modulus in the FGM, measurements were conducted in the as-fired and as-polished sample.

The Young's modulus of the FGM increases slightly with polishing depth (Table 5.2). For the control sample (97:3 of alumina:zirconia by volume), value of as high as 387 GPa was obtained. This is consistent with the value of 380 GPa obtained by Wang and Stevens (1989) for their 90:10 (by volume) alumina:zirconia composites.

Table 5.2 Young's modulus of the AT/zirconia-alumina FGM (as-fired and as-polished) and the control sample.

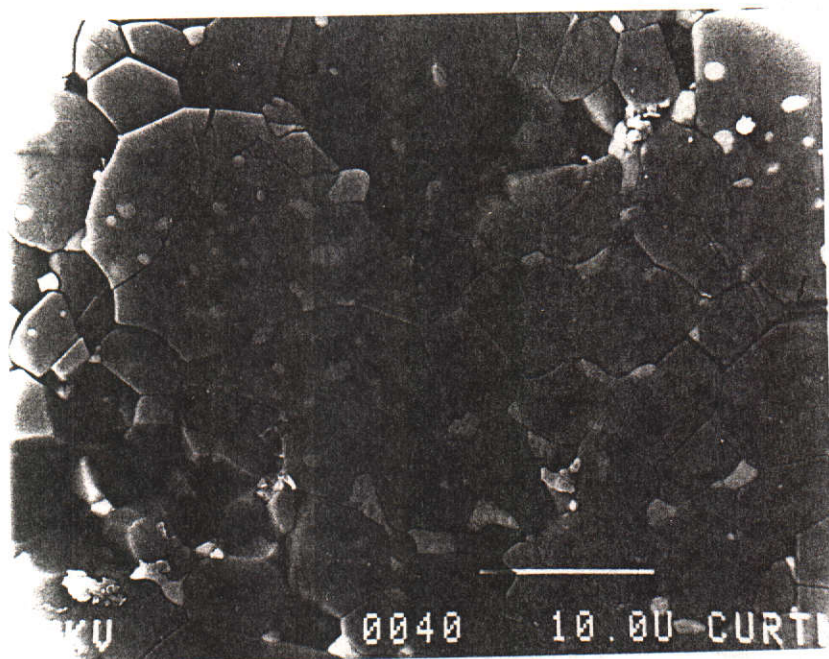
Specimen	Depth of polish (mm)	Young's Modulus (GPa)
FGM	0	280(10)
	0.3	334(10)
	0.5	358(10)
Control	-	386(5)

The FGM has a lower Young's modulus than the control sample which could be due to the presence of AT. It is apparent that the Young's modulus value in the FGM increases significantly with depth of polish, i.e. from 280 GPa before polishing to 334 GPa after 0.3 mm polishing and then to 358 GPa after 0.5 mm polishing. The latter value has almost approached that of the alumina-zirconia control sample which is also the matrix of the FGM.

5.2.6 Hertzian Contact Damage

Hertzian contact testing is a useful method for characterising the sub-surface quasi-plastic damage mechanism particularly in tough ceramic materials. This test

(a)



(b)

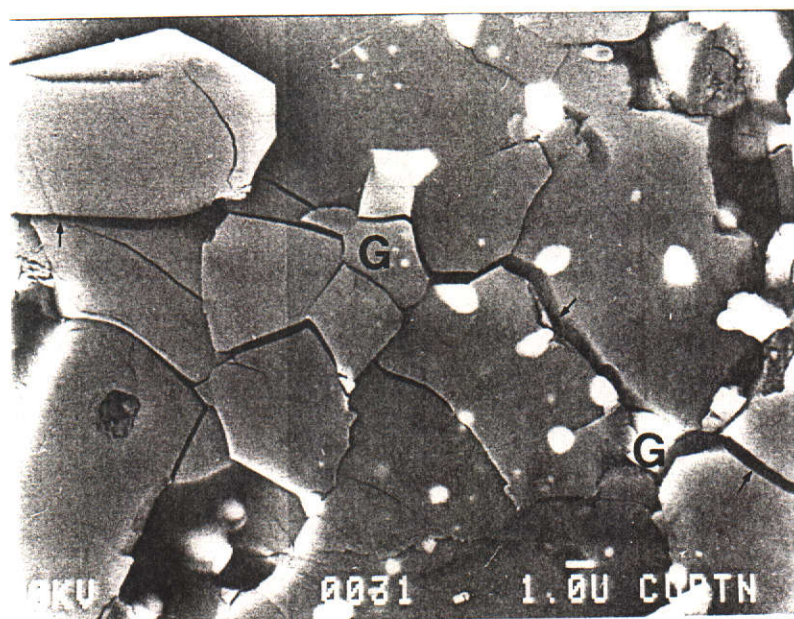


Figure 5.11 Back-scattered SEM micrographs of microhardness indentations of AT/zirconia-alumina FGM showing (a) crack deflection and (b) grain-bridging (labelled as "G"). Cracks propagate from the left-hand side to right-hand side. Arrows indicate the indentation cracks.

utilises a spherical indenter to introduce a controllable damage. The damage characterisation was observed under a Nomarski optical microscope. An indentation stress-strain curve can be measured to quantify the damage tolerance.

In this study, an AT/zirconia-alumina FGM and an alumina-zirconia control sample were prepared for the test. The measurement has been described in section 3.5.3. Figures 5.12 and 5.13 show the effect of the loading on surface and subsurface contact damage in both materials. In the alumina-zirconia control sample, a ring crack has initiated and attempted to run around the contact circle (Figure 5.13a). A classical cone crack was observed in the subsurface region of this material (Figure 5.13b) indicating that the alumina-zirconia control sample is brittle. Note that there is no detectable deformation in both regions. By contrast, instead of displaying a ring crack around the contact circle and cone crack in the subsurface region, the AT/zirconia-alumina FGM shows a deformation which involves microfailures along the weak boundaries between alumina (and zirconia) grains and AT grains (Figure 5.12). This result indicates that the FGM exhibits “quasi-ductility”. It appears that the indentation energy has been used to initiate the microfailures and has caused extensive grain debonding and grain pullout in the contact region.

Figure 5.14 shows the indentation stress-strain curve obtained from the Hertzian indentation measurement. The lower curve represents the indentation stress-strain behaviour of the AT/zirconia-alumina FGM whereas the upper one is that of the control sample. Dashed lines in both curves represent the average Young’s moduli of the specimens. Solid curves are empirical fits for the data.

The FGM exhibits a considerable deviation from the linear curve at a relatively low stress level, i.e. 0.5 GPa, which is reasonably lower than that of the zirconia-alumina ceramic, i.e. approximately 2 GPa. This result, therefore, emphasises that the FGM exhibits considerable “plasticity” during Hertzian loading as was also observed in metals or other ‘quasi-plastic’ ceramic materials (Liu *et al.* 1996; Pajares *et al.* 1996).

5.2.7 Machinability

The machinability of samples was studied by observing the cutting time taken to cut a sample using a diamond cutting blade. Both FGM and alumina-zirconia control samples with thickness of approximately 3 mm were studied. It was found that the time taken to cut the FGM was much less than that for the control sample,

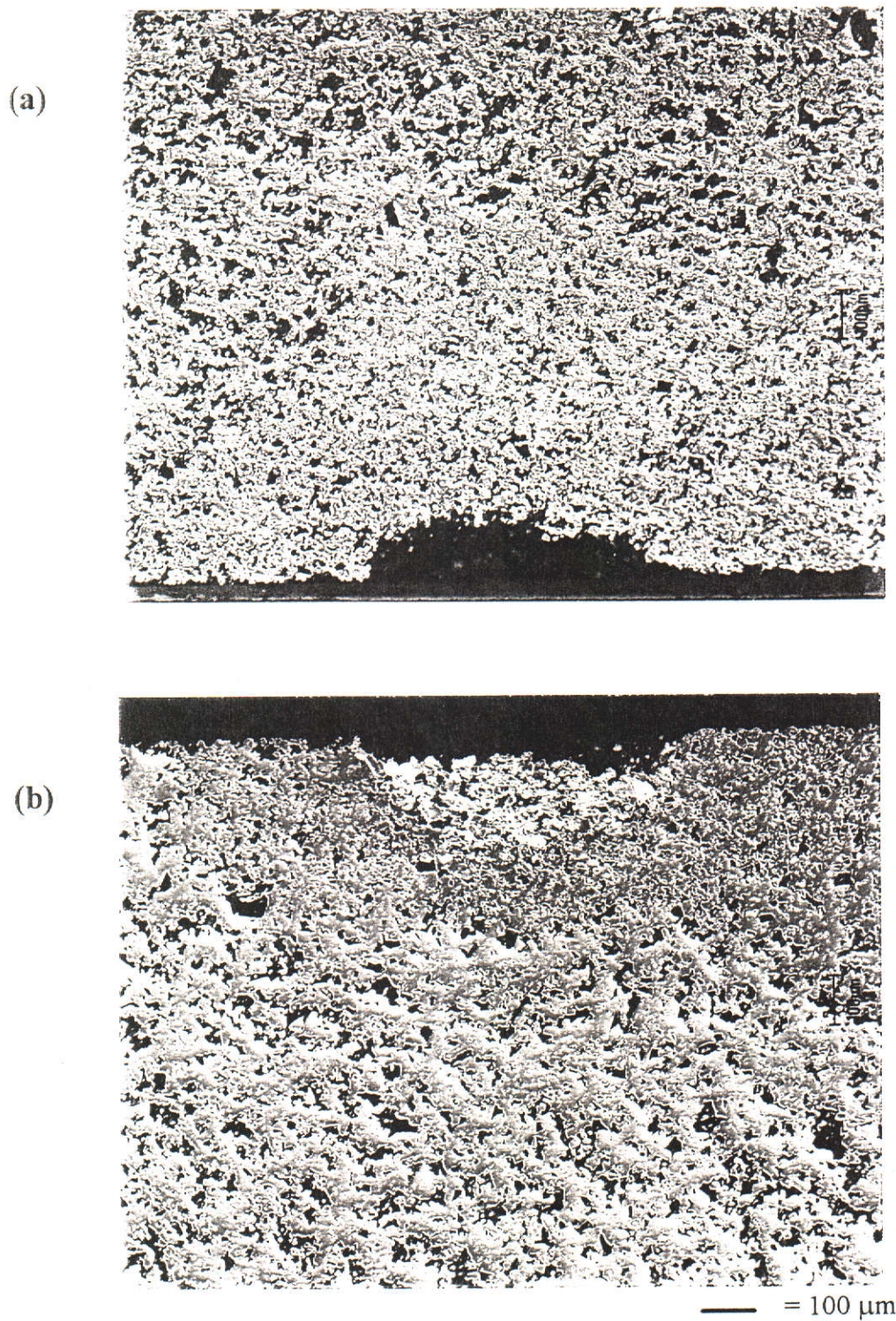
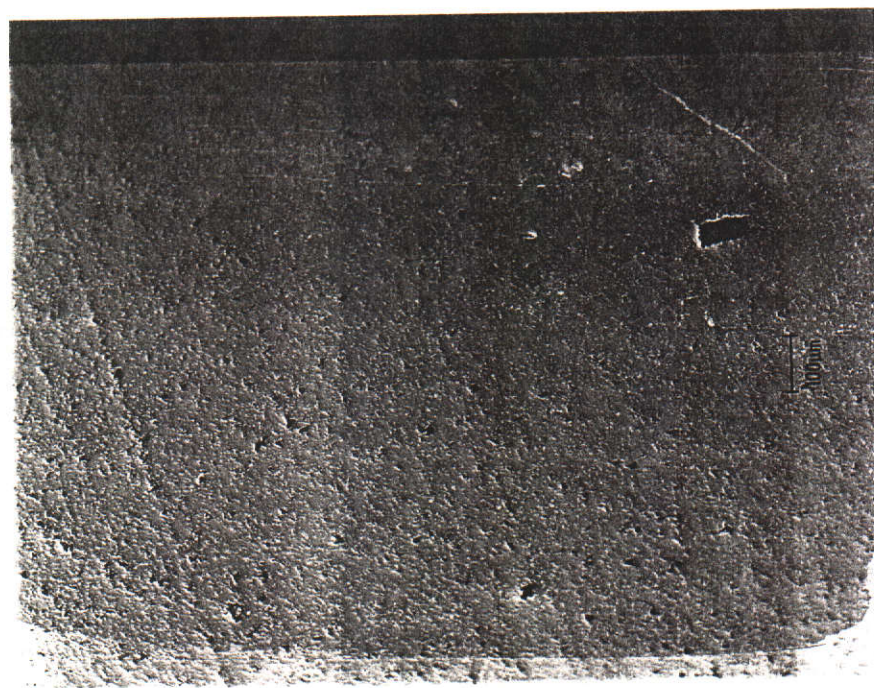


Figure 5.12 Nomarski optical micrographs of surface (a) and subsurface (b) of the near-surface region of AT/zirconia-alumina FGM at load of $P = 2000$ N. Note the grain pullout at the contact region indicating the damage-tolerance of the material.

(a)



(b)



— = 100 μm

Figure 5.13 Nomarski optical micrographs of surface (a) and subsurface (b) of the zirconia-alumina ceramic at load of $P = 2000$ N. Note the cone cracks at the contact region indicating the brittleness of the material.

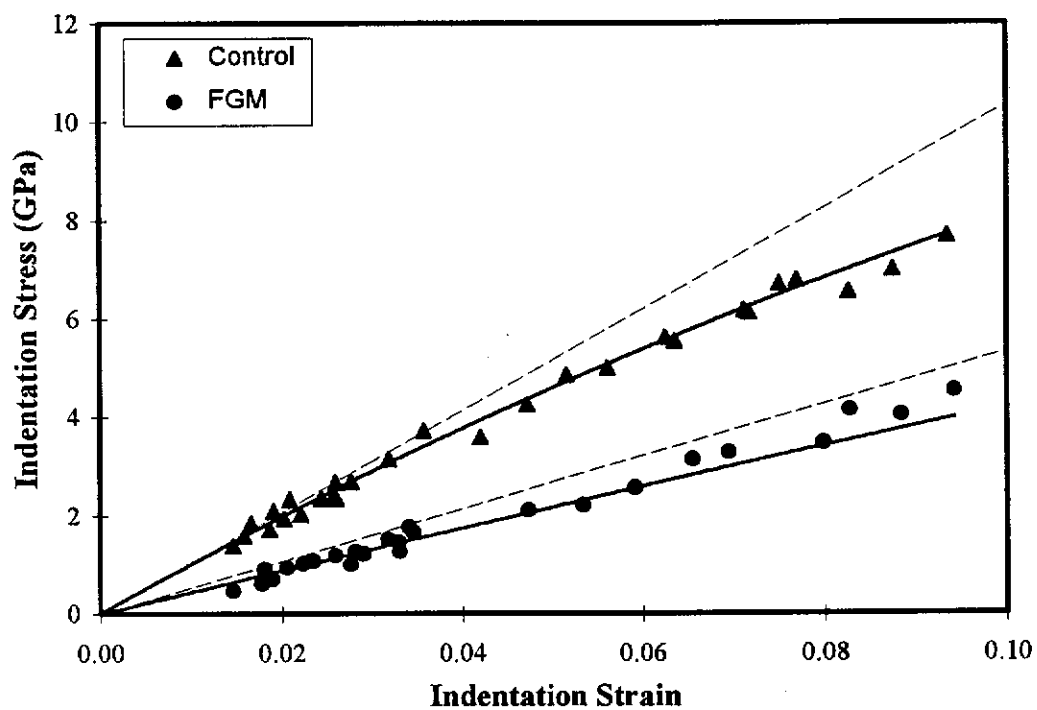


Figure 5.14 Indentation stress-strain curves for AT/zirconia-alumina FGM and zirconia-alumina control sample. Solid curves are empirical fits.

i.e. 2 mins against 30 mins. The observation that the FGM is readily machinable can be correlated to its lower hardness and better “ductility”. A similar behaviour has also been observed in a Ti_3SiC_2 ceramic (Barsoum and El-Raghy 1996) which could be readily machined like graphites.

5.3 DISCUSSION

The thermal and mechanical properties of the FGM are significantly different from those of the alumina-zirconia control sample. As shown from the results of previous sections, the gradual change in properties with depth is evident in the FGM. Moreover, the FGM, exhibits pronounced graded properties over the control sample which include lower thermal expansion, improved “ductility”, better fracture resistance, and damage-tolerance.

Thermal expansion measurements showed that the surface of the FGM has a relatively much lower thermal expansion coefficient than the core. This low thermal expansion may provide a pronounced thermal shock resistant surface layer. The thermal expansion coefficient value increased quite abruptly approaching that of the matrix after polishing to 0.5 mm depth.

Compositional distribution analysis (see Chapter 4) showed that the concentration of AT decreased sharply from 44.5 wt% on the surface to 9.5 wt% at 0.3 mm depth, and to approximately 8 wt% at 0.5 mm depth. It is believed that the apparent rapid reduction in AT with depth could be an artefact or anomaly resulting from preferential removal of AT grains during polishing. Corrections for these AT grain pull-outs should give a more gradual drop in AT content with depth.

Removal of AT-rich material from the surface will lead to a thermal expansion behaviour approaching that of the control sample (which is also the matrix of the FGM). This can be seen by comparing both the thermal expansion curves (Figures 5.1a and 5.1b) and thermal expansion coefficient values (Table 5.1) of the FGM and the control sample.

Both the FGM and the control sample exhibited thermal expansion hysteresis during thermal cycling. However, the degree of the hysteresis was higher for the as-fired (ie. unpolished) FGM than the polished one or the control sample. Hasselman *et al.* (1993) showed that the thermal hysteresis in alumina-AT composites annealed at 1200° C was due to the crack healing of AT. Since the near surface region of FGM has more AT, it has a higher degree of hysteresis than

the polished or core of FGM because the former exhibits more crack healings than the latter.

Neutron diffraction data from the AT/zirconia-alumina FGM collected at high temperatures showed that the $m \rightarrow t$ zirconia transformation occurred at approximately 750° C (Figure 5.2). Such transformation occurs in zirconia composites at above 1100° C (e.g., Wang and Stevens 1989). Since the transformation is followed by a drop of unit cell volume of 4%, such transformation can be associated with a decrease of thermal expansion coefficient value. Comparing the two materials, it appears that the presence of AT has enhanced the $m \rightarrow t$ zirconia transformation at a much lower temperature (750° C compared with 1100°C). It has been discussed previously that AT is also too weak to retain the tetragonal zirconia phase at room temperature (Wohlfromm *et al.* 1991). It can be argued here that the weakness of AT may also be responsible for the observed lower phase transformation temperature.

Crack healing during heating may occur in ceramic materials (e.g., Ohya *et al.* 1988; Mitomo *et al.* 1996). Such crack healing is followed by a reduction in dimensions of the material. As already discussed in the Chapter 4, microcracks have been observed in the FGM. It can be proposed here that crack healing has also occurred in the FGM and caused a reduction in the thermal expansion value during heating. This crack healing is believed to commence at 750° C (Figure 5.1), i.e. when the thermal expansion curve starts to decline. This together with $m \rightarrow t$ transformation are believed to be responsible for the observed sharp drop in thermal expansion values of the FGM at high temperature.

Observations showed that the presence of zirconia in the FGM has a favourable effect on the thermal decomposition of AT. However this effect is expected to be pronounced only for short-term annealing times (< 6 h). For longer annealing times (i.e. over 100 h), this favourable effect is expected to be insignificant because zirconia is not a good stabiliser for AT (Ishitsuka *et al.* 1987). As explained by Wohlfromm (1991), the negligible effect of zirconia in the stabilisation of AT may be attributed to the inability of relatively large Zr^{4+} (ionic radius = 0.79 Å) to substitute for the smaller Ti^{4+} (0.68 Å) or Al^{3+} (0.51 Å) in AT. Oxygen deficiency (Pena *et al.* 1987) in the AT structure may also reduce its ability to be stabilised by zirconia. On the contrary, MgO and Fe_2O_3 are excellent stabilisers of AT (Tilloca 1991; Battilana *et al.* 1995).

Microhardness tests showed that the FGM exhibits a soft surface but a hard core. The soft surface is believed to be due to the presence of a large amount of relatively soft AT. Since the amount of AT gradually reduces with depth, the hardness increases towards the core. The microhardness curves of FGM lie between those of Reuss-type and Voigt-type which indicate that the “modified” rule of mixtures is applicable for this material (Markworth *et al.* 1995a).

It is well known that most ceramics are brittle and hard. Recently, it was found that Ti_3SiC_2 ceramic exhibited high Young’s modulus, i.e. 326 GPa (Pampuch *et al.* 1993) but relatively low hardness, i.e. 6 GPa (Pampuch *et al.* 1993; Goto and Hirai 1987). Pampuch *et al.* (1993) noted that the hardness to Young’s modulus ratio (H_v/E) of this material is quite low, i.e. 0.012. It should be noted that this ratio for hard metals is in the range of 0.001 - 0.03 whereas for ceramics is 0.04 - 0.1. This ratio has been used as an elasto-plastic parameter for materials (McColm 1990). The Vicker’s hardness of the Ti_3SiC_2 ceramic was found to depend on load. Both the low H_v/E value and the load-dependence of microhardness suggest that the properties of the Ti_3SiC_2 ceramic are close to those of ductile metals.

The load-dependence of microhardness in the AT/zirconia-alumina FGM at a depth of 0.3 mm is evident from Figure 5.6. With average hardness of 5.6 GPa and Young’s modulus of 280 GPa, it is found that the H_v/E value is 0.02, which is notably comparable to the values of hard metals. This result indicates that the near surface region exhibits quasi-ductile behaviour.

The microhardness at the core of FGM is less load-dependent than that of the near-surface region. The average microhardness at the core is 10.7 GPa. Using the (estimated) Young’s modulus value of 380 GPa, it is found that the H_v/E value is 0.028. This suggests that the core is more brittle than the surface. However, the transition from ductile to brittle behaviour is a continuous one with no sharp discontinuity. The control sample, by contrast, exhibits almost no dependence of microhardness with load and has a H_v/E value of 0.042, indicating the obvious brittleness of the ceramic.

The micrographs of Vicker’s indentation and Hertzian contact damage of the FGM can be used to explain its pseudo-plastic behaviour. The presence of AT “softens” the alumina-zirconia matrix thus rendering AT excellent in energy absorption and crack attenuation. Figures 5.7 and 5.8 show the presence of extensive surface uplift such as grain pullout and microdamage around the

impressions which are not common in brittle ceramic materials. When an indentation is applied, ceramics usually exhibit a “sink in impression” (Figure 5.15a) which is caused by the densification below the tip of indentation (Zeng *et al.* 1996). Moreover, cracks normally propagate through the tips of the indentation implying the low fracture toughness of the materials. By contrast, metals exhibit a “rising of material” or surface uplift around the indentation above the unindented surface level (Figure 5.15b) as a result of shear or plastic deformation. In view of this, it can be argued that the FGM specimen exhibits characteristics akin to pseudo-plastic deformation during loading.

The “plastic” deformation of FGM is also shown by the Nomarski optical micrographs during Hertzian loading. Instead of showing cone cracks pattern which is typical of brittle material, the FGM exhibits extensive shear-driven grain debonding and grain pullouts within a hemispherical damage zone. It is believed that this damage behaviour imparts quasi-ductility to the FGM as can be discerned from its indentation stress-strain behaviour during loading.

As indicated from the microstructural observation, the presence of AT provided weak interphase boundaries and large thermal expansion mismatch with the matrix, namely alumina-zirconia, and thereby promoted “quasi-plastic” deformation in the matrix. Microscopic deformation in the system could be related to shear-driven frictional sliding at the weak interphase between AT and the matrix resulting in interface microfailures (Liu *et al.* 1996). Such microfailures account for the “machinability” of the FGM. It follows that the poor machinability of the alumina-zirconia control sample was due to its lack of such microfailures.

It has been shown by Runyan and Bennison (1991) and Braun *et al.* (1992) that an alumina-AT composite (20 vol% AT) exhibited pronounced flaw-tolerance. The composite, with 5.8 μm alumina grain size, displayed both considerable strength, i.e. approximately 250 MPa, and low degradation in strength with increasing contact load. The origins of flaw tolerance were attributed to crack deflection and grain bridging (Braun *et al.* 1992). Crack deflection was believed to arise from the presence of residual tensile stresses produced by thermal expansion mismatch between AT and alumina. The AT/zirconia-alumina FGM also showed the presence of extensive crack deflection and grain bridging (Figure 5.11). Although the indentation strength measurements were not performed, it is believed that the FGM also exhibited pronounced flaw-tolerance.

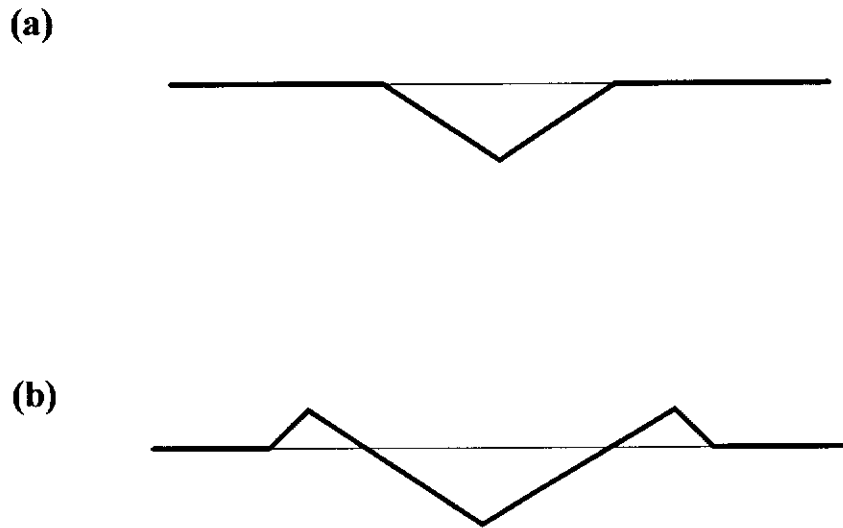


Figure 5.15 Response of materials to a Vicker's hardness indentation. (a) "sink in marks"; typical for ceramics, (b) "rising of material"; typical for metals.

The unique combination of properties in the FGM may lead to a wide range of applications. The surface exhibits unusual material properties, i.e. low thermal expansion coefficient, quasi-ductility, and damage tolerance. In contrast, the core is quite hard and, presumably, wear resistant. Overall the material displays excellent flaw-tolerance and machinability.

The ideal area of application for the AT/zirconia-alumina FGM is in environments which require the material to withstand severe thermal shock. Potential uses for this material are metal smelting crucibles, car exhaust pipes, lining tiles in the furnace, heating tubes, etc.

5.4 CONCLUSIONS

The AT/zirconia-alumina ceramic FGM produced by infiltration has graded thermal and mechanical properties, i.e. thermal expansion, microhardness, and Young's modulus. The near-surface region has a lower thermal expansion coefficient and Young's modulus than the core, i.e. $5.9 \times 10^{-6} \text{ }^{\circ}\text{C}^{-1}$ and 280 GPa

compared with $7.4 \times 10^{-6} \text{ }^{\circ}\text{C}^{-1}$ and 380 GPa. The surface is also softer than the core, i.e. 5.6 GPa compared with 10.7 GPa. These graded changes in properties are due to the presence of AT, which gradually reduces in amount from the surface to the core.

An anomalous thermal expansion behaviour at high temperature has been observed in the as-fired AT/zirconia-alumina FGM. Further investigation showed that this behaviour can be attributed to either $m \rightarrow t$ zirconia transformation or the occurrence of crack healing during heating. From the neutron diffraction study, it was found that the presence of AT has lowered the $m \rightarrow t$ zirconia transformation from 1100° C to 750° C.

The decomposition study showed that zirconia had a favourable short term stabilisation effect on AT, i.e. less than 6 h. This effect is expected to disappear after prolonged annealing times leading to complete decomposition of the material.

In contrast to the control sample, the FGM displayed a remarkable fracture resistance as indicated by the absence of indentation cracks and the display of extensive damage around indentations. The quasi-ductility and flaw-tolerance of FGM are confirmed by evidences such as load-dependence microhardness, low Hv/E value, good machinability, low “yielding” stress, and display of extensive grain debonding and grain pullout.

CHAPTER 6

CONCLUSIONS AND FURTHER WORK

6.1 CONCLUSIONS

In relation to the specific objectives of the research, conclusions which can be drawn from this study include the following:

1. A functionally-graded aluminium titanate (AT)/zirconia-alumina composite has been synthesised by infiltrating an alumina-zirconia green body in a solution containing titanium chloride. The graded character of the functionally-graded material (FGM) was confirmed by (a) a graded compositional study using quantitative x-ray Rietveld analysis showing the decrease of AT content and the increase of α -alumina content with depth, (b) x-ray emission measurement for elements in the material showing the decrease of TiK α intensity with depth, (c) Ti dot mapping at the near surface of the material indicating the decrease of Ti (and hence AT) content with depth, and (d) SEM micrographs at various specimen depths denoting the decrease in number of AT grains. Zirconia content increases slightly with depth counterbalancing the reduction of AT content.
2. The FGM exhibits graded thermal and mechanical behaviours. The surface is relatively soft, “ductile”, flaw or damage-tolerant, and has a low thermal expansion. The core, by contrast, is harder, more brittle, and has a higher thermal expansion. This combination of properties is believed to be potentially useful for applications where two extremely different characters are desired.
3. The presence of zirconia lowered the decomposition rate of AT in the FGM. Its effect, however, was considerable only for a short-term annealing time, i.e. less than 6 h. The effect was expected to be negligible for longer annealing time.

There are several other conclusions which can also be deduced from this study:

4. The external standard x-ray diffraction Rietveld analysis, with attenuation corrections applied using x-ray emission Compton scatter measurements, can provide a superior means for graded composition characterisation of FGMs over the electron-probe microanalysis technique, especially for determining the content of tetragonal zirconia and amorphous phase.

5. The presence of AT affects the grain growth of alumina and phase transformation temperature of zirconia. AT hinders the grain growth of alumina in the AT/zirconia-alumina FGM. The graded composition of AT leads to a graded grain size of alumina in the microstructure. Another effect of AT is its inability to retain the tetragonal zirconia phase at room temperature due to the weakness of AT grains. The presence of AT has enhanced $m \rightarrow t$ transformation during heating by lowering the transformation temperature from 1100° C to 750° C.
6. Both intergranular and intragranular microcrackings were observed in the FGM. Intragranular microcracks were found in AT and zirconia grains. In the latter, such microcracks were driven by the advancing intragranular cracking in the former.
7. The FGM demonstrates pronounced mechanical properties over the control sample and these include (a) much improved fracture resistance, as indicated qualitatively by the absence of cracks during Vickers and Hertzian loadings, (b) better “ductility” and damage-tolerance, as indicated by its load-dependent microhardness, low Hv/E value, lower “yielding” stress, grain debonding and grain pullout during Vickers and Hertzian loading, and (c) improved machinability.

6.2 FURTHER WORK

This thesis dealt with an investigation of the structure-property relationships of a functionally-graded aluminium titanate/zirconia-alumina composite. Much information on characters of the material has been revealed from the study, nevertheless, further work should be undertaken to fully understand the interplay between composition, microstructure and properties. This is essential before the full potential of this material can be realized in commercial applications. For further study, it is recommended that the following aspects be considered:

1. The infiltration kinetics prior to the synthesis of FGM deserves an in-depth study. Such study will provide valuable information for controlling the microstructure, distribution of phases and thus the graded properties.
2. The use of suitable stabiliser, such as MgO or Fe₂O₃ for preventing the decomposition of AT. This will lead to the development of FGMs which are thermally stable for long term use.

3. Measurement of residual stresses by x-ray and neutron diffraction. Large residual stresses are expected to be induced in the material by virtue of pronounced thermal expansion anisotropy in AT and thermal expansion mismatch between alumina and AT. Information on the nature and intensity of these stresses will be useful for the understanding of failure micromechanisms during Vickers and Hertzian loadings. Control of these stresses will also lead to the optimisation of specific properties.
4. Evaluate the thermal shock performance of FGM. This information is vital for the successful application of this material in environments which demand a high degree of thermal shock resistance.

REFERENCES

- Austin, A.E. and Schwartz, C.M. (1953). The Crystal Structure of Aluminium Titanate. *Acta Cryst.* **6**, 812-813.
- Australian Standards. (1989). Refractories and Refractory Materials - Physical Test Methods, Method 5: The Determination of Density, Porosity and Water Absorption: 1774.5, Standard Australia.
- Barsoum, M.W. and El-Raghy, T. (1996). Synthesis and Characterisation of a Remarkable Ceramic: Ti_3SiC_2 . *J. Am. Ceram. Soc.* **79**(7), 1953-1956.
- Battilana, G. Buscaglia, V., Nanni, P. and Aliprandi, G. (1995). Effect of MgO and Fe_2O_3 on Thermal Stability of Al_2TiO_5 . In *High Performance Materials in Engine Technology* (ed. Vincenzini, P.), pp. 147-154. Techna Srl.
- Bayer, G. (1971). *J. Less-Common Metal* **24**, 129. [Quoted from paper by Thomas and Stevens (1989a)].
- Bish, D.L. and Howard, S.A. (1988). Quantitative Phase Analysis Using the Rietveld Method. *J. Appl. Cryst.* **21**, 86-91.
- Braun, L.M., Bennison, S.J. and Lawn, B.R. (1992). Objective Evaluation of Short-Crack Toughness Curves Using Indentation Flaws: Case Study on Alumina-based Ceramics. *J. Am. Ceram. Soc.* **75**(11), 3049-3057.
- Buessem, W.R., Thielke, N.R. and Sarakauskas, R.V. (1952). *Ceramic Age* **60**, 38. [Quoted from paper by Thomas and Stevens (1989a)].
- Buscaglia, V., Nanni, P., Battilana, G., Aliprandi, G. and Carry, C. (1994). Reaction Sintering of Aluminium Titanate: I - Effect of MgO Addition. *J. Euro. Ceram. Soc.* **13**, 411-417.
- Bush, E.A. and Hummel, F.A. (1959). High-Temperature Mechanical Properties of Ceramic Materials: II. *J. Am. Ceram. Soc.* **42**(8), 388-391.
- Caglioti, G., Paoletti, A. and Ricci, F.P. (1958). Choice of Collimator for Crystal Spectrometer for Neutron Diffraction. *Nucl. Instrum.* **3**, 223-228.
- Cai, H., Kalceff, M.A.S., Lawn, B.R. (1994). Deformation and Fracture of Mica-containing Glass-ceramic in Hertzian Contacts. *J. Mater. Res.* **9**(3), 762-770.

- Callister, W.D.J. (1991). *Materials Science and Engineering: An Introduction*. John Wiley and Sons, New York.
- Claussen, N. (1976). Fracture Toughness of Al_2O_3 with an Unstabilized ZrO_2 Dispersed Phase. *J. Am. Ceram. Soc.* **59**(1-2), 49-51.
- Cleveland, J.J. and Bradt, R.C. (1987). Grain Size/Microcracking Relations for Pseudobrookite Oxides. *J. Am. Ceram. Soc.* **61**(11-12), 478-481.
- Coble, R.L. (1961). Sintering of Crystalline Solids - II. Experimental Test of Diffusion Models in Porous Compacts. *J. Appl. Phys.* **32**(5), 793-799.
- Cullity, B.D. (1978). *Elements of X-Ray Diffraction*. Addison-Wesley, USA.
- Dollase, W.A. (1986). Correction of Intensities for Preferred Orientation in Powder Diffractometry: Application of the March Model. *J. Appl. Cryst.* **19**, 267-272.
- Dörre, E. and Hübner, H. (1984). *Alumina*. Springer-Verlag, Berlin.
- El-Raghy, T., Zavaliangos, A., Barsoum, M.W. and Kalidindi, S.R. (1996). Damage Mechanism Around Hardness Indentation in Ti_3SiC_2 . Unpublished work.
- Evans, A.G. and Charles, E.A. (1980). Fracture Toughness Determination by Indentations. *J. Am. Ceram. Soc.* **59**(7-8), 371-372.
- Feltz, A. and Schmidt, F. (1990). Preparation Studies of Amorphous Al_2TiO_5 . *J. Euro. Ceram. Soc.* **6**, 107-110.
- Freudenberg, B. and Mocellin, A. (1987). Aluminum Titanate Formation by Solid-State Reaction of Fine Al_2O_3 and TiO_2 Powders. *J. Am. Ceram. Soc.* **70**(1), 33-38.
- Fukui, Y., Takashima, K. and Ponton, C.B. (1994). Measurement of Young's Modulus and Internal Friction of an *in situ* Al- Al_3Ni functionally gradient material. *J. Mater. Sci.* **29**, 2281-2288.
- Gasgnier, M. (1992). Phase Transitions and Microstructures of: a) Zirconia Ceramics as: $\text{ZrO}_2\text{-M}_x\text{O}_y$ ($\text{M} = \text{Y}, \text{Sc}, \text{Mg}, \text{Ca}, \text{Al}$ and Mullite) Systems; b) Alumina and $\text{Al}_x\text{M}_y\text{O}_z$ Systems. In *Key Engineering Materials*, pp. 247-292. Trans Tech Publication, Switzerland.
- Glass, S.J. and Green, D.J. (1987). Surface Modification of Ceramics by Partial Infiltration. *Adv. Ceram. Mat.* **2**(2), 29-31.

- Goto, T. and Hirai, T. (1987). Chemically Vapor Deposited Ti_3SiC_2 . *Mat. Res. Bull.* **22**, 2295-1202.
- Green, D.J., Hannink, R.H.J. and Swain, M.V. (1989). *Transformation Toughening of Ceramics*. LRC Press, Boca Raton (Florida).
- Hamano, K., Nakagawa, Z., Sawano, K. and Hasegawa, M. (1981). *Nippon Kagaku* **10**, 1647. [Quoted from paper by Thomas and Stevens (1989a)].
- Hansson, C.B. (1972). *Physical Data Book*. Pergamon Press, Oxford.
- Hasselmann, D.P.H., Donaldson, K.Y., Anderson, E.M., Johnson, J.A. (1993). Effect of Thermal History on the Thermal Diffusivity and Thermal Expansion of an Alumina-Aluminum Titanate Composite. *J. Am. Ceram. Soc.* **76**(9), 2180-2184.
- Hennicke, H.W. and Lingenberg, W. (1986). Formation of Aluminium Titanate. *J. de Phys.* **2**(47), 533-536.
- Hill, R.J. (1991). Expanded Use of the Rietveld Method in Studies of Phase Abundance in Multiphase Mixture. *Powder Diff.* **6**(2), 74-77.
- Hill, R.J. (1993). Data Collection Strategies: Fitting in Experiment to the Need (Appendix). In *The Rietveld Method* (ed. Young, R. A.), pp. 95-101. Oxford University Press, Oxford.
- Hill, R.J. and Cranswick, L.M.D. (1994). International Union of Crystallography Commission on Powder Diffraction Rietveld Refinement Round Robin. II. Analysis of Monoclinic Zirconia. *J. Appl. Cryst.* **27**, 802-844.
- Hill, R.J. and Howard, C.J. (1986). *LHPM, Rietveld Refinement Program Manual*. Australian Atomic Energy Commission, Lucas Heights Research Laboratory, Menai, NSW.
- Hill, R.J. and Howard, C.J. (1987). Quantitative Phase Analysis from Neutron Powder Diffraction Data Using the Rietveld Method. *J. Appl. Cryst.* **20**, 467-474.
- Hirai, T. (1996). Functional Gradient Materials. In *Processing of Ceramics (Part 2)* (ed. Brook, R. J.). VCH Verlagsgesellschaft mbH, Weinheim.
- Hirano, T. and Wakashima, K. (1995). Mathematical Modelling and Design. In *MRS Bulletin*, June, pp 40-42.

- Honeyman-Colvin, P. and Lange, F.F. (1996). Infiltration of Porous Alumina Bodies with Solution Precursors: Strengthening via Compositional Grading, Grain Size Control and Transformation Toughening. *J. Am. Ceram. Soc.* **79**(7), 1810-1814.
- Howard, C.J. and Kennedy, S. Neutron Diffraction. *Materials Forum*, **18**, pp 155-176.
- Hubbard, C.R., Evans, E.H. and Smith, D.K. (1976). The Reference Intensity Ratio, I/I_c , for Computer Simulated Powder Patterns. *J. Appl. Cryst.* **9**, 169-174.
- Hwang, C., Nakagawa, Z. and Hamano, K. (1994). Microstructures and Mechanical Properties of TiO_2 -doped Alumina Ceramics Owing to Decomposition of Formed Al_2TiO_5 . *J. Ceram. Soc. Jap.* **102**(2), 253-258.
- Ishitsuka, M., Sato, T., Endo, T. and Shimada, M. (1987). Synthesis and Thermal Stability of Aluminum Titanate Solid Solutions. *J. Am. Ceram. Soc.* **70**(2), 69-71.
- Kameyama, T. and Yamaguchi, T. (1976). *Yogyo Kyokaishi* **84**, 589. [Quoted from paper by Thomas and Stevens (1989)].
- Kato, E., Daimon, K. and Takahashi, J. (1980). Decomposition Temperature of β - Al_2TiO_5 . *J. Am. Ceram. Soc.* **63**(5-6), 355-356.
- Kisi, E.H., Howard, C.J. and Hill, R.J. (1989). Crystal Structure of Orthorhombic Zirconia in Partially Stabilized Zirconia. *J. Am. Ceram. Soc.* **72**(9), 1757-1760.
- Kisi, E.H. (1994). Rietveld Analysis of Powder Diffraction Patterns. *Materials Forum* **18**, 135-153.
- Klug, H.P. and Alexander, L.E. (1974). *X-Ray Diffraction Procedures for Polycrystalline and Amorphous Materials*. 2nd Edition. John Wiley and Sons, New York.
- Koizumi, M. (1992). The Concept of FGM. In *Second International Symposium on Functionally Gradient Materials* (ed. Holt, J. B., Koizumi, M., Hirai, T. and Munir, Z.A.), pp. 3-10. The American Ceramic Society, Westerville, Ohio, San Fransisco, CA.

- Lange, F.F. and Hirlinger, M.M. (1984). Hindrance of Grain Growth in Al_2O_3 by ZrO_2 Inclusions. *J. Am. Ceram. Soc.* **67**(3), 164-168.
- Lee, B. and Hiraga, K. (1994). Crack Propagation and Deformation Behavior of Al_2O_3 -24 vol% ZrO_2 Composite Studied by Transmission Electron Microscopy. *J. Mater. Res.* **9**(5), 1199-1207.
- Lewis, J., Schwarzenbach, D. and Flack, H.D. (1982). Electric Field Gradients and Charge Density in Corundum, $\alpha\text{-Al}_2\text{O}_3$. *Acta Cryst.* **A38**, 733-739.
- Liu, H., Lawn, B.R. and Hsu, S.M. (1996). Hertzian Contact Response of Tailored Silicon Nitride Multilayers. *J. Am. Ceram. Soc.* **79**(4), 1009-1014.
- Low, I.M., Hwang, H. and Skala, R.D. (1995). Epoxy-modified Bi(Pb)SrCaCuO superconductors with improved mechanical properties. *J. Mater. Sci. Lett.* **14**, 384-386.
- Low, I.M., Skala, R.D. and Mohazzab-H, G. (1994). Mechanical and Fracture Properties of Epoxy-modified YBaCu(123). *J. Mater. Sci. Lett.* **13**, 1340-1342.
- Low, I.M., Skala, R., Richards, R. and Perera, D.S. (1993). Synthesis and Properties of Novel Mullite-Zirconia-toughened Alumina Composites. *J. Mater. Sci. Lett.* **12**, 1985-1987.
- Low, I.M., Skala, R.D. and Zhou, D. (1996a). Synthesis of Functionally gradient Aluminium titanate/Alumina Composites. *J. Mater. Sci. Lett.* **15**, 345-347.
- Low, I.M., Yamaguchi, S., Nakahira, A. and Niihara, K. (1996b). Functionally-graded Epoxy-modified Zirconium Phosphate Materials Produced by an Infiltration Process. Pre-print of: *Proceedings of the 4th International Symposium on Functionally Graded Materials*, Tsukuba, Japan 21-24 Oct 1996.
- Markworth, A.J., Ramesh, K.S. and Parks, Jr. W.P. (1995a). Review Modelling Studies Applied to Functionally Graded Materials. *J. Mater. Sci.* **30**, 2183-2193.
- Markworth, A.J. and Saunders, J.H. (1995b). A Model of Structure Optimization for a Functionally Graded Material. *Mater. Lett.* **22**(1-2), 103-107.
- Marple, B.R. and Boulanger, J. (1994). Graded Casting of Materials with Continuous Gradients. *J. Am. Ceram. Soc.* **77**(10), 2747-2750.

- Marple, B.R. and Green, D.J. (1989). Mullite/Alumina Particulate Composites by Infiltration Processing. *J. Am. Ceram. Soc.* **72**(11), 2043-2048.
- Marple, B.R. and Green, D.J. (1990). Mullite/Alumina Particulate Composites by Infiltration Processing: II, Infiltration and Characterization. *J. Am. Ceram. Soc.* **73**(12), 3611-3616.
- Marple, B.R. and Green, D.J. (1991). Mullite/Alumina Particulate Composites by Infiltration Processing: III, Mechanical Properties. *J. Am. Ceram. Soc.* **74**(10), 2453-2459.
- Marple, B.R. and Green, D.J. (1992). Mullite/Alumina Particulate Composites by Infiltration Processing: III, Residual Stress Profile. *J. Am. Ceram. Soc.* **75**(1), 44-51.
- Marple, B.R. and Green, D.J. (1993). Graded Compositions and Microstructures by Infiltration Processing. *J. Mater. Sci.* **28**, 4637-4643.
- McColm, I.J. (1990). *Ceramic Hardness*. Plenum Press, New York. [Quoted from paper by El-Raghy *et al.* (1996)].
- Misra, C. (1986). *Industrial Alumina Chemicals*, American Chemical Society Monograph 184.
- Mitomo, M., Nishimura, T. and Tsutsumi, M. (1996). Crack Healing In Silicon Nitride and Alumina Ceramics. *J. Mater. Sci. Lett.* **15**, 1976-1978.
- Morishima, H., Kato, Z. and Uematsu, K. (1986). Development of Aluminium Titanate-Mullite Composites Having High Thermal Shock Resistance. *J. Am. Ceram. Soc.* **69**(10), C226-C227.
- Morosin, B. and Lynch, R.W. (1972). Structure Studies on Al_2TiO_5 at Room Temperature and 600° C. *Acta Cryst.* **B28**, 1040-1046.
- Muramatsu, K., Kawasaki, A., Taya, M. and Watanabe, R. (1990). In *Proceedings of the 1st International Symposium on FGM*, pp. 53, Sendai, Japan. [Quoted from paper by Markworth *et al.* (1995a)].
- Navrotsky, A. and Kleppa, O.J. (1967). Enthalpy of the Anatase-Rutile Transformation. *J. Am. Ceram. Soc.* **50**(11), 626.
- Norrish, K. and Chappell, B.W. (1977). X-Ray Fluorescence Spectrometry. In *Physical Methods of Determinative Mineralogy* (ed. Zussman, J.), pp. 242-244. Academic Press, London.

- O'Connor, B.H. and Chang, W-J. (1985). Use of Primary Beam Filtration in Estimating Mass Attenuation Coefficients by Compton Scattering. In *Advances in X-Ray Analysis* (ed. Barret, C. S. et al.). Plenum Press, New York.
- O'Connor, B.H. and Raven, M.D. (1988). Application of the Rietveld Refinement Procedure in Assaying Powdered Mixtures. *Powder Diffr.* **3**(3), 2-6.
- O'Connor, B.H. and Thomas, A.G. (without year). X-ray Analysis Toolkit. Version 3.0. Curtin University of Technology, Perth, Australia.
- Ohya, Y., Hamano, K. and Nakagawa, Z. (1983). Microstructure and Mechanical Strength of Aluminum Titanate Ceramics Prepared from Synthesized Powders. *Yogyo-Kyokai-Shi* **91**(6), 290-297.
- Ohya, Y., Nakagawa, Z. and Hamano, K. (1987). Grain Boundary Microcracking due to Thermal Expansion Anisotropy in Aluminium Titanate Ceramics. *J. Am. Ceram. Soc.* **70**(8), C184-C186.
- Ohya, Y., Nakagawa, Z. and Hamano, K. (1988). Crack Healing and Bending Strength of Aluminum Titanate Ceramics at High Temperature. *J. Am. Ceram. Soc.* **71**(5), C232-C233.
- Ohya, Y. and Nakagawa, Z. (1996). Measurement of Crack Volume due to Thermal Expansion Anisotropy in Aluminium Titanate Ceramics. *J. Mater. Sci.* **31**, 1555-1559.
- Okada, K. and Sakuma, T. (1996). Tensile Ductility in Zirconia-dispersed Alumina at High Temperature. *J. Am. Ceram. Soc.* **79**(2), 499-502.
- Padture, N.P., Bennison, S.J. and Chan, H.M. (1993). Flaw-Tolerance and Crack-Resistance Properties of Alumina and Aluminum Titanate Composites with Tailored Microstructures. *J. Am. Ceram. Soc.* **76**(9), 2312-2320.
- Pajares, A., Wei, L. and Lawn, B. (1996). Contact Damage in Plasma-Sprayed Alumina-Based Coatings. *J. Am. Ceram. Soc.* **79**(7), 1907-1914.
- Pampuch, R., Lis, J., Piekarczyk, J. and Stobierski, L. (1993). Ti_3SiC_2 -Based Materials Produced by Self-Propagating High-Temperature Synthesis (SHS) and Ceramic Processing. *J. Mater. Synthesis & Processing* **1**, 93.
- Pena, P., de Aza, S. and Moya, J.S. (1987). Microstructure and Mechanical Properties of an Al_2TiO_5 -Mullite- ZrO_2 Composite Obtained by Reaction

- Sintering. In *Ceramic Microstructures '86. Role of Interfaces*. (ed. Pask, J. and Evans, A.G.), pp. 847-857. Plenum Press, New York & London.
- Persson, M., Hermansson, L. and Carlsson, R. (1981). Investigation of the Stability of Aluminium Titanate Ceramics. *Science of Ceramics* **11**, 479-484.
- Pratapa, S. and Low, I.M. (1996). Synthesis and Properties of Functionally-gradient Aluminium titanate-Mullite-ZTA Composites. *J. Mater. Sci. Lett.* **15**, 800-802.
- Requena, J., Moya, J.S., Pena, P. (1992). Al_2TiO_5 - Al_2O_3 Functionally Gradient Materials Obtained by Sequential Slip Casting. In *Functionally Gradient Materials* (ed. Holt, B. J., Koizumi, M., Hirai, T. and Munir, Z.A.). The American Ceramic Society, Westerville.
- Reynolds, R.C. (1963). Matrix Correction in Trace Element Analysis by X-ray Fluorescence Estimation of the Mass Absorption Coefficient by Compton Scattering. *Am. Mineral.* **48**, 1133-1143.
- Richerson, D.W. (1992). *Modern Ceramic Engineering: properties, processing and use in design*. M. Dekker, New York.
- Rietveld, H.M. (1967). Line Profiles of Neutron Powder-Diffraction Peaks for Structure Refinement. *Acta Cryst.* **22**, 151-152.
- Rietveld, H.M. (1969). A Profile Refinement Method for Nuclear and Magnetic Sources. *J. Appl. Cryst.* **2**, 65-71.
- Root, J.H., Sullivan, J.D. and Marple, B.R. (1991). Residual Stresses in Alumina-Mullite Composite. *J. Am. Ceram. Soc.* **74**(3), 579-583.
- Runyan, J.L. and Bennison, S.J. (1991). Fabrication of Flaw-tolerant Aluminium-titanate-reinforced Alumina. *J. Euro. Ceram. Soc.* **7**, 93-99.
- Ruys, A.J., Kerdic, J.A. and Sorrell, C.C. (1996). Thixotropic Casting of Ceramic-Metal Functionally Gradient Materials. *J. Mater. Sci.* **31**, 4347-4355.
- Sarkar, P., Huang, X. and Nicholson, P.S. (1993). Zirconia/Alumina Functionally Graded Composites by Electrophoretic Deposition Techniques. *J. Am. Ceram. Soc.* **76**(4), 1055-1056.
- Sasaki, M. and Hirai, T. (1991). Fabrication and Properties of Functionally Gradient Materials. *J. Ceram. Soc. Jap.* **99**(10), 970-980.

- Shintani, H., Sato, S. and Saito, Y. (1975). Electron-Density Distribution in Rutile Crystals. *Acta Cryst.* **B31**, 1981.
- Sitepu, H. (1991). *Characterisation of Preferred Orientation in Crystalline Materials by X-ray Powder Diffraction*. MSc thesis, Curtin University of Technology, Perth, Australia.
- Smith, D.K. and Newkirk, H.W. (1965). The Crystal Structure of Baddeleyite (Monoclinic Zirconia) and Its Relation to the Polymorphism of ZrO_2 . *Acta Cryst.* **18**, 983-991.
- Sudre, O. and Lange, F.F. (1992). Effect of Inclusions on Densification: I, Microstructural Development in an Al_2O_3 Matrix Containing a High Volume Fraction of ZrO_2 Inclusions. *J. Am. Ceram. Soc.* **75**(3), 519-524.
- Teufer, G. (1962). The Crystal Structure of Tetragonal ZrO_2 . *Acta Cryst.* **15**, 1187.
- Thomas, H.A. J. and Stevens, R. (1989a). Aluminium Titanate - A Literature Review. Part 1: Microcracking Phenomena. *Br. Ceram. Trans.* **88**, 144-151.
- Thomas, H.A. J. and Stevens, R. (1989b). Aluminium Titanate - A Literature Review. Part 2: Engineering Properties and Thermal Stability. *Br. Ceram. Trans.* **88**, 184-190.
- Tilloca, G. (1991). Thermal Stabilization of Aluminium Titanate and Properties of Aluminium Titanate Solid Solution. *J. Mater. Sci.* **26**, 2809-2814.
- Tu, W.C. and Lange, F.F. (1995). Liquid Precursor Processing of Powder Compacts: I, Kinetic Studies and Microstructure Development. *J. Am. Ceram. Soc.* **78**(12), 3277-3282.
- Tuffe, S. and Marple, B.R. (1995). Graded Casting: Process Control for Producing Tailored Profile. *J. Am. Ceram. Soc.* **78**(12), 3297-3303.
- Vasudevan, A.K., Mani, T.V., Damodaran, A.D. and Warriar, K.G.K. (1995). Dependence of Aluminium Titanate Formation on Precursor Characteristics. *J. Mater. Sci. Lett.* **14**, 1317-1320.
- Wakashima, K., Hirano, T. and Niino, M. (1990). In *Space Applications of Advance Structural Materials*, pp. 97. European Space Agency. [Refer to the paper by Markworth et al. (1995a)].

- Wang, J. and Stevens, R. (1989). Review: Zirconia-toughened Alumina (ZTA) Ceramics. *J. Mat. Sci.* **24**, 3421-3440.
- Wiles, D.B. and Young, R.A. (1981). A New Computer Program for Rietveld Analysis of X-Ray Powder Diffraction Patterns. *J. Appl. Cryst.* **14**, 149-151.
- Wohlfromm, H., Epicier, T., Moya, J.S., Pena, P. and Thomas, G. (1991). Microstructural Characterization of Aluminium Titanate-based Composite Materials. *J. Euro. Ceram. Soc.* **7**, 385-396.
- Wurst, J.C. and Nelson, J.A. (1972). Lineal Intercept Technique for Measuring Grain Size in Two-Phase Polycrystalline Ceramics. *J. Am. Ceram. Soc.* **55**(2), 109.
- Young, R.A. (1993). Introduction to the Rietveld Method. In *The Rietveld Method* (ed. Young, R. A.). Oxford University Press, New York.
- Zeng, K., Soederlund, E., Giannakopoulos, A.E. and Rowcliffe, D.J. (1996). Controlled Indentation: A General Approach to Determine Mechanical Properties of Brittle Materials. *Acta Mater.* **44**, 1127.

APPENDIX 1: CRYSTALLOGRAPHIC DATA

The crystallographic data for phases used in the Rietveld analysis are listed in this appendix. Cell parameters are the only parameters in the list which were refined during the Rietveld refinements, except for aluminium titanate due to the lack of crystallographic data from literature. The overall isotropic temperature factor (not listed here) was refined only for aluminium titanate. The listed atomic occupancies are the Rietveld site occupancies, whereas those reported in the literature are generally true values. The references cited for the input data model are as listed in Chapter 3, section 3.3.2.

Phase : Alumina (Al_2O_3)
 Symmetry : Trigonal
 Space Group : R-3c
 Formula Unit : Al_2O_3
 Formula Units per Cell : 6
 Unit Cell Volume : 0.25498 nm^3
 Unit Cell Molecular Weight : $101.96 \text{ g mol}^{-1}$
 Cell Parameters :
 $a = 0.47602 \text{ nm}, \quad b = 0.47602 \text{ nm}, \quad c = 1.29933 \text{ nm}$
 $\alpha = 90^\circ, \quad \beta = 90^\circ, \quad \gamma = 120^\circ$

Atomic Positions

Atom	Wyckoff Site	x	y	z	Occupancy
Al	12c	0	0	0.3522	0.3333
O	18e	0.3061	0	0.25	0.5000

Reference:

Lewis, J., Schwarzenbach, D. and Flack, H.D. (1982). Electric Field Gradients and Charge Density in Corundum, $\alpha\text{-Al}_2\text{O}_3$. *Acta Cryst. A* **38**, 733-739

Phase : Zirconia (ZrO₂)
 Symmetry : Monoclinic
 Space Group : P 1 21/c 1
 Formula Unit : ZrO₂
 Formula Units per Cell : 4
 Unit Cell Volume : 0.1404 nm³
 Unit Cell Molecular Weight : 123.22 gmol⁻¹
 Cell Parameters :
 a = 0.5145 nm, b = 0.5207 nm, c = 0.5311 nm
 α = 90°, β = 99.2°, γ = 90°

Atomic Positions

Atom	Wyckoff Site	x	y	z	Occupancy
Zr	4e	0.2758	0.0411	0.2082	1.000
O1	4e	0.0703	0.3359	0.3406	1.000
O2	4e	0.4423	0.7549	0.4789	1.000

Reference:

Smith, D.K. and Newkirk, H.W. (1967). The Crystal Structure of Baddeleyite (monoclinic ZrO₂) and Its Relation to the Polymorphism of ZrO₂. *Acta Cryst.* A18, 983-991

Phase : Zirconia (ZrO₂)
 Symmetry : Tetragonal
 Space Group : P 42/n m c S
 Formula Unit : ZrO₂
 Formula Units per Cell : 2
 Unit Cell Volume : 0.0698nm³
 Unit Cell Molecular Weight : 123.22 gmol⁻¹
 Cell Parameters :
 a = 0.3640 nm, b = 0.3640 nm, c = 5.270 nm
 α = 90°, β = 90°, γ = 90°

Atomic Positions

Atom	Wyckoff Site	x	y	z	Occupancy
Zr	2a	0.7500	0.2500	0.7500	0.1250
O	4d	0	0.5000	0.4250	0.2500

Reference:

Teufer, G. (1962). The Crystal Structure of Tetragonal ZrO₂. *Acta Cryst.* **15**,
 1187

Phase : Aluminium Titanate ($\text{Al}_2\text{O}_3 \cdot \text{TiO}_2$)
 Symmetry : Orthorhombic
 Space Group : $C m c m$
 Formula Unit : Al_2TiO_5
 Formula Units per Cell : 4
 Unit Cell Volume : 0.3238 nm^3
 Unit Cell Molecular Weight : $181.86 \text{ g mol}^{-1}$
 Cell Parameters :
 $a = 0.3557 \text{ nm}, \quad b = 0.9436 \text{ nm}, \quad c = 0.9648 \text{ nm}$
 $\alpha = 90^\circ, \quad \beta = 90^\circ, \quad \gamma = 90^\circ$

Atomic Positions

Atom	Wyckoff Site	x	y	z	Occupancy
Ti	4c	0	0.19	0.25	0.2500
Al	8f	0	0.145	0.56	0.5000
O1	4c	0	0.76	0.25	0.2500
O2	8f	0	0.04	0.12	0.5000
O3	8f	0	0.32	0.09	0.5000

Reference:

Austin, A.E. and Schwartz, C.M. (1953). The Crystal Structure of Aluminum Titanate. *Acta Cryst.* 6. 812-813

APPENDIX 2: RIETVELD REFINEMENT OUTPUT

Rietveld refinements were applied to the x-ray diffraction patterns of AT/zirconia-alumina FGM collected at various depths. Rietveld program LHPM (Hill *et al.* 1986) was used for the refinements. The refined parameters included background profile parameters, 2θ -zero shift (both are global parameters), scale factors, peak profile function parameters, lattice parameters, preferred-orientation factor, asymmetry factor, and line function mixing factor. Thermal parameter and position coordinates were only refined for AT. The parameters of interest for phase analysis are scale factors and lattice parameters. The lattice parameters were used to calculate the unit cell volume of each phase. Both parameters were then applied to the external standard 'ZMV' expression with the correlated mass attenuation coefficient value.

Table A2.1 shows the Rietveld refined parameters of the patterns.

Table A2.1 Rietveld Refinement Output of X-ray Diffraction Patterns of AT/Zirconia-Alumina FGM.

Phase	Parameter	d=0.0mm	d=0.1mm	d=0.3mm	d=0.4mm	d=0.8mm	d=1.2mm	d=1.5mm
1. AT	Background							
	B ₀	26(2)	32(2)	37(1)	37(1)	40(2)	33(1)	40(2)
	B ₁	.13(6)	-.12(6)	-.20(6)	-.27(5)	-.31(6)	-.20(6)	-.35(6)
	B ₂	-.0008(5)	.0002(5)	.0007(5)	.0015(5)	.0016(5)	.010(5)	.024(5)
	Zeropoint							
	2-th	.16(1)	-.12(1)	-.043(5)	-.450(7)	-.418(7)	-.083(5)	-.176(6)
	U	.26(3)	.19(2)	.31(8)	.22(7)	.16(8)	1.8(5)	.5(4)
	V	-.012	-.012	-.012	-.012	-.012	-.012	-.012
	W	.027(3)	.021(3)	.028(8)	.045(7)	.049(10)	-.04(1)	-.03(12)
	G ₀	.36(4)	.50(5)	.4(1)	.39(12)	.5(2)	.9(2)	1.3(4)
Cell parameters	Peak factor							
	Asymmetry	-.02(1)	-.039(8)	.05(1)	.001(11)	.0002(131)	.06(2)	.01(3)
	a	3.5862(7)	3.5840(5)	3.5807(9)	3.5746(10)	3.5736(12)	3.5719(28)	3.5791(28)
	b	9.4653(18)	9.4524(18)	9.4538(34)	9.4481(34)	9.4522(39)	9.4506(78)	9.4670(94)
	c	9.7031(22)	9.6802(17)	9.6753(28)	9.6692(31)	9.6572(37)	9.6730(59)	9.6550(67)
	Ti	.182(1)	.174(1)	.172(3)	.174(3)	.171(3)	.146(4)	.129(10)
	Al	.139(1)	.132(1)	.136(3)	.135(3)	.137(4)	.122(4)	.136(9)
	z	.590(1)	.591(1)	.598(3)	.598(2)	.573(5)	.626(3)	.629(4)
	O ₁	.756(2)	.760(3)	.759(8)	.758(8)	.767(7)	.746(12)	.724(19)
	O ₂	.04	.04	.04	.04	.04	.04	.04
Atomic Positions	z	.130(1)	.126(2)	.119(4)	.120(4)	.112(6)	.066(6)	.037(18)
	O ₃	.320(2)	.308(3)	.308(6)	.306(6)	.325(6)	.268(12)	.266(20)
	z	.079(2)	.082(2)	.072(4)	.071(4)	.075(7)	.043(6)	.071(13)
	Thermal factor	1.0(2)	1.3(2)	1.4(5)	.8(4)	.8(5)	1.1(9)	1.5(12)
	PO	.90(1)	.92(1)	.99(3)	1.02(3)	.91(3)	1.5(1)	1.4(1)
	Scale factor*	180(4)	152(4)	52(3)	46(3)	40(3)	44(5)	31(5)

Table A2.1 Rietveld Refinement Output of X-ray Diffraction Patterns of Al/Zirconia-Alumina FGM (continued).

Phase	Parameter	d=0.0mm	d=0.1mm	d=0.3mm	d=0.4mm	d=0.8mm	d=1.2mm	d=1.5mm
2. Al ₂ O ₃	Peak function	U	.042(4)	.045(3)	.039(2)	.039(2)	.045(2)	.046(2)
		V	-.01988	-.01988	-.01988	-.01988	-.01988	-.01988
		W	.025(3)	.020(2)	.019(1)	.023(1)	.019(1)	.020(1)
	Peak factor	G ₀	.40(5)	.44(4)	.39(2)	.36(2)	.36(2)	.35(2)
	Asymmetry		-.03(1)	-.049(9)	.052(6)	-.008(9)	.035(7)	.027(7)
	Cell parameters	a	4.7638(7)	4.7587(4)	4.7588(3)	4.7529(4)	4.7532(4)	4.7579(3)
		b	4.7638(7)	4.7587(4)	4.7588(3)	4.7529(4)	4.7532(4)	4.7579(3)
		c	13.0037(22)	12.9897(14)	12.9903(8)	12.9750(11)	12.9752(11)	12.9900(10)
	PO		1.007(12)	1.010(9)	.953(6)	.967(6)	.943(6)	.930(5)
	Scale factor*		275(4)	379(5)	674(5)	671(5)	730(5)	760(5)
3. ZrO ₂ (m)	Peak function	U	1.6(4)	1.1(3)	1.3(2)	1.1(2)	1.3(2)	2.2(3)
		V	-.4(1)	-.29(9)	-.30(6)	-.21(5)	-.28(6)	-.44(8)
		W	.05	.05	.05	.05	.05	.05
	Peak factor	G ₀	.62(16)	.6(1)	.66(7)	.65(6)	.67(7)	.63(7)
	Asymmetry		-.12(2)	-.10(2)	.05(1)	-.02(1)	-.04(1)	.02(2)
	Cell parameters	a	5.1326(42)	5.1181(30)	5.1121(18)	5.1049(20)	5.1060(21)	5.1079(25)
		b	5.1348(42)	5.1376(29)	5.1368(21)	5.1316(21)	5.1348(24)	5.1358(26)
		c	5.3303(42)	5.3232(30)	5.3148(19)	5.3096(19)	5.3135(22)	5.3090(27)
	PO		.915(35)	.93(3)	.98(2)	1.01(2)	.98(2)	.92(2)
	Scale factor*		75(3)	89(3)	135(3)	136(3)	133(3)	137(3)

Table A2.1 Rietveld Refinement Output of X-ray Diffraction Patterns of AT/Zirconia-Alumina FGM (continued).

Phase	Parameter	d=0.0mm	d=0.1mm	d=0.3mm	d=0.4mm	d=0.8mm	d=1.2mm	d=1.5mm
4. ZrO ₂ (t)	Peak function	U	.20(18)	.29(12)	.32	.18(7)	.29(4)	.22(3)
		V	-.19	-.19	-.19	-.19	-.19	-.19
		W	.07(3)	.08(3)	.06	.09(3)	.06(1)	.06(1)
	Peak factor	G ₀	2.1(2)	1.1(3)	1.3(1)	1.2(3)	.9(1)	.7(1)
	Asymmetry		-.02(10)	-.08(4)	-.03(38)	.03(3)	.04(2)	.04(1)
	Cell parameters	a	3.5452(333)	3.5833(209)	3.5978(83)	3.5930(70)	3.5887(23)	3.5823(22)
		b	3.5651(114)	3.5836(73)	3.5745(33)	3.5790(33)	3.5779(12)	3.5768(10)
		c	5.1675(216)	5.2033(95)	5.2024(40)	5.1872(41)	5.2103(17)	5.2129(14)
	PO		1.19(20)	1.16(9)	1.11(8)	1.1(7)	1.06(3)	1.10(3)
	Scale factor*		60(10)	45(8)	82(5)	89(6)	195(6)	174(6)

* x 10⁻⁶

PO is preferred-orientation

Refined scale factors and cell-parameters were used for phase analysis.

Figures in parentheses indicate the estimated standard deviation at the least-significant figures to the left.

Figures without standard deviations were not refined.

Table A2.2 Rietveld Refinement Output of X-ray Diffraction Patterns of Zirconia-Alumina Control Sample and α -alumina standard.

Phase	Parameter		Control	Standard
1. Al ₂ O ₃	Peak function	U	.037(2)	.030(2)
		V	-.0190	-.01988
		W	.021(1)	.024(1)
	Peak factor	G ₀	.30(2)	.50(2)
	Asymmetry		-.04(1)	-.05(1)
	Cell parameters	a	4.7610(3)	4.7595(2)
		b	4.7610(3)	4.7595(2)
		c	13.0028(8)	12.9933(7)
	PO		0.984(6)	0.974(5)
	Scale factor*		752(5)	1150(10)
3. ZrO ₂ (m)	Peak function	U	2.1(3)	
		V	-.48	
		W	.08(2)	
	Peak factor	G ₀	.66(11)	
	Asymmetry		-.03(3)	
	Cell parameters	a	5.1140(48)	
		b	5.1764(44)	
		c	5.3296(42)	
	PO		.900(34)	
	Scale factor*		76(3)	
4. ZrO ₂ (t)	Peak function	U	0.31(2)	
		V	-.189	
		W	.053(3)	
	Peak factor	G ₀	.47(6)	
	Asymmetry		-.056(9)	
	Cell parameters	a	3.6061(12)	
		b	3.6005(5)	
		c	5.2066(8)	
	PO		.993(16)	
	Scale factor*		387(8)	

* $\times 10^{-6}$

PO is preferred-orientation

Refined scale factors and cell-parameters were used for phase analysis.

Figures in parentheses indicate the estimated standard deviation at the least-significant figures to the left.

Figures without standard deviations were not refined.

There were three measures from the refinement which were used to determine the completion of the refinement. The first is the figures-of-merit parameters, i.e. R-Bragg, R-profile, R-weighted-profile, and “goodness of fit” (GoF) parameters. These parameters for the specimen (at various depths), the control sample, and the external standard are depicted in Table A2.2. The Bragg-R factor (R_B) for each phase in each refinement is acceptable, i.e. generally less than 10%. Alumina has a lower R_B values since it is the major phase. The “goodness of fit” (GoF) values are low, i.e. less than 3%, indicating that the refinements are acceptable (Kisi 1994).

Table A2.3 Figures-of-Merit from Rietveld Refinement of Aluminium titanate/Zirconia-Alumina Composite at Various Depths (in %).

Depth (mm)	R_B				R_{exp}	R_p	R_{wp}	GoF
	AT	Al_2O_3	m-ZrO ₂	t-ZrO ₂				
0.0	10.74	4.40	9.91	6.90	12.25	15.11	20.23	2.73
0.1	11.28	4.43	9.14	5.57	11.86	13.97	19.26	2.64
0.3	5.82	3.68	6.67	4.14	11.03	11.41	15.87	2.07
0.4	5.77	3.67	6.12	5.41	11.22	11.24	15.68	1.95
0.8	6.94	2.89	6.38	5.46	11.02	11.61	16.17	2.15
1.2	6.54	3.65	6.57	7.27	10.99	11.76	16.16	2.16
1.5	7.34	3.56	7.05	8.61	10.83	11.44	15.62	2.08
Control	-	4.92	10.63	10.34	11.19	12.21	17.23	2.37
Standard	-	3.80	-	-	11.60	12.89	20.71	3.80

Subscript *B* for Bragg, *exp* for expected, *p* for profile, *wp* for weighted profile.

GoF is “Goodness of Fit”. *AT* is aluminium titanate, m-ZrO₂ and t-ZrO₂ are monoclinic and tetragonal zirconia, respectively.

The second measure is difference plot from a refinement. The representative output plots from refinement of the patterns of the sample (at depths of 0.1 mm and 1.2 mm) are shown in Figure 4.6. The plots show no unassigned reflections, indicating that the correct phases were used in the refinement. Fluctuations in the difference profile (line below the plot) in each plot are reasonably negligible. Therefore, the plots are acceptable.

The final measure is the estimated standard deviations (esd's) of the refined parameters. These esd's are depicted in the parenthesis of each refined parameter (Table A2.1). As can be seen from the table, the standard deviation is generally

acceptable. Standard deviations of scale factors and unit cell volumes are shown in Tables 4.4 and 4.5. These esd's are generally low, ie. less than 10%. This indicates that the refinements were acceptable from the esd's point of view. Relatively high standard deviations were observed for tetragonal zirconia at low depths because it is a minor phase.

APPENDIX 3: CALIBRATION CURVES TO DETERMINE MASS ATTENUATION COEFFICIENTS BY COMPTON SCATTERING

Two calibration curves were constructed to determine the mass attenuation coefficient (MAC) of the FGM samples at the $\text{CuK}\alpha$ wavelength. the calibration curve in Figure A3.1 was used to calculate the MAC of the specimens for $\text{MoK}\alpha$ radiation. When a Compton peak intensity of a specimen was measured, its MAC value for $\text{MoK}\alpha$ could readily be calculated by taking the reciprocal value of the corresponding intercept in the $1/\mu$ axis.

Calibration curve A3.2 was used to convert the MAC values at the $\text{MoK}\alpha$ to those at the $\text{CuK}\alpha$ radiation. The latter is the radiation used for the x-ray diffractometry. After determination of MAC values of the specimens for the $\text{MoK}\alpha$ wavelength using calibration curve A3.1, these values were converted to those for the $\text{CuK}\alpha$ wavelength by finding the corresponding projections for each value in the calibration curve of Figure A3.2.

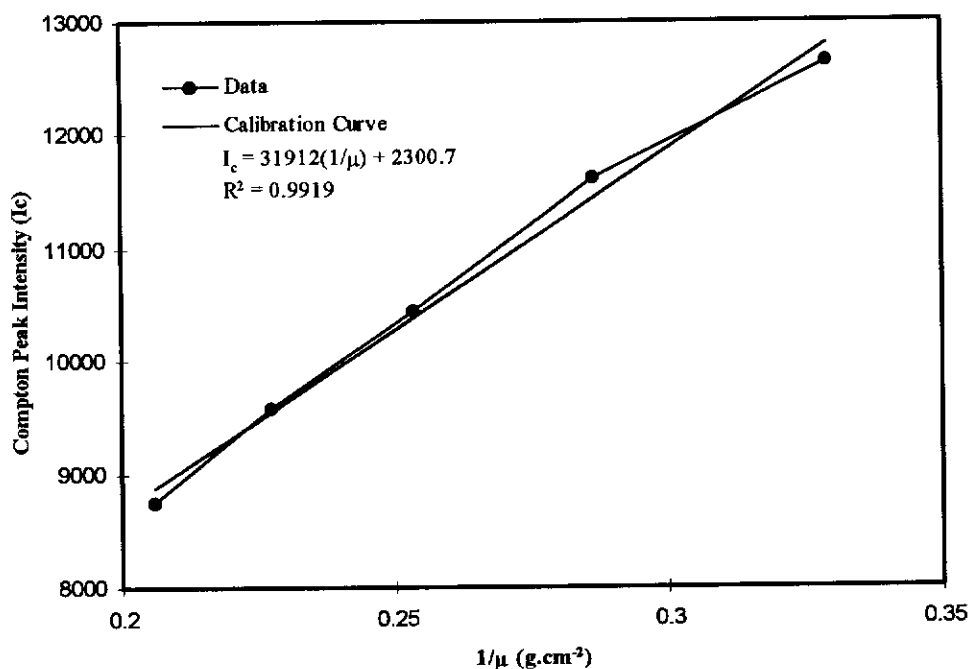


Figure A3.1 Calibration curve for mass attenuation coefficient (MAC) determination constructed using alumina-zirconia compacted powders (zirconia content from 0% to 20% by weight). $\text{MoK}\alpha$ radiation was used.

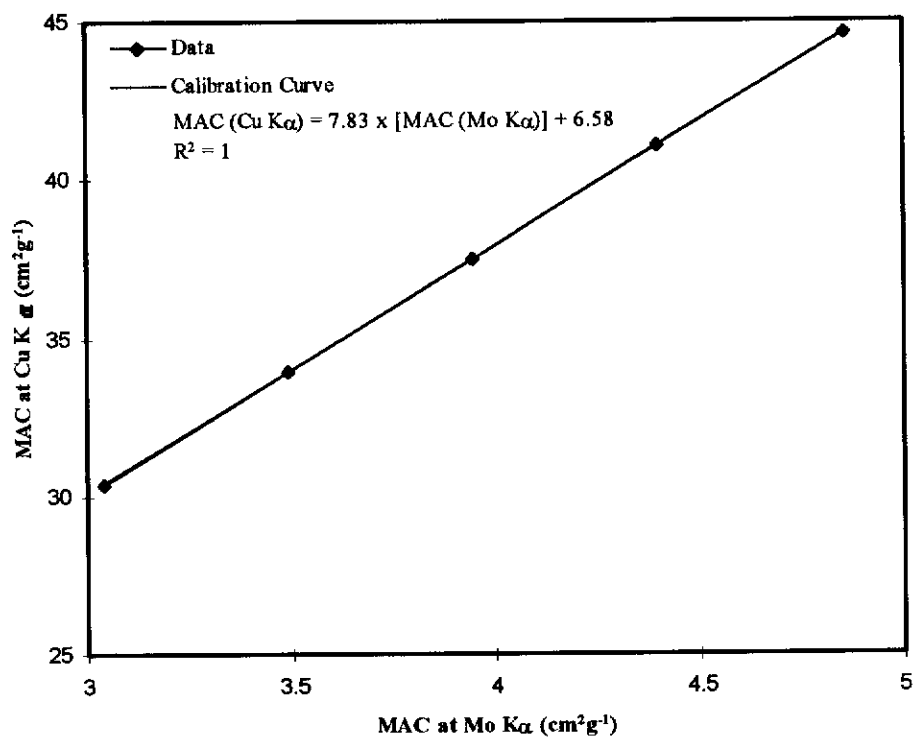


Figure A3.2 Calibration curve to convert the MAC values from those at the MoK α radiation to those at the CuK α radiation.

LIST OF PUBLICATIONS FROM THESIS STUDY

1. Pratapa, S. and Low, I.M. (1995). Processing and Properties of Functionally Gradient Ceramic Materials. *5th Postgraduate Research Conference, Australian Institute of Physics, Western Australian Branch*. Jarrahdale, Western Australia, 30 August - 1 September 1995.
2. Pratapa, S. and Low, I.M. (1996). Synthesis and Properties of Functionally-gradient Aluminium Titanate-Mullite-Alumina Composites. *J. Mater. Sci. Lett.* **15**, pp 800-802.
3. Pratapa, S. and Low, I.M. (In press). Effect of Spodumene Addition on the Properties of Functionally-gradient Aluminium Titanate/Zirconia-toughened Alumina Composites. In: *Proceedings of the 2nd International Meeting of Pacific Rim Ceramic Societies*. Cairns, Australia, 15-17 July 1996.
4. Pratapa, S., O'Connor, B.H. and Low, I.M. (1996). Application of X-ray Diffraction Rietveld Refinement for Phase Analysis in a Functionally-graded Aluminium Titanate/Zirconia-Alumina Composite. In: *Proceedings of the 1996 State Conference and Workshop of the Australian X-ray Analytical Association Inc. (WA) and Western Australian Society for Electron Microscopy*. Pemberton, Western Australia, 27-29 September 1996.
5. Pratapa, S., O'Connor, B.H. and Low, I.M. (In press). Phase Composition Profile Character of a Functionally-graded $\text{Al}_2\text{TiO}_5/\text{ZrO}_2\text{-Al}_2\text{O}_3$ Composite. In: *Proceedings of the 4th International Symposium on Functionally Graded Materials*. Tsukuba, Japan, 21-24 October 1996.